THESIS FOR THE DEGREE OF DOCTOR OF PHILOSOPHY

Analysis and Evaluation of Wingsails with Crescent-Shaped Profiles – from Aerodynamics to Aeroelasticity

HENG ZHU

Department of Mechanics and Maritime Sciences

CHALMERS UNIVERSITY OF TECHNOLOGY

Gothenburg, Sweden, 2024

Analysis and Evaluation of Wingsails with Crescent-Shaped Profiles – from Aerodynamics to Aeroelasticity

Analysis and Evaluation of Wingsails with Crescent-Shaped Profiles – from Aerodynamics to Aeroelasticity

HENG ZHU

Chalmers University of Technology

Department of Mechanics and Maritime Sciences

Division of Marine Technology

Abstract

Seaborne transportation accounts for ~2% of global greenhouse gas (GHG) emissions. The International Maritime Organization (IMO) has stipulated that GHG emissions should be reduced by 50% before 2050 compared to 2018. The use of wind-assisted ship propulsion (WASP) is considered an effective way to reach the target. In this context, this thesis aims to promote wingsails with crescent-shaped profiles through the assessment of their aerodynamic and aeroelastic performance, as well as long-term propulsive efficiency. This thesis provides an in-depth investigation into the unsteady aerodynamic and aeroelastic characteristics of wingsails, setting it apart from other related work.

Conceptual designs of crescent-shaped wings were investigated using high-fidelity numerical simulations. Wind tunnel (WT) tests were conducted for validation. Flows were simulated with the unsteady Reynolds-averaged Navier-Stokes equations (URANS) and improved delayed detached eddy simulation (IDDES). Structures were analyzed with finite element methods. To simulate the fluid-structure interaction, a two-way coupled algorithm was used. Additionally, the long-term propulsion performance was assessed with an in-house program, ShipCLEAN.

The aerodynamic analyses revealed that the crescent-shaped wingsails generate higher thrust forces compared to traditional symmetric airfoils, especially under sidewind conditions. However, unsteady aerodynamic characteristics due to strong flow separation were observed. Different structural configurations were evaluated, with a focus on balancing the weight, strength, and rigidity. The aeroelastic analyses pointed out significant fluid-structure interaction effects. The structural deformations have a notable influence on thrust generation. It means that aeroelasticity must be considered in the wingsail design and operation in practice. A long-term case study demonstrated that a large commercial ship equipped with a selected crescent-shaped wingsail achieves fuel savings of up to 10%, depending on wind conditions and operational strategies.

Keywords: aeroelasticity, cambered profile, fluid-structure interaction, wind-assisted ship propulsion, wingsail

Preface

I express profound gratitude to the myriad individuals, institutions, and organizations whose support and contributions were indispensable over the past three and a half years, culminating in the completion of my thesis.

Foremost, I extend my deepest appreciation to my advisors, Hua-Dong Yao, Jonas W. Ringsberg, Bengt Ramne, and Carl-Erik Janson. Their expert guidance and steadfast support were critical throughout my doctoral journey. Their extensive knowledge and continuous encouragement laid the foundation for my achievements. This dissertation could not have been realized without their invaluable input.

Special thanks are due to Hua-Dong Yao for his specialized expertise in fluid dynamics and computational mechanics, as well as his kind supervision and mentorship, which were crucial in addressing the complex aspects of my research. His patient guidance and consistent support greatly contributed to both my personal and academic development.

I also wish to express my gratitude to Jonas W. Ringsberg for his comprehensive guidance and support in advancing my doctoral studies. His comprehensive knowledge of naval architecture and structural engineering, as well as his leadership as my line manager, were invaluable. I am particularly grateful for his insightful feedback and critical analyses, which were essential in refining my structural analysis.

My appreciation extends to Bengt Ramne for his broad perspective and astute feedback, which have significantly shaped my research and enhanced its relevance to practical applications.

I sincerely thank Valery Chernoray for his invaluable support with the wind tunnel tests. His expertise in experimental fluid dynamics was crucial to the success of this research.

Moreover, I am deeply indebted to Carl-Erik Janson for his exceptional expertise in fluid dynamics. His insights and wise counsel were pivotal in shaping my research and deepening my understanding of the fundamental principles of fluid mechanics.

Special recognition goes to my co-authors, Melisa Nikmanesh, Sreeharsha Bikkireddy, Fabian Thies, and Yanlin Shao for their cooperation during my PhD study, which was crucial to my research.

I extend my sincere thanks to my study advisors and administrators, Scott MacKinnon, Ida-Maja Hassellöv, and Carina Schmidt, for their invaluable feedback during my follow-up meetings.

A special thanks to all my colleagues at the Division of Marine Technology for creating such a supportive and collaborative working environment.

I am forever grateful for the unwavering love and support of my parents and grandparents, whose continual inspiration and encouragement have been fundamental to my academic success.

I want to extend my heartfelt love to my girlfriend, Jingnan Zhang, who earned her PhD degree last year. Her dedication, intelligence, and resilience continue to inspire me every day, and we are proud of our remarkable achievements. I am deeply grateful for her unwavering support and honored for her being part of my academic journey.

To all who have contributed to this journey, your involvement has been invaluable. Thank you for being part of my academic and personal growth.

<div align="right">

Heng Zhu
Gothenburg, September 2024

</div>

Table of Contents

List of appended Papers

This thesis consists of an extended summary and the following appended **Paper**s.

For **Paper**s **I**, **II**, **IV**, and **V**, the author contributed to the ideas, work plan, modeling, simulation, pre- and post-processing, and writing.

For **Paper III**, the author contributed to the ideas, work plan, part of the experiments, modeling, simulation, pre- and post-processing, and writing.

Paper I   **Zhu, H.***, Yao, H.-D., Thies, F., Ringsberg, J. W., & Ramne, B. (2023a). Propulsive performance of a rigid wingsail with crescent-shaped profiles. *Ocean Engineering*, *285*, 115349. https://doi.org/10.1016/j.oceaneng.2023.115349.

Paper II   **Zhu, H.***, Yao, H.-D., & Ringsberg, J. W. (2024a). Unsteady RANS and IDDES studies on a telescopic crescent-shaped wingsail. *Ships and Offshore Structures*, 1-14. https://doi.org/10.1080/17445302.2023.2256601.

Paper III   **Zhu, H.***, Chernoray, V., Ringsberg, J. W., Ramne, B., & Yao, H.-D. (2025a). Experimental and numerical studies on moderate-Re aerodynamics of cambered thick wingsails in crescent shape. *Under review by Journal of Ocean Engineering and Science. Preprint is available at SSRN: https://ssrn.com/abstract=4929670.*

Paper IV   **Zhu, H.***, Chernoray, V., Ringsberg, J. W., Ramne, B., Shao, Y., & Yao, H.-D. (2025b). Reynolds number sensitivity of cambered wingsail aerodynamics. *Under revision in Ocean Engineering.*

Paper V   **Zhu, H.***, Ringsberg, J. W., Ramne, B., & Yao, H.-D. (2025c). Fluid-structure interaction analysis of a crescent-shaped wingsail. *In manuscript.*

* Corresponding author.

List of other Papers by the author

In addition to the appended **Paper**s, the author produced the following publications and manuscripts.

Paper A   **Zhu, H.***, Nikmanesh, M. B., Yao, H. -D., Ramne, B., & Ringsberg, J. W. (2022a). Propulsive performance of a novel crescent-shaped wind sail analyzed with unsteady RANS. *Proceedings of the ASME 2022 41st International Conference on Ocean, Offshore and Arctic Engineering (OMAE 2022), June 5– 10, Hamburg, Germany* (Vol. 7, p. V007T08A053). https://dx.doi.org/10.1115/OMAE2022-79867.

Paper B   **Zhu, H.***, Yao, H.-D., & Ringsberg, J. W. (2022b). Unsteady RANS and IDDES study on a telescopic crescent-shaped windsail. *Proceedings of the 7th International Conference on Ships and Offshore Structures (ICSOS 2022), October 17–19, Ålesund, Norway.*

Paper C   **Zhu, H.***, Bikkireddy, S., Ringsberg, J. W., Yao, H.-D., & Ramne, B. (2023b). Structure analysis of lightweight sail structures for wind-assisted ship propulsion. In J. W. Ringsberg & C. Guedes Soares (Eds.), *Advances in the Analysis and Design of Marine Structures: Proceedings of 9th International Conference on Marine Structures (MARSTRUCT 2023), 3–5 April 2023, Gothenburg, Sweden* (pp. 327–335). CRC Press. https://dx.doi.org/10.1201/9781003399759-36.

Paper D.   **Zhu, H.**, Chernoray, V., Ringsberg, J. W., Yao, H.-D.*, & Ramne, B. (2023c). Experimental study on structure responses of triple wing sails to turbulence flows at multiple apparent wind angles. In J. W. Ringsberg & C. Guedes Soares (Eds.), *Advances in the Analysis and Design of Marine Structures: Proceedings of 9th International Conference on Marine Structures (MARSTRUCT 2023), 3– 5 April 2023, Gothenburg, Sweden* (pp. 781–787). CRC Press. https://dx.doi.org/10.1201/9781003399759-86.

Paper E   **Zhu, H.**, Thies, F.*, Ringsberg, J. W., & Ramne, B. (2023d). Development and performance analysis of a crescent-type sail for WASP applications. *Proceedings of the International Academic Conference on Shipping, Sustainability & Solutions 2023 (SSS 2023), March 2–3, Hamburg, Germany.*

Paper F   **Zhu, H.** (2023e). *Methods for the Evaluation of Wingsails with a Crescent-Shaped Profile.* Chalmers University of Technology. Gothenburg, Sweden.

Paper G   **Zhu, H.***, Chernoray, V., Ringsberg, J. W., Yao, H.-D., & Ramne, B. (2024b). Fluid-structure interaction analysis of crescent-shaped wingsails. *Proceedings of the ASME 2024 43rd International Conference on Ocean, Offshore and Arctic Engineering (OMAE 2024), June 9 – 14, Singapore, Singapore* (Vol. 6, p. V006T08A004). https://doi.org/10.1115/OMAE2024-125739.

Paper H   **Zhu, H.***, Yao, H.-D., & Ringsberg, J. W. (2025d). An unsteady RANS CFD study of the turbulent flow around an aeroelastic foil. *In manuscript.*

* Corresponding author.

Nomenclature

A_F Frontal area of the wingsail [m²], *i.e.* A_S projected in the X direction.

A_H Cross-section area of the wingsail [m²].

A_S Wingsail reference area [m²]. $A_S = L_c \cdot H$.

A_{WT} Streamwise sectional area of the WT test section [m²].

C_D Drag coefficient [-]. C_D is defined as $\frac{F_D}{\frac{1}{2}\rho_{air}A_S V_{AW}^2}$ for full scale and $\frac{F_D}{\frac{1}{2}\rho_{air}A_S V_\infty^2}$ for model scale. $\langle C_D \rangle$ represents the time-averaged drag coefficient. C_{D_Mea} represents the drag coefficient measured in the WT tests before blockage correction.

C_L Lift coefficient [-]. C_L is defined as $\frac{F_L}{\frac{1}{2}\rho_{air}A_S V_{AW}^2}$ for full scale and $\frac{F_L}{\frac{1}{2}\rho_{air}A_S V_\infty^2}$ for model scale. $\langle C_L \rangle$ represents the time-averaged lift coefficient. C_{L_Mea} represents the lift coefficient measured in the WT tests before blockage correction.

C_M Moment coefficient [-]. C_M is defined as $\frac{M}{\frac{1}{2}\rho_{air}A_S L_c V_{AW}^2}$ for full scale and $\frac{M}{\frac{1}{2}\rho_{air}A_S L_c V_\infty^2}$ for model scale. $\langle C_M \rangle$ represents the time-averaged moment coefficient.

C_p Pressure coefficient [-]. C_p is defined as $\frac{p}{\frac{1}{2}\rho_{air}V_{AW}^2}$ for full scale and $\frac{p}{\frac{1}{2}\rho_{air}V_\infty^2}$ for model scale. $\langle C_p \rangle$ represents the time-averaged drag coefficient.

C_T Thrust coefficient [-]. C_T is defined as $\frac{F_T}{\frac{1}{2}\rho_{air}A_S V_{AW}^2}$.

C_τ Wall friction coefficient [-]. C_τ is defined as $\frac{\tau}{\frac{1}{2}\rho_{air}V_{AW}^2}$ for full scale and $\frac{\tau}{\frac{1}{2}\rho_{air}V_\infty^2}$ for model scale. $C_{\tau\{\}}, \{\} = X, Y, Z$, represents the component of the wall friction coefficient in a certain direction, *e.g.*, $C_{\tau X}$ is the wall friction coefficient in the X direction.

E Young's modulus [GPa].

F_D Drag [N].

F_L Lift [N].

F_S Side force [N].

F_T Thrust [N].

f Frequency [Hz].

f_e Eigenfrequency [Hz]. $f_{e\{\}}, \{\} = 1,2,3,4 ...$, represents the eigenfrequency in different modes, *e.g.*, f_{e1} is the fundamental eigenfrequency.

H Wingsail height [m], *i.e.*, the spanwise length of the wingsail.

k_t Turbulent kinetic energy [m²/s²], or TKE for short.

L_c Chord length [m].

Ma Mach number [-]. The Mach number of a wingsail is defined by $Ma = \frac{V_{AW}}{c}$ for full scale and $Ma = \frac{V_\infty}{c}$ for model scale, where c is the speed of sound.

p Relative pressure [Pa]. Relative pressure is the difference between absolute pressure and the atmospheric pressure.

Q Q-criterion [s^{-2}].

Re Reynolds number [-]. The Reynolds number of a wingsail is defined by $Re = \frac{\rho_{air}V_{AW}L_c}{\mu}$ for full scale and $Re = \frac{\rho_{air}V_\infty L_c}{\mu}$ for model scale.

St Strouhal number [-]. The Strouhal number of a wingsail is defined by $St = \frac{fL_c}{V_{AW}}$ for full scale and $St = \frac{fL_c}{V_\infty}$ for model scale.

V Flow velocity [m/s]. $V_{\{\}}$, $\{\} = X,Y,Z$, represents the component of the flow velocity in a certain direction, $e.g.$, V_X is the streamwise velocity and V_Z is the spanwise velocity.

V_{AW} Apparent wind speed [m/s]. The definition of the apparent wind speed is illustrated in Figure 17.

V_S Ship speed [kn].

V_{TW} True wind speed [kn].

V_∞ Inlet velocity in the WT [m/s], corresponded to V_{AW} in practice.

y^+ Non-dimensional wall normal distance [-].

α Angle of attack [°], or AOA for short.

α_c Critical angle of attack [°].

β Yaw angle in the WT [°], corresponded to θ_{AW} in practice. The definition of the yaw angle is illustrated in Figure 9(c).

Δ_{DES} DES length scale [m].

δ_{99} Boundary layer thickness [m].

θ_{AW} Apparent wind angle [°], or AWA for short. The definition of the apparent wind angle is illustrated in Figure 17.

θ_{TW} True wind angle [°], or TWA for short.

λ Tip displacement [m]. $\lambda_{\{\}}$, $\{\} = X,Y,Z$, represents the component of the tip displacement in a certain direction, $e.g.$, λ_X is the streamwise tip displacement and λ_Y is the cross-flow tip displacement.

μ Dynamic viscosity [Pa · s].

ν Poisson's ratio [-].

ρ Material density [kg/m^3]. ρ_{Al} represents the density of aluminum, and ρ_{steel} represents the density of steel.

ρ_{air} Air density [kg/m^3].

σ Stress [MPa]. $\sigma_{\{\}\{\}}, \{\} = i, j, k$, represents stress in a certain direction. σ_{ii}, σ_{jj}, and σ_{kk} are the normal stresses. σ_{ij}, σ_{jk}, and σ_{ki} are the shear stresses.

σ_{buck} Buckling stress [MPa].

σ_{Mises} von Mises stress [MPa].

σ_{yield} Yield stress [MPa].

τ Wall friction [MPa]. $\tau_{\{\}}, \{\} = X, Y, Z$, represents the component of the wall friction in a certain direction, *e.g.*, τ_X is the streamwise wall friction.

ω Vorticity [s^{-1}]. $\omega_{\{\}}, \{\} = X, Y, Z$, represents the component of the vorticity in a certain direction, *e.g.*, ω_X is the streamwise vorticity and ω_Z is the spanwise vorticity. ω^* represents the non-dimensional vorticity defined by $\omega^* = \frac{\omega \cdot L_C}{V_\infty}$, *e.g.*, ω_X^* is the non-dimensional streamwise vorticity and ω_Z^* is the non-dimensional spanwise vorticity.

Abbreviations

ALE	Arbitrary Lagrangian–Eulerian.
AOA	Angle of attack.
AWA	Apparent wind angle.
BC	Boundary condition.
BL	Boundary layer.
CFD	Computational fluid dynamics.
CMEMS	Copernicus Marine Environment Monitoring Service.
DDES	Delayed detached eddy simulation.
DES	Detached eddy simulation.
DNS	Direct numerical simulation.
DOF	Degree of freedom.
FEA	Finite element analysis.
FFT	Fast Fourier transform.
FSI	Fluid-structural interaction.
FVM	Finite volume method.
GHG	Greenhouse gas.
IDDES	Improved delayed detached-eddy simulation.
IMO	International Maritime Organization.
LES	Large eddy simulation.
LESB	Leading-edge separation bubble.

LSQ	Least squares.
NACA	(The United States) National Advisory Committee for Aeronautics.
NSGA-II	Non-dominated sorting genetic algorithm.
PCTC	Pure car and truck carrier.
PINN	Physics-informed neural networks.
PIV	Particle image velocimetry.
PPP	Power prediction program.
PSO	Particle swarm optimization.
RANS	Reynolds-averaged Navier–Stokes.
RBF	Radial basis function.
RBD	Rigid body dynamics.
SIMPLE	Semi-implicit method for pressure-linked equations.
SST	Shear stress transport.
TKE	Turbulent kinetic energy.
TWA	True wind angle.
URANS	Unsteady Reynolds-averaged Navier–Stokes.
VLCC	Very large crude carriers.
VLM	Vortex lattice method.
VIV	Vortex-induced vibration.
VPP	Velocity prediction program.
WASP	Wind-assisted ship propulsion.
WT	Wind tunnel.

1 Introduction

This Chapter begins with an introduction to the thesis, providing a brief overview of the background, and a discussion of current knowledge gaps, objectives, and limitations. The outline of the thesis is also presented at the end of this Chapter.

1.1 Background

Climate change, particularly global warming driven by greenhouse gas (GHG) emissions, is widely acknowledged as one of the most significant threats facing human society. Today, shipping accounts for over 80% of all freight transport by volume (UNCTAD, 2024), which shares ~2% of the global GHG emissions (Faber *et al.*, 2020; Ritchie *et al.*, 2020), as shown in Figure 1. The energy demands of shipping are immense, with an estimated annual fuel consumption of ~330 million tonnes (IMO, 2020; Kass *et al.*, 2018). For example, a pure care and truck carrier (PCTC), may consume 30–60 tons of fossil fuel per day, depending on the various operational practices, strategies, and conditions under which the vessel is managed and run (Bialystocki & Konovessis, 2016).
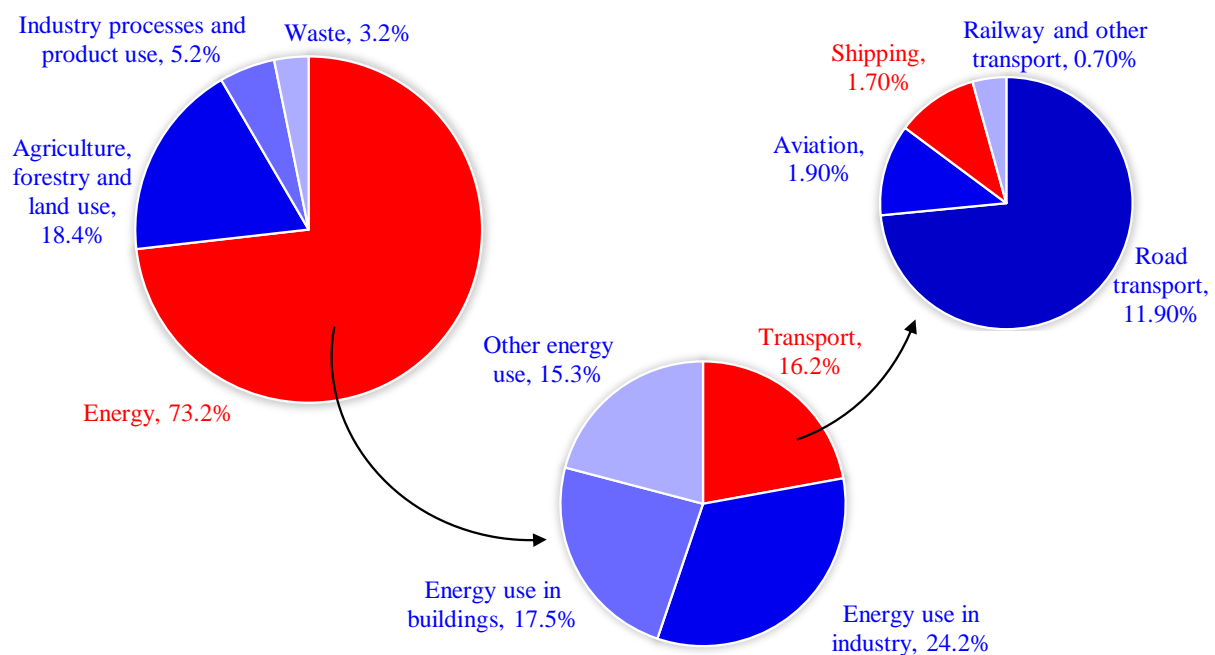
Figure 1. Global GHG emissions from different sectors based on the data in 2017 (Ritchie *et al.*, 2020).

According to the International Maritime Organization (IMO), by 2050, the shipping industry should reduce its GHG emissions to 50% of the level in 2008 (IMO, 2018). Wind-assisted ship propulsion (WASP) for large commercial ships is seen as one promising solution, both for new ship designs and retrofitting, to achieve this goal. According to data from Lloyd's Register (Register, 2024), bulk carriers have been the largest adopters of WASP to date, with 10 vessels already installed and 18 more on order. This segment of the fleet is also expected to account for a significant portion of retrofitting projects, which will complement new builds as the adoption of wind propulsion technologies accelerates. Different sail technologies have been proposed, such as Flettner rotors, wingsails, DynaRigs, and kite sails. Flettner rotors utilize the Magnus effect to generate lift, making them highly effective under sidewind conditions. Kite sails

primarily rely on drag forces for propulsion, which optimizes their performance under downwind conditions. In contrast, wingsails offer efficient operation across a broader range of wind directions compared to other WASP concepts (Zhu, 2023).

Since winds can come from either the starboard or the port side of a ship, wingsails should withstand winds equally from both sides. Consequently, early wingsail designs featured symmetric profiles without camber, such as the NACA 00xx series (Atkins, 1996). These profiles were originally designed to achieve a high lift-to-drag ratio since drag is always negative for airplane wings or wind turbine blades. However, for wingsails, drag can also contribute to thrust under some conditions, *e.g.*, downwind (Kimball, 2009). Modern designs target high lift and drag coefficients instead. In this context, to achieve higher lift, which is the major contributor to the trust under sidewind conditions, modern wingsail profiles have incorporated cambers, *e.g.*, segment (Atkinson *et al.*, 2018; Atkinson, 2019; Atkinson & Binns, 2018), arc (Chen *et al.*, 2022; Zeng *et al.*, 2024a; Zeng *et al.*, 2023), and crescent (Nikmanesh, 2021; Ouchi *et al.*, 2011; Ouchi *et al.*, 2013; Zhang *et al.*, 2023; Zhu *et al.*, 2022b), as shown in Figure 2. Among these cambered profiles, crescent-shaped profiles often have a smoother and more gradual curvature, which helps reduce abrupt flow separations compared to other profiles.
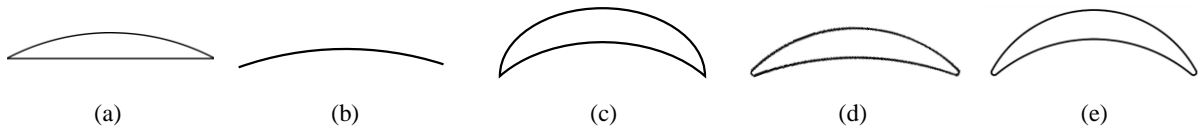
Figure 2. Schematics of cambered wingsail profiles: (a) segment (Atkinson *et al.*, 2018); (b) arc (Chen *et al.*, 2022); (c) crescent (Ouchi *et al.*, 2011); (d) crescent (Nikmanesh, 2021); (e) crescent (Zhu *et al.*, 2022b).

It should be mentioned that two- and three-element profiles are currently also popular concepts (Blakeley *et al.*, 2012). These concepts are combinations of a main foil with one or two small foils. The small foils are utilized to increase the generation of lift and drag (Smith, 1975). Conventional airfoil profiles, such as NACA 0015, are typically used in these concepts. From a practical perspective, conventional airfoil profiles always have the same leading edge, so the wingsail needs to make a half turn when the apparent wind direction is changing between the starboard and the port side under downwind conditions ($\theta_{AW} \sim 180°$), as shown in Figure 3(a). However, a crescent-shaped wingsail is easier to operate under downwind conditions, since it can swap the leading and trailing edges when changing tack (Zhu *et al.*, 2022a), as shown in Figure 3(b).

In 2022, the first ship with a crescent-shaped wingsail developed by the Wind Challenger project (Ouchi *et al.*, 2023), *Shofu Maru*, started its voyage. The cargo ship was reported to save an average of 30% on fuel on the Yokohama-Seattle route (Zhang *et al.*, 2024). There are also two very large crude carriers (VLCCs) operated by China Merchants Energy Shipping CO., LTD, *New Vitality* (in service since 2018) and *New Aden* (in service since 2022), which are both equipped with crescent-shaped wingsails. The fuel consumption reductions of these two VLCCs are up to 5% and 9%, respectively (Ma *et al.*, 2022; Wang *et al.*, 2022).
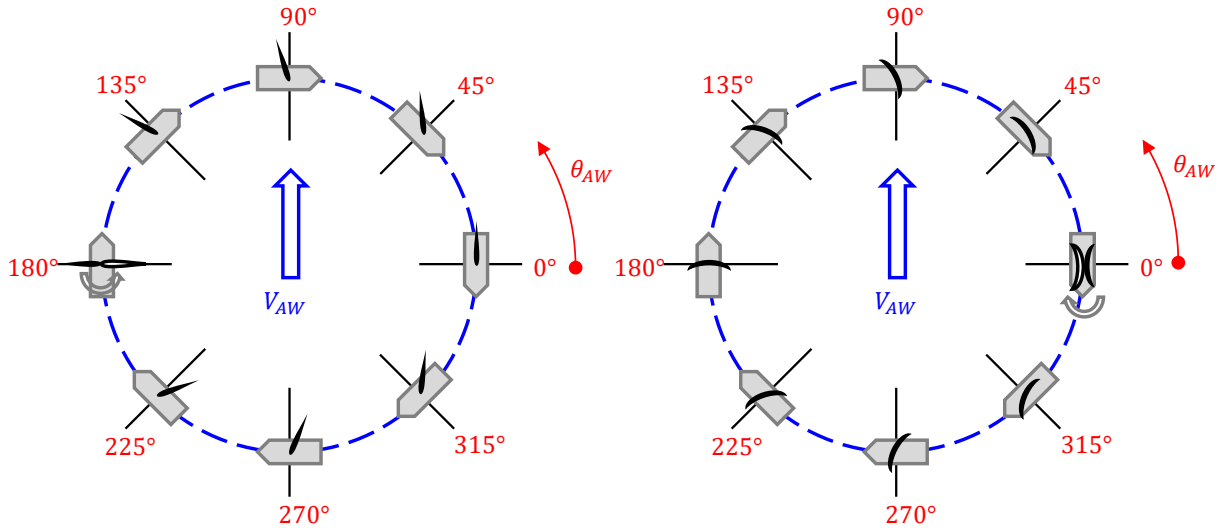
(a) Symmetric profile (NACA 0015).   (b) Crescent-shaped profile.

Figure 3. Changed tacks of a symmetric profile (left) and a crescent-shaped profile (right). Here θ_{AW} represents the apparent wind angle, and the blue hollow arrows indicate the apparent wind direction.

1.2 Objectives

From a performance evaluation perspective, several knowledge gaps persist in WASP. A key issue is the lack of standardized methodologies to accurately assess the performance of WASP technologies under varying operational and environmental conditions. Besides, the fundamental physical mechanisms of WASP facilities, such as aerodynamics, have not been deeply investigated yet, which limits further development of WASP. Closing these gaps is essential to establishing reliable performance benchmarks and ensuring consistent, real-world efficiency gains.

Specifically for cambered wingsails, although they have shown great potential, there have been several unresolved issues that still require further investigation.

- **Aerodynamic characteristics.** The current understanding of the aerodynamic characteristics of cambered wingsail profiles remains incomplete, particularly regarding their complex flow dynamics. The profiles, characterized by large cambers, exhibit significantly different aerodynamic characteristics compared to traditional symmetric airfoils (Atkinson, 2019; Nikmanesh, 2021; Zhu *et al.*, 2022b). The flow around these wingsails experiences strong separation, making accurate predictions of lift and drag coefficients challenging (Chen *et al.*, 2022; Zeng *et al.*, 2023). Understanding these aerodynamic characteristics is crucial as they directly influence design and aerodynamic optimization, thereby impacting the efficiency of wingsails in real-world operations.

- **Feasibility of simulation and experiment methods.** When this thesis work was initiated in 2020, few numerical studies has been conducted on crescent-shaped wingsails. Furthermore, it was unclear whether model-scale simulations and wind tunnel (WT) tests remained valid for the evaluation of full-scale characteristics. These limitations could lead to inaccurate aerodynamic predictions and potentially mislead the wingsail design process. Therefore, it is essential to discuss the capabilities of the various existing computational fluid dynamics (CFD) methods.

- **Structural responses to wind loads.** Wingsails are usually designed as light-weight thin-

3

wall structures, which can be significantly deformed due to wind loads. The structural deformation of wingsails can alter flow patterns, thereby impacting the generation of aerodynamic forces (Souppez, 2023). This effect is known as fluid-structure interaction (FSI). It was unknown whether neglecting the FSI in the wingsail design process could lead to an overestimation of aerodynamic loads. Despite its critical importance, the FSI had not been explored when this thesis work was begun.

- **Long-term performance.** The shipping industry is focused on fuel savings (Khan *et al.*, 2021; Lu & Ringsberg, 2020; Thies & Fakiolas, 2022). However, accurately predicting long-term improvements poses significant challenges due to the need to account for diverse meteorological and oceanographic conditions, *i.e.*, metocean.

The overall aim of this thesis is to address the aerodynamic and aeroelastic performance of crescent-shaped wingsails, with particular focus on their unsteady characteristics. To achieve this aim and fill the knowledge gaps, four objectives are set below.

- Reveal the aerodynamic characteristics of wingsails with cambered profiles, with an emphasis on the quantification of the unsteady characteristics due to significant flow separation.

- Evaluate different CFD and WT test approaches for wingsail aerodynamics to propose suggestions for best practices. This evaluation will focus on the accuracy and relevance of different methods, particularly in relation to model-scale effects.

- Explore the FSI characteristics of cambered wingsails and address the impact of FSI on their aerodynamic performance, *i.e.*, to how much extent, the FSI affects the propulsive performance.

- Demonstrate long-term energy efficiency by integrating ship motion dynamics and metocean databases. Estimate the potential fuel savings for commercial vessels within an extended operational period.

1.3   Scope and delimitations

This work concentrates on a technological niche (Nykvist & Whitmarsh, 2008). The scope is confined to crescent-shaped wingsails that have cambered profiles. Other WASP concepts such as Flettner rotors, kite sails, soft sails, and two- and three-element wingsails are not investigated. The assumptions below are adopted.

- The external geometry of the wingsail design is generated by ScandiNAOS AB and further improved by (Nikmanesh, 2021). This thesis focuses on assessing the aerodynamic and aeroelastic performance of the wingsails, so re-evaluating the fundamental geometric design process is not included. The aerodynamic shape of the wingsail is simplified when performing CFD and FSI simulations. In the three-dimensional CFD simulations, the wingsail is modeled as a uniformly extruded geometry.

- The wind gradient is only considered in the long-term propulsive performance case study, and the interactions among wingsails, ship hull, and superstructures are not considered. The wingsail on a cargo vessel operates in a highly dynamic and turbulent environment. The large freeboard height causes significant air-sea interaction disturbances, compounded by the vessel's forward speed. This results in a complex vertical profile of airflow influenced by large-scale turbulence. Additionally, the movement of the vessel and varying

meteorological conditions further disrupt the flow, which significantly impacts aerodynamic performance. Although this thesis acknowledges the complexity, the apparent wind, *i.e.*, the inlet velocity, is still assumed to be a uniformly distributed horizontal flow. This assumption allows for a clearer understanding of wingsail performance under controlled conditions. Since the Re of the wingsail profiles is normally in the range of 3×10^6 to 3×10^7, in which the force coefficients are not sensitive to the Re, this assumption is considered reasonable.

- The wingsails are assumed to be installed on a fixed deck without any motion. The heeling angles, rolling motions, and leeway caused by the wingsails are neglected. One exception is the long-term fuel saving case study where the ship motion dynamics are integrated.

- In two-way coupled FSI simulations, the internal substructures of the wingsail are simplified. The simplification method is explained in Section 3.4.2. The material properties of the structure are assumed to be linear elastic, so plastic deformation is not considered. With this assumption, the FSI is regarded as an aeroelastic problem.

1.4 Thesis outline

This thesis is divided into six Chapters. In Chapter 1, a brief introduction is provided. In Chapter 2, relevant literature is reviewed. Detailed information about the methods applied and developed is given in Chapter 3. An overview of the five appended **Paper**s is presented in Chapter 4, and selected results from the appended **Paper**s are summarized in Chapter 4. In Chapter 5, conclusions are listed. Future research is suggested in Chapter 6.

2 Literature review

The purpose of this literature review in this Chapter is to provide a comprehensive overview of the current state of knowledge in the field of wingsails, especially those with crescent-shaped profiles. The review aims to identify existing technologies and methodologies related to crescent-shaped wingsails. Meanwhile, this Chapter also points out specific knowledge gaps that remain unaddressed, which are critical for further advancements. These knowledge gaps will guide the research focus of this thesis, ensuring that it targets the most pressing challenges in the field.

It also needs to be noted that the research work for this thesis started in 2021, with the first publication released in 2022. Related studies including those from the author are reviewed for a comprehensive understanding of both historical and contemporary perspectives on wingsail research is presented.

2.1 Aerodynamic investigations

Accurately predicting the wind loads on a sail is essential for assessing its propulsive performance, as this is inherently an aerodynamic challenge. This can be solved with theoretical, numerical, experimental, and empirical methods.

2.1.1 Theoretical and empirical calculations

Theories such as the thin-airfoil theory can be used to deduce wind loads. Recently, these methods were applied to predict wingsail aerodynamics. von Klemperer *et al.* (2023) used XFOIL (Drela, 1989) to analyze the aerodynamic loads on a double articulating wingsail based on NACA 0020. The XFOIL results were found to agree with two-dimensional CFD. Malmek *et al.* (2020) developed an efficient method based on the lifting-line theory of potential flow in combination with CFD data that was obtained by solving the two-dimensional Reynolds-averaged Navier–Stokes equations (RANS). On this basis, Malmek *et al.* (2024) used the vortex lattice method (VLM). The theoretical methods provided acceptable forces, moments, and stall predictions, with negligible computational cost compared to three-dimensional CFD simulations. These theoretical methods are typically efficient, especially for thin airfoils at low angles of attack (AOA). Nevertheless, theoretical methods are always based on some assumptions, limiting their applicability to real-world problems. For instance, aerodynamic performance under stall conditions with strong flow separation is typically difficult to accurately calculate by these methods.

It should also be mentioned that hybrid theoretical-empirical methods exist for engineering problems, which adjust theoretical calculations based on engineering experience to compensate for the limitations. Empirical methods provide quick, but approximate solutions, to fluid flow problems, sometimes being limited in their accuracy and reliability. Additionally, when compared with other engineering applications, such as airplane wings and propeller blades, wingsails are a relatively newer concept with a limited history of use in design and operation, leading to rare and underdeveloped empirical methods for predicting propulsive performance.

2.1.2 Numerical simulations

Numerical simulations have some advantages over theoretical simulations. Numerical methods can be used to simulate complex fluid flow problems with high accuracy, providing

visualizations and detailed information about flow characteristics. It has been demonstrated that wingsails with large-camber profiles always suffer from strong flow separation, even with very low AOA, which is difficult to capture using theoretical methods. In such cases, numerical simulations are more appropriate although they have high computational costs.

Numerical studies have been conducted for wingsails with cambered profiles. Ouchi *et al.* (2011); Ouchi *et al.* (2013) proposed the crescent-shaped profile and performed three-dimensional CFD simulations to evaluate the propulsive performance of a nine-wingsail system in full scale. This study indicated that crescent-shaped wingsails can provide appreciable thrust for ship propulsion. Atkinson and Binns (2018) simulated a wingsail with a segment-shaped profile for a wide range of angles of attack (α); the authors reported that the critical angle of attack (α_c) of this kind of profile is notably larger than that of symmetric airfoils. It was shown that wingsails with cambered profiles can provide notably stronger thrust force. Subsequently, Atkinson (2019) studied a multiple wingsail system in three dimensions and found that the system can be significantly improved by adjusting the spacing, orientation, and rotation angles of the wingsails. Nikmanesh (2021) introduced the concept of a crescent-shaped wingsail with round edges and performed two- and three-dimensional CFD simulations based on unsteady RANS (URANS). It was found that the flow field around the wingsail experiences strong separation due to the large camber, as visualized in Figure 4, which leads to significant oscillation of the force coefficients over time.
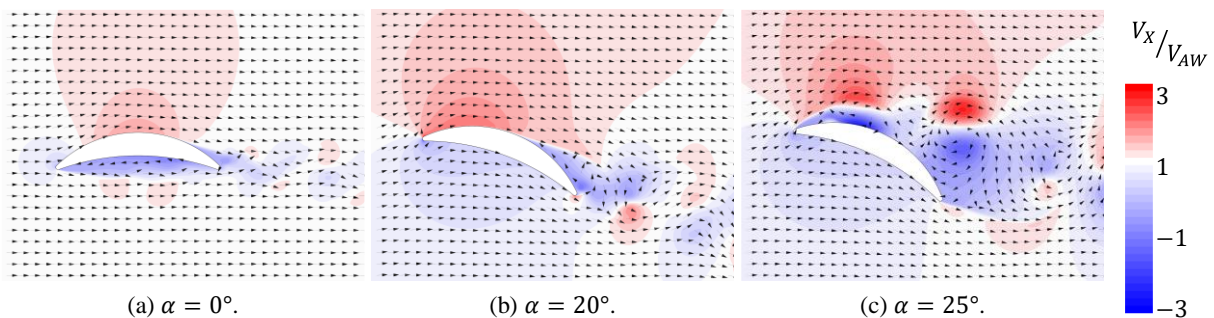
Figure 4. Distribution of the ratio of the streamwise flow velocity (V_X) and the apparent wind speed (V_{AW}) around a crescent-shaped wingsail at different angles of attack (α) (post-processed based on two-dimensional CFD simulations conducted by Nikmanesh (2021)).

Hussain and Amin (2021) considered various drift angles of ship motions, and carried out CFD simulations for a five-wingsail system with a NACA 4412 profile, indicating substantial aerodynamic interactions among multiple wingsails and between wingsails and the ship. Chen *et al.* (2022) applied overset techniques to two-dimensional CFD simulations for a triple-sail system and summarized the effects of sail geometry and position on lift and drag. On this basis, Zeng *et al.* (2023) analyzed the flow around DynaRigs, particularly the wake flow, indicating that the decrease in speed and the oscillations in the wake cause negative effects on the propulsive performance. Based on CFD simulations with RANS, Zhang *et al.* (2023) used particle swarm optimization (PSO) to improve the design parameters of a double-wingsail system. Further, Zhang *et al.* (2024) used RANS to analyze vertical wind gradients, hull-sail interaction, and heeling angles from $-15°$ to $15°$ of a ship. It was found that the heeling angle is detrimental to the propulsive performance.

There have been some numerical studies for other wingsail profiles, such as two- and three-element profiles as mentioned in Section 1.1. Lee *et al.* (2016) studied the NACA 0012 profile and applied optimization techniques to maximize the thrust. Ma *et al.* (2018) studied NACA 23012, NACA 0012, and NACA0018 using RANS with $k-\omega$ shear stress transport (SST) turbulence model. Persson *et al.* (2019) presented simplified approaches to model WASP systems with the NACA 0015 profile. Blount and Portell (2021); Zhu (2020) performed detached eddy simulation (DES) of a NACA 0015 profile under downwind conditions. Li *et al.* (2019) performed two- and three-dimensional CFD simulations for two- and three-element foils, and optimized the foil gap length. Ljungberg (2023) conducted a parametric sensitivity study for two- and three-element wingsails based on two-dimensional URANS and three-dimensional improved delayed detached-eddy simulation (IDDES). The importance of the gap length was highlighted in these studies.

Furthermore, wingsails have been investigated for small sailing boats that are operated at relatively lower Reynolds numbers. For example, Viola *et al.* (2014) performed DES for soft and rigid sails, and compared it with previous WT test results (Viola & Flay, 2012). They found that aerodynamic loads are sensitive to small changes in the Reynolds stresses. Viola *et al.* (2015) carried out a RANS-based optimization for an AC72 rigid wing sail. Zeng *et al.* (2024a) studied a NACA 0012 sail for unmanned vessels at a Reynolds number (Re) of 3.6×10^5 through large-eddy simulation (LES). They explored the unsteady characteristics of the force coefficients, *e.g.*, the spectral features. However, it should be noted that the order of magnitudes of the Re for sails (based on the chord length) on small sailing boats is typically 10^5, while it can be 10^7 for wingsails installed on large commercial ships. From a physics perspective, the differences in Re lead to distinct aerodynamic characteristics, which will be discussed in detail in Section 2.1.3.

As noted by Nikmanesh (2021), crescent-shaped wingsails are prone to strong flow separation, which increases turbulence. As a consequence, structural vibrations induced by vortices are increased. High-fidelity numerical approaches may be required to better resolve and understand these effects. Figure 5 shows the differences among different CFD approaches according to (Salim, 2011). Direct numerical simulation (DNS) resolves all scales down to the Kolmogorov scale of eddies. However, the computational costs of DNS are extremely expensive. LES models sub-grid scales using turbulence models, whereas RANS models all scales (Davidson, 2019; Yao *et al.*, 2008).

DES is a method combining RANS and LES, making it more computationally efficient than LES (Fröhlich & Von Terzi, 2008). In this method, boundary layers are solved using RANS to reduce the requirement on the mesh resolution. The DES length scale (Δ_{DES}) determines the allocation of RANS and LES regions (Davidson, 2019). Zhu (2020) compared different DES approaches, such as DES97 (Spalart, 1997), delayed detached eddy simulation (DDES) (Spalart *et al.*, 2006), and IDDES, in the context of wingsail analysis (Shur *et al.*, 2008). It was found that IDDES provided the most reasonable allocations of the RANS and LES regions, as shown in Figure 6.
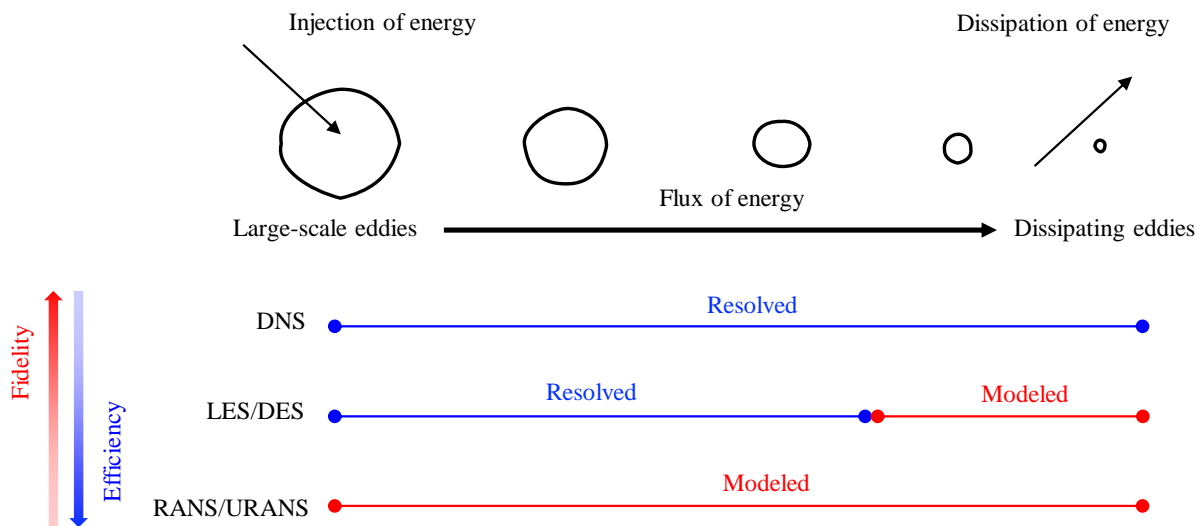
Figure 5. CFD approaches for resolving turbulent flow (regenerated from Salim (2011)).

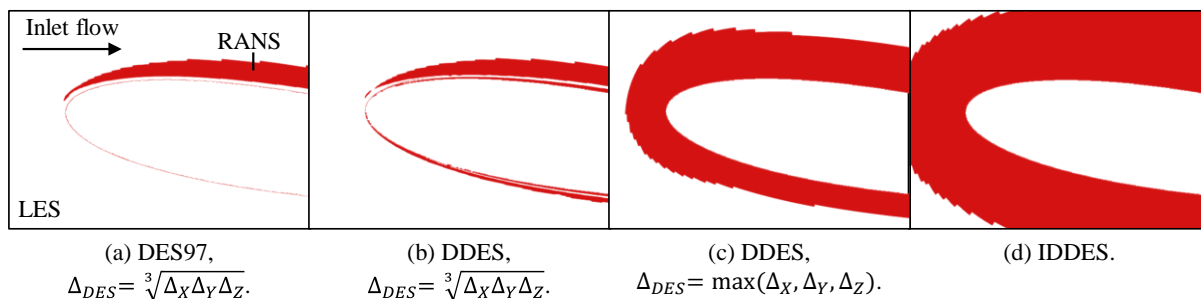| (a) DES97,	(b) DDES,	(c) DDES,	(d) IDDES.
$\Delta_{DES} = \sqrt[3]{\Delta_X \Delta_Y \Delta_Z}$.	$\Delta_{DES} = \sqrt[3]{\Delta_X \Delta_Y \Delta_Z}$.	$\Delta_{DES} = \max(\Delta_X, \Delta_Y, \Delta_Z)$.	

Figure 6. Distributions of LES and RANS regions based on Δ_{DES} in different DES approaches, near the leading edge of NACA 0015 at $Re = 1 \times 10^7$ (Zhu, 2020).

2.1.3 Experimental tests and model-scale effects

Although numerical simulations provide a comprehensive analysis of aerodynamic characteristics, experimental tests are usually necessary for validation. In recent years, model-scale WT tests have been conducted for wingsails. Burden *et al.* (2010) investigated wingsail spacing, stagger, and wingsail-container interactions, to maximize the performance of a multi-wingsail system. Hu *et al.* (2012) proposed a concept called ellipse wingsails, the sectional profile of which is similar to a crescent-shaped profile, tested the model-scale wingsail in a WT, and found that the aerodynamic performance of this wingsail profile is better than arc-shaped profiles. Furukawa *et al.* (2015) studied two wingsails with different symmetrical profiles at low Re. Bordogna *et al.* (2018) measured a single sail and a two-sail arrangement. Zhang *et al.* (2022) addressed the parametric sensitivity of arc-shaped wingsails. Giovannetti *et al.* (2022) analyzed the sail interaction for a triple-wingsail system for a Re above 1×10^6. Nevertheless, these WT tests were primarily for conventional airfoil profiles without cambers, *i.e.*, the NACA series. Cambered profiles have not been extensively studied in the context of vortex shedding, as well as flow separation and reattachment.

Additionally, experimental studies have been conducted for sailing yachts (Viola, 2013). The sectional profiles of sails have typically been simplified as a cambered arc with sharp edges in previous studies (Larsson, 1990; Viola, 2013). For example, Viola and Flay (2012) measured the pressures on three horizontal sections of a downwind sail for several wind directions and

sail trims. Aubin *et al.* (2018) measured the effects of a flapping leading edge for a spinnaker in a WT. Yin *et al.* (2023) carried out outdoor experiments to analyze coupling parameters for arc sails of unmanned sailboats. Souppez and Viola (2024) used water tunnel tests with particle image velocimetry (PIV) to analyze wings with low aspect ratios, large cambers, and sharp leading edges.

It is worth noting that the Re achieved in WT tests is generally on the order of 10^5, which is similar to those of full-scale yachts. However, for large commercial ships, the order of the Re is normally 10^7 (Malmek *et al.*, 2024), raising the question of whether model-scale WT test results remain valid for full-scale configurations, *i.e.*, the dependence of the aerodynamics on Re.

It is necessary to address the model-scale effects of experiments to fill the knowledge gap above. The viscous effect is a classic perspective, and the Re sensitivity of curvature geometries has been investigated for decades (Forouzi Feshalami *et al.*, 2022). In cambered geometries, flow separation ordinarily occurs under moderate- and high-Re conditions even at low angles of attack (α), *e.g.*, $\alpha = 0°$ (Souppez *et al.*, 2022; Tank *et al.*, 2021). Consequently, the characteristics of the resulting flow field share similarities with those induced by bluff bodies, *i.e.*, non-streamlined objects (Rockwood & Green, 2019). Studies on the model-scale effects of typical bluff bodies, such as cylinders and prisms, can be traced back to decades ago (Williamson, 1996). Among all these reviewed studies, the circular cylinder most closely resembles the suction side of the cambered profiles depicted in Figure 2 (Souppez *et al.*, 2022).

In the field of aeronautical engineering, the model-scale effects of cambered airfoils are also of interest. Bot *et al.* (2016) conducted water tunnel experiments for an arc-shaped foil and found that the foil suffers from lift and drag crises, *i.e.*, the force coefficients sharply drop at a critical Re. Nava *et al.* (2016) detected similar phenomena in water tunnel tests. Tank *et al.* (2021) analyzed the flow transition for a cambered airfoil at moderate Re in a wide range of AOA. Souppez *et al.* (2022) analyzed the leading-edge separation bubble (LESB) for an arc profile. However, these previous studies mainly focused on low or moderate Re. There are few studies for high-Re conditions ($Re > 10^6$), where the laminar-turbulent transition happens very early and the turbulent flow dominates the boundary layer. Besides, in WT tests, the inlet wind velocity (V_∞) is usually high to make Re as close to the real condition as possible. For example, if V_∞ is 100 m/s, the Mach number (Ma) is approaching 0.3, leading to compressibility effects.

In addition to the viscous effects in tests, blockage effects and wall interferences are also caused by surrounding tunnel walls (Forouzi Feshalami *et al.*, 2022). Studies of blockage effects have been conducted for several decades. However, most have focused on low Re from 10^3 to 10^5 (Madhavan *et al.*, 2014; Rehimi *et al.*, 2008), which is approximately 2–3 orders of magnitude lower than the practical operation of wingsails and one order of magnitude lower than the model-scale WT tests. In addition, the majority of previous studies were based on circular or rectangular cylinders. The flow field around cambered profiles, particularly on the pressure side, exhibits distinct characteristics, which have been rarely studied. Although the thickness of the boundary layers near tunnel walls should be much thinner at high Re, the influence on the aerodynamic loads has not been quantified. That is, it is unclear whether the wall interferences are negligible in the measurement of aerodynamic loads.

2.2 Structural response analysis

Wingsail structures must be strong and sufficiently durable to withstand the bending moment caused by wind loads. Hence, investigating the structural responses of crescent-shaped wingsails, including ultimate strength, fatigue characteristics, and the response to operational loads, particularly regarding plastic deformation, is of significant interest. DNV has released a standard for WASP systems (DNV-ST-0511) (DNV, 2022), which provides strength and fatigue criteria for wingsail structures.

2.2.1 Structural design and analysis

Though the concept of wingsails has been proposed for decades, mature structural designs for wingsails are very limited. The three ships mentioned in Section 1.1 (*Shofu Maru*, *New Vitality*, and *New Aden*) are equipped with crescent wingsails, which have many vertical stiffeners to bear the global bending and torsion (Ma *et al.*, 2022; Ouchi *et al.*, 2013; Wang *et al.*, 2022). This structural design strategy is commonly seen in naval architecture, as the hull structures of ships are always arranged in this way. On the other hand, the wingsail structure can usually be considered a cantilever, and the wind load is a distributed load on the wingsail surface. Therefore, the boundary and loading conditions of wingsails have greater similarity to those of airplane wings (Sofla *et al.*, 2010) and wind turbine blades (Chen *et al.*, 2013), which mainly use a strong internal frame, *e.g.*, a spar, to bear the global bending. Although gravity acts in the spanwise direction of the wingsail, it has a minimal impact on the global bending moments compared to the aerodynamic loads distributed along the wingsail surface. Consequently, structural analysis of wingsails focuses primarily on the effects of wind loads rather than gravity (Zhu *et al.*, 2023).

Currently, finite element analysis (FEA) has been utilized to compute wingsail structures. Ouchi *et al.* (2011); Ouchi *et al.* (2013) proposed a conceptual design for a telescopic rigid wingsail and analyzed deflection and stress distribution. Hu *et al.* (2015) investigated the structural design, dynamic performance, and control strategy for large, ocean-going, sail-assisted ships. Additionally, Hussain and Amin (2021) conducted static FEA for cambered wingsails. It was noted that the stress value is maximum in the mast, but much lower in the sail shells.

However, the above studies were preliminary structural analyses based on static FEA. Revealing structural responses due to unsteady aerodynamic load requires the application of dynamic FEA coupled with CFD. In addition, the telescopic function makes the structural design more complex, which further complicates modeling.

2.2.2 Aeroelasticity analysis

Due to its camber, a crescent-shaped wingsail induces strong flow separation, which results in vortex-induced vibration (VIV) and fatigue (Storhaug *et al.*, 2022). These structural deformations can in turn affect the flow field. Consequently, it is necessary to fully understand wingsail aeroelasticity in relation to the FSI (Bak *et al.*, 2013; Souppez, 2023).

Studies on wingsail aeroelasticity are rarely seen in the literature, necessitating the reliance on findings from other FSI case studies. The Tacoma Narrows Bridge is a well-known FSI problem (Matsumoto *et al.*, 2003). From the perspective of global bending and torsion, if the eigenfrequency (f_e) of the structure is similar to the vortex shedding frequency, resonance may

occur, leading to relatively strong structural responses (Billah & Scanlan, 1991). It should also be mentioned that due to turbulence, the light-weight panels of a wingsail can also vibrate (Thies & Fakiolas, 2022).

In FSI simulations, the coupling between fluid and structural domains can be classified as one-way or two-way. The solution algorithms illustrated in Figure 7 use FSI simulations based on CFD and FEA as an example, (Bazilevs *et al.*, 2013; Benra *et al.*, 2011; Bisplinghoff *et al.*, 2013; Ezkurra *et al.*, 2018). In one-way coupled FSI, the fluid forces act on the structure, but the structural response does not influence the fluid flow. This approach assumes that the structural deformations have a sufficiently negligible effect on the fluid domain, making it computationally less expensive but limiting its accuracy in scenarios where fluid-induced deformations are significant. In contrast, two-way coupled FSI accounts for the influence on the flow field due to structural deformation. The fluid exerts forces on the structure, causing deformations, while the structural response, in turn, alters the fluid flow. This two-way coupled method is more accurate for complex, highly interactive systems but requires significantly greater computational resources for solving both fluid and structural equations simultaneously.
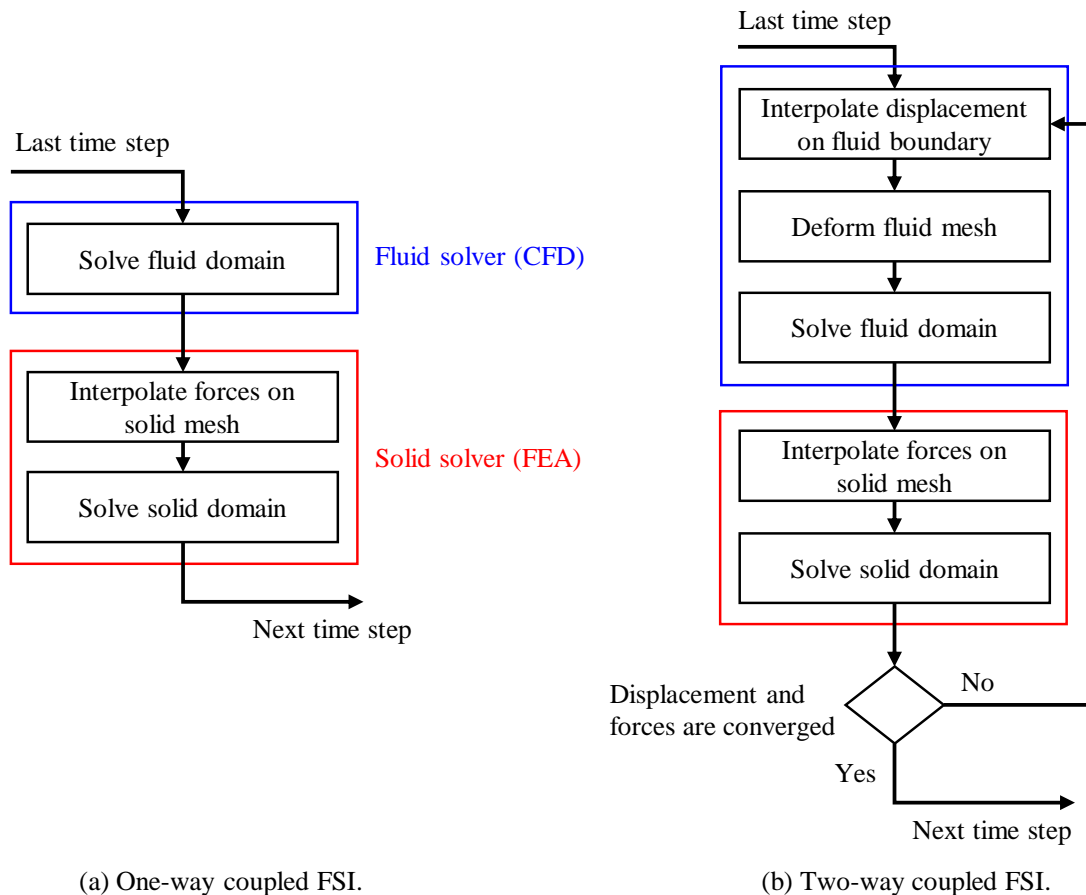
(a) One-way coupled FSI.   (b) Two-way coupled FSI.

Figure 7. Solution algorithms for one- and two-way coupled FSI simulations based on CFD for fluid and FEA for solid (regenerated from Benra *et al.* (2011); Ezkurra *et al.* (2018)).

The Arbitrary Lagrangian–Eulerian (ALE) method is commonly employed in FSI simulations to deal with the dynamic coupling between fluid and solid domains (Bazilevs *et al.*, 2013; Richter, 2010). In FSI problems, the fluid domain often has significant deformations. Unlike purely Lagrangian methods, where the mesh moves with the structure, or Eulerian methods,

where the mesh remains fixed, the ALE approach allows the mesh to move arbitrarily, enabling the ALE method to mitigate excessive mesh distortion in the fluid domain while accurately tracking structural boundaries. The ALE method maintains computational accuracy and stability by updating the mesh in a controlled manner, making it especially useful in simulations involving large deformations, such as flexible structures interacting with turbulent fluids (Basting *et al.*, 2017).

Considering similar structures to wingsails, many studies on two-way coupled FSI simulations applied to airplane wings (Ajaj *et al.*, 2021) and wind turbine blades (Ageze *et al.*, 2017; Della Posta *et al.*, 2021; Della Posta *et al.*, 2022) have been conducted in recent years. Among these, aeroelasticity, which is specifically concerned with the interaction between aerodynamic forces and structural elasticity, is frequently focused (Bisplinghoff *et al.*, 2013). These simulations aim to predict how aerodynamic forces cause structural deformations and how these deformations alter the flow field. The structural models are usually simplified and considered linear elastic in aeroelastic simulations, making these simulations cost-effective.

2.3 Energy saving evaluation

Several studies have been carried out to analyze and evaluate the propulsive performance of WASP systems. Kijima *et al.* (1990) developed the velocity prediction program (VPP). Ship motions are solved in terms of aero- or hydrodynamic forces and moments (Larsson, 1990).

Ouchi *et al.* (2013) conducted voyage simulations to estimate the reduction of fuel consumption of a ship equipped with Wind Challenger wingsails in the real sea. They also optimized the shipping route based on the WASP performance. Tillig *et al.* (2017) developed a generic ship energy system model, including the VPP and the power prediction program (PPP). This model was later named ShipCLEAN (Tillig *et al.*, 2019). It is aimed at predicting the fuel consumption of ships at sea while considering the external loads caused by several factors, such as wind, waves, and currents, using this model, Lu and Ringsberg (2020) compared the true fuel savings of three sail technologies (the Flettner rotor, the DynaRig, and a wingsail) for a specific ship sailing in specific voyage routes, showing that WASP technologies reduced fuel consumption by several percentage points but not as much as expected. One of the crucial factors found was the sail performance related to the heading direction of the ship. The performance also depends on the aerodynamic interactions among multiple sails.

3   Methodology

This Chapter presents the benchmark crescent-shaped wingsails and methods that are developed or applied in this thesis. This thesis investigates the aerodynamic and aeroelastic performance of crescent-shaped wingsails. The framework consists of several stages that systematically address the research objectives through a combination of conceptual design, numerical simulations, experimental validation, and long-term performance analysis, as illustrated in Figure 8.
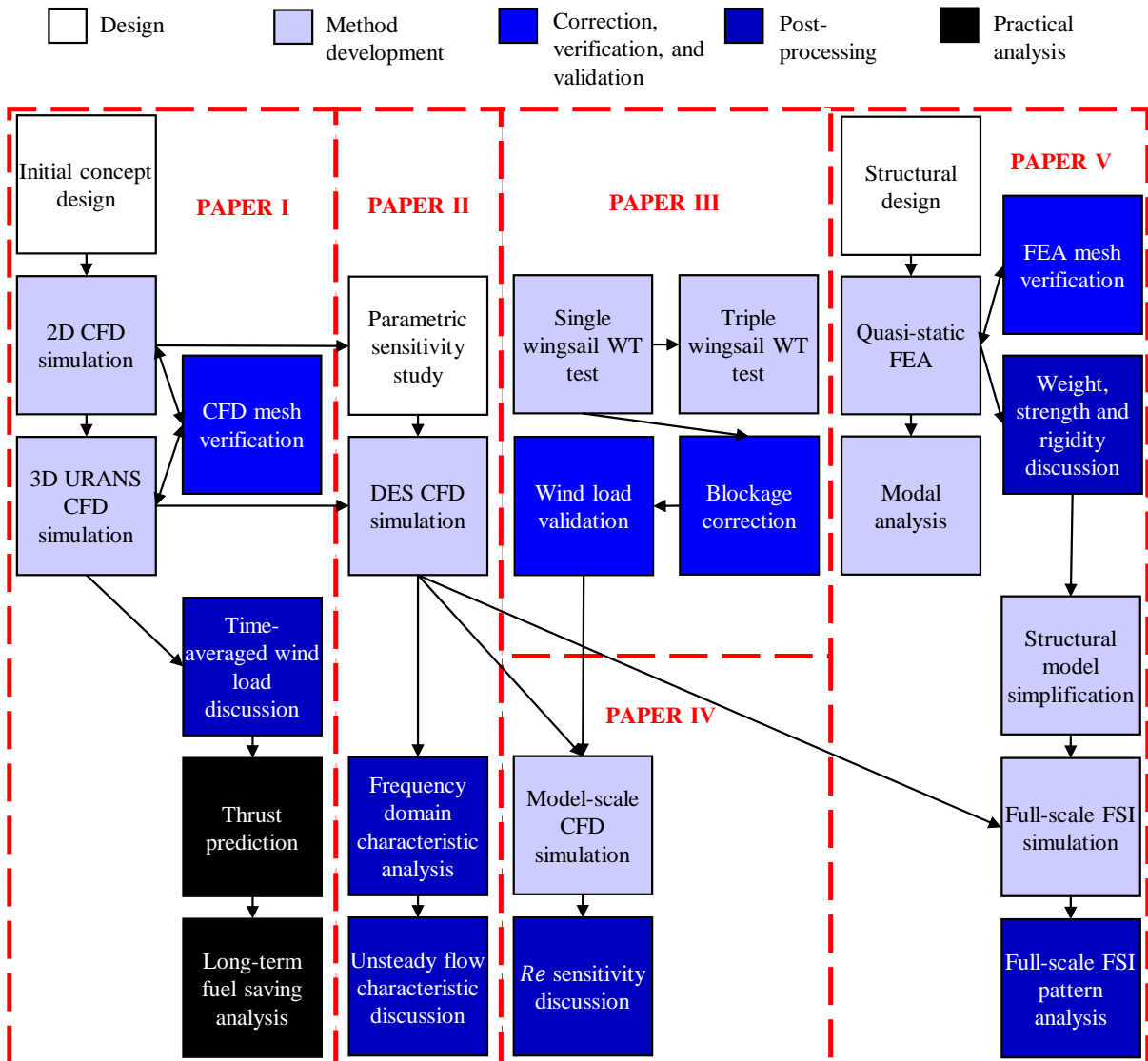
Figure 8. Research path and framework.

The research process begins with the initial concept design, followed by CFD simulations based on URANS to refine the aerodynamic properties of the wingsail. Mesh verification is carried out at this stage to ensure accuracy. This is further expanded into CFD simulations based on IDDES to capture unsteady aerodynamic behavior. The aerodynamic results are validated against WT tests, considering the model-scale effects. The structural integrity is analyzed using FEA, including quasi-static FEA, modal analysis, and frequency domain characteristic analysis, with an emphasis on structural design and model simplification. This leads to a comprehensive

two-way coupled aeroelastic simulation to predict how the wingsail behaves under wind-induced deformation. The propulsive performance is calculated based on the principle of sailing, while the long-term energy performance is estimated by ShipCLEAN.

3.1 Study benchmarks

3.1.1 Conceptual design

A conceptual design of telescopic wingsails with crescent-shaped profiles is selected as the benchmark in this thesis, as shown in Figure 9.

(a) Design parameters of the crescent-shaped profile.

(b) Schematic diagram of the telescopic function.

(c) Design of triple-wingsail arrangement.

(d) Two concepts of structural designs .
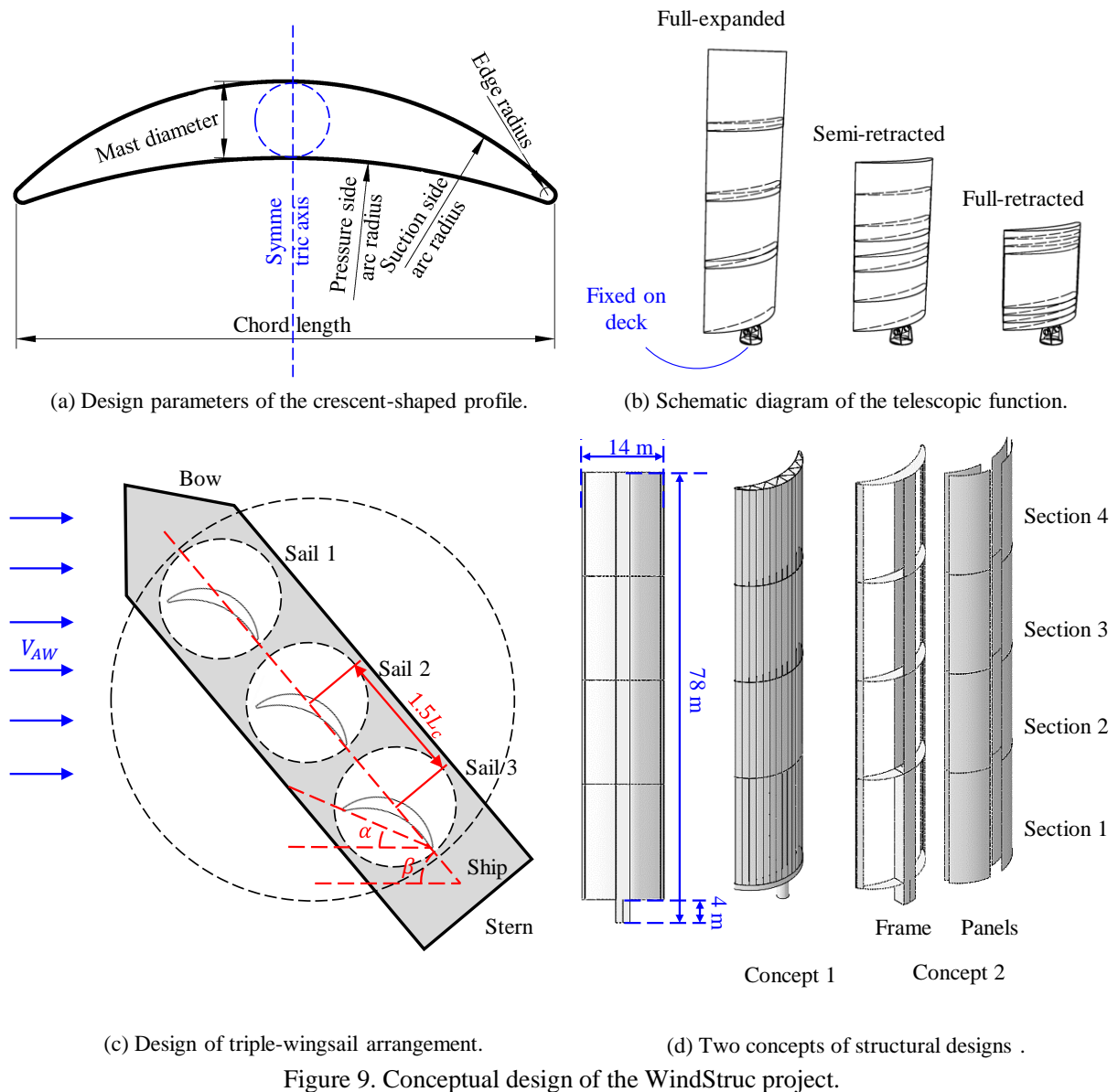
Figure 9. Conceptual design of the WindStruc project.

3.1.1.1 Crescent-shaped profile

The crescent-shaped profile is a simple geometry that is comprised of arcs and circles, as illustrated in Figure 9(a). The shape is controlled by four main design parameters: the chord length (L_c), edge radius, suction-side arc radius, and mast diameter. The L_c is held constant at

14 m, and the edge radius is 0.2 m. The dimension parameters are suggested by ScandiNAOS AB according to its practice.

A series of profiles are generated and labeled as "DxRy," where "x" represents the mast diameter and "y" represents the suction-side arc radius. For example, for the profile named "D2R8," the mast diameter is 2 m and the suction-side arc radius is 8 m, which results in an arc radius of 10.67 m on the pressure side.

3.1.1.2 Telescopic function

The real wingsail has a telescopic function, as shown in Figure 9(b). It is divided into four sections. The wingsail can be expanded at low wind speeds, while it can be semi- or fully retracted to prevent structural failures at high wind speeds. The fully expanded height is 72–74 m, and the fully retracted height is 26 m. The height of the mast section between the wingsail bottom and the deck is 4 m.

3.1.1.3 Triple-wingsail arrangement

Multiple wingsails are installed on ships to capture additional wind power (Li *et al.*, 2017). Figure 9(c) shows a triple-sail system with three wingsails installed along the centerline of the ship. The wingsail design presented in Sections 3.1.1.1 and 3.1.1.2 is followed. The distance between the mast centers is $1.5L_c$, which is suggested by industry experts at ScandiNAOS AB, based on their experience with WASP systems. For the purposes of this discussion, the sail closest to the bow of the ship is referred to as "Sail 1".

3.1.1.4 Structural design

The wingsail should have a lightweight design to reduce its influence on the ship's cargo capacity and fulfill any stability requirements. Another challenge is that wind loads cause bending and torsion in the structure. This increases the required strength-to-weight ratio.

As presented in Figure 9(d), two structural design concepts are proposed and analyzed in this thesis. "Concept 1" uses the global shell structure to bear global bending, so several vertical stiffeners and web structures are used to increase the strength and rigidity. "Concept 2" explores the use of a square prism mast to prevent stress concentration in the mast and reduce the weight of the wingsail rig. The entire structure can be divided into two parts: the frame, which is expected to bear global bending and torsion, and the panels, which are assumed only to suffer under local wind pressure. The mast only extends to the lowest section.

For "concept 1," all parts are made of steel (S275) (BS EN, 2004). In contrast, aluminum (6061-T4) (ASTM, 2004) is used for "concept 2." Detailed information about the material properties can be found in **Paper V**. Two material arrangements are studied in "concept 2": "steel frame, aluminum panels" and "all in aluminum."

In this thesis, each structure is evaluated in terms of its weight, strength, and rigidity. Since there is no guidance for the crescent-shaped structure, **Paper V** formulates a series of conservative criteria listed below. These criteria are suggested by ScandiNAOS AB according to its practice, which is slightly stricter than those proposed by DNV (2022).

• The total weight of the wingsail must be as low as possible.

• The maximum von Mises stress (σ_{Mises}) should not exceed the yield stress. With a safety

17

factor of 2.0, the allowable von Mises stress for steel (S275) (BS EN, 2004) is 140 MPa, while the allowable stress for aluminum (6061-T4) (ASTM, 2004) is 105 MPa. The maximum normal stress in compression should not exceed the buckling stress (σ_{buck}). The buckling stress is calculated based on Euler's formula. For the mast, σ_{buck} is 252 MPa for steel (S275) and 126 MPa for aluminum (6061-T4). The maximum shear stress should be less than 50% of the allowable von Mises stress; therefore, the permissible shear stress is 70 MPa for steel and 53 MPa for aluminum.

- Rigidity or flexibility is also relevant because if the structure is not sufficiently rigid, the telescopic function will not work. The maximum deflection, which usually occurs at the tip, should not be larger than 5% of the full-expanded height. In the fully expanded state, the maximum allowable tip deflection is 3.7 m. The relative displacement of the panels should not exceed half of the mast diameter (*i.e.*, 1 m).

3.1.2 Coordinate systems

For the sake of convenience in expression, a set of Cartesian coordinate systems is introduced, as shown in Figure 10. Figure 10(a) shows the global coordinate system. The X axis is aligned with the inlet flow, *i.e.*, the streamwise direction. The Y axis points from the pressure side to the suction side. The Z axis points vertically upward from the bottom to the top, *i.e.*, the spanwise direction. The origin is located at the wingsail bottom surface. It is at the center of the mean camber line for the crescent-shaped profile, whereas it is located at the leading edge for NACA 0015. When discussing the pressure and shear stress on the surfaces, an in-section coordinate system xOy, as shown in Figure 10(b). The x axis is along the chord. When post-processing FEA results for shell structures, local in-element coordinate systems are defined (Dassault Systemes, 2020), as shown in Figure 10(c). The n axis is normal to the surface.

Crescent-shaped profile ($\alpha = 20°$)

NACA 0015 ($\alpha = 16°$)

Crescent-shaped profile ($\alpha = 20°$)

NACA 0015 ($\alpha = 16°$)

(a) Global coordinate system.

(b) In-section coordinate system.
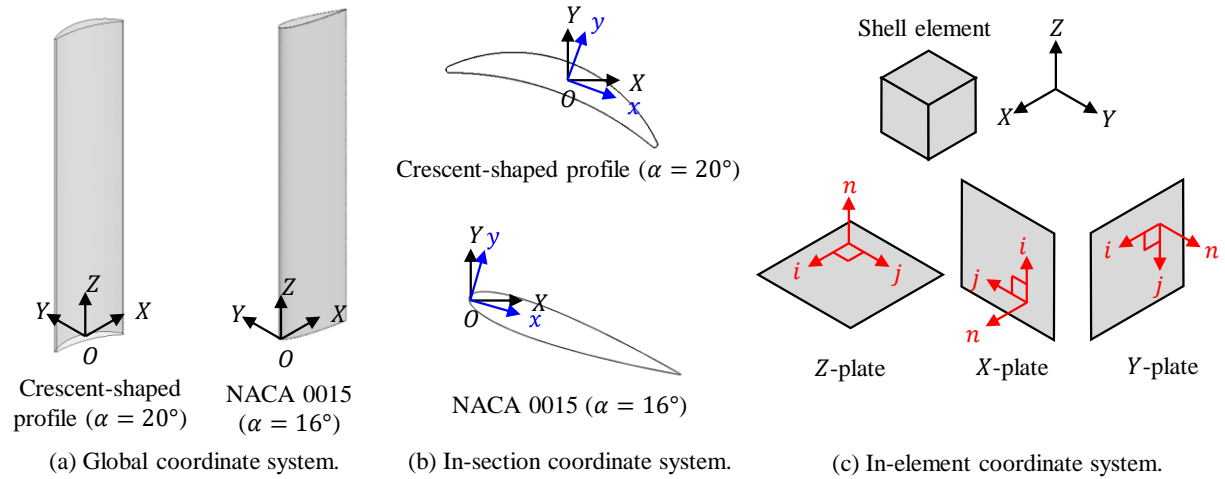
(c) In-element coordinate system.

Figure 10. Coordinate systems.

3.2 CFD

CFD simulations are used to compute flows. The present study uses mesh generators and solvers in the commercial software STAR-CCM+ (Siemens PLM Software, 2021).

3.2.1 CFD simulation model

3.2.1.1 Domain and boundary conditions

The numerical simulations adopt two types of cuboid computational domains, as shown in Figure 11. The dimensions of the computational domains were verified by Nikmanesh (2021). The first type is referred to as "periodic top and bottom", where the sail geometry extends across the entire domain in the spanwise direction. This setup is used to reveal the aerodynamic characteristics of the crescent-shaped profile. The other type is referred to as "symmetry bottom and freestream tip," where the distance between the sail's top end and the domain's top boundary is 4 times the sail's spanwise length. The setup is used to evaluate more realistic flow features, such as tip vortices.

A no-slip boundary condition (BC) is specified at the wingsail walls for both types of computational domains. The domain inlet uses a velocity inlet BC with a uniformly distributed flow speed, corresponding to the apparent wind speed. The side boundaries and outlet are set with a pressure outlet BC, with the pressure loss coefficient set to zero.

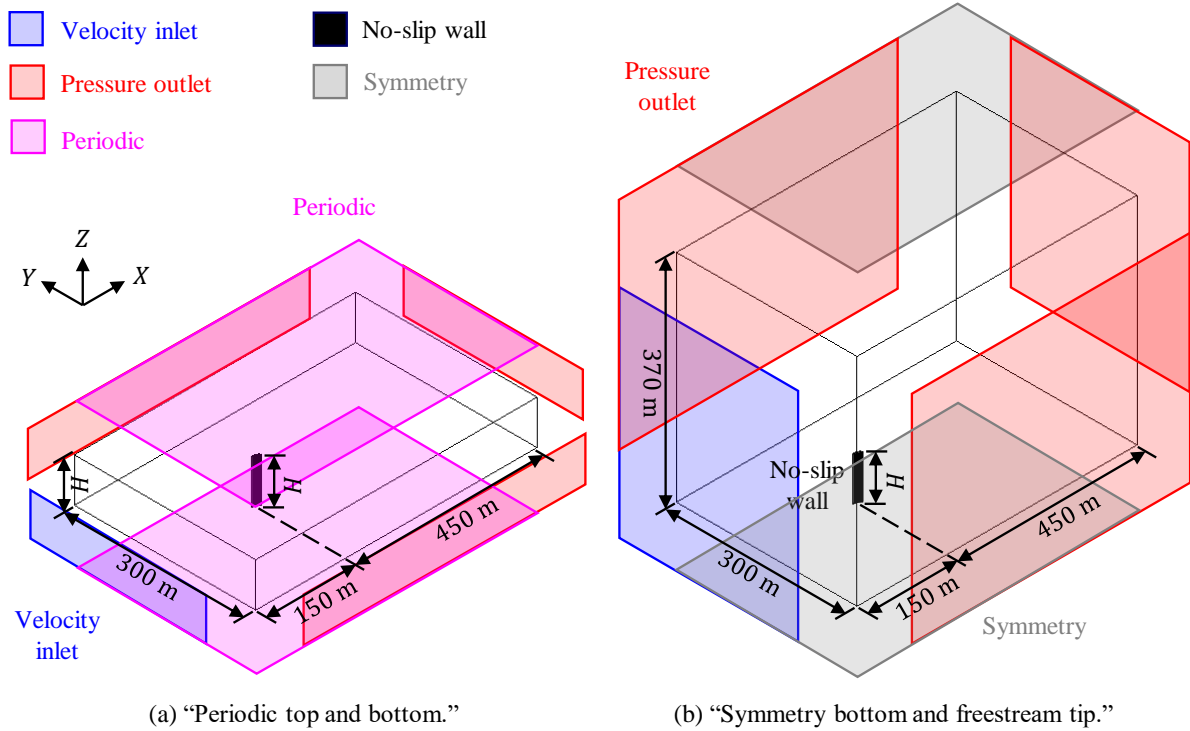(a) "Periodic top and bottom."   (b) "Symmetry bottom and freestream tip."
Figure 11. Two types of computational domains.

3.2.1.2 Meshing and sensitivity study

Unstructured meshes with trimmed cell topologies are used for the simulations. Figure 12 illustrates the "symmetry bottom and freestream tip" mesh. The base size is denoted by l_{base}. The cells maintain a uniform size within each region at each refinement level. Both the regions near the foil and the wake are refined, as shown in the section plane at $Z = 0.5H$ in Figure 12(b). Wake region refinement is controlled by two parameters: the length and separation angle. Additionally, a cylindrical volumetric mesh refinement with a length of $1.1H$ is introduced near the foil. The diameter of this cylinder is $1.4L_c$. Flow separation points are expected to distribute

around the two edges, so refinement is applied near the edges, as shown in Figure 12(c) and (d).

Prism cells are generated to resolve the boundary layers. The absolute total thickness of the prism layer is $0.036 \cdot L_c$, and the number of prism layers is 55. The y^+ of the first-layer cells near the wall is set to be less than 1, while the values in most of the surface areas are approximately 10^{-1}. The near-wall thickness of the prism layer is set to $7.14 \times 10^{-7} \cdot L_c$ to achieve this.
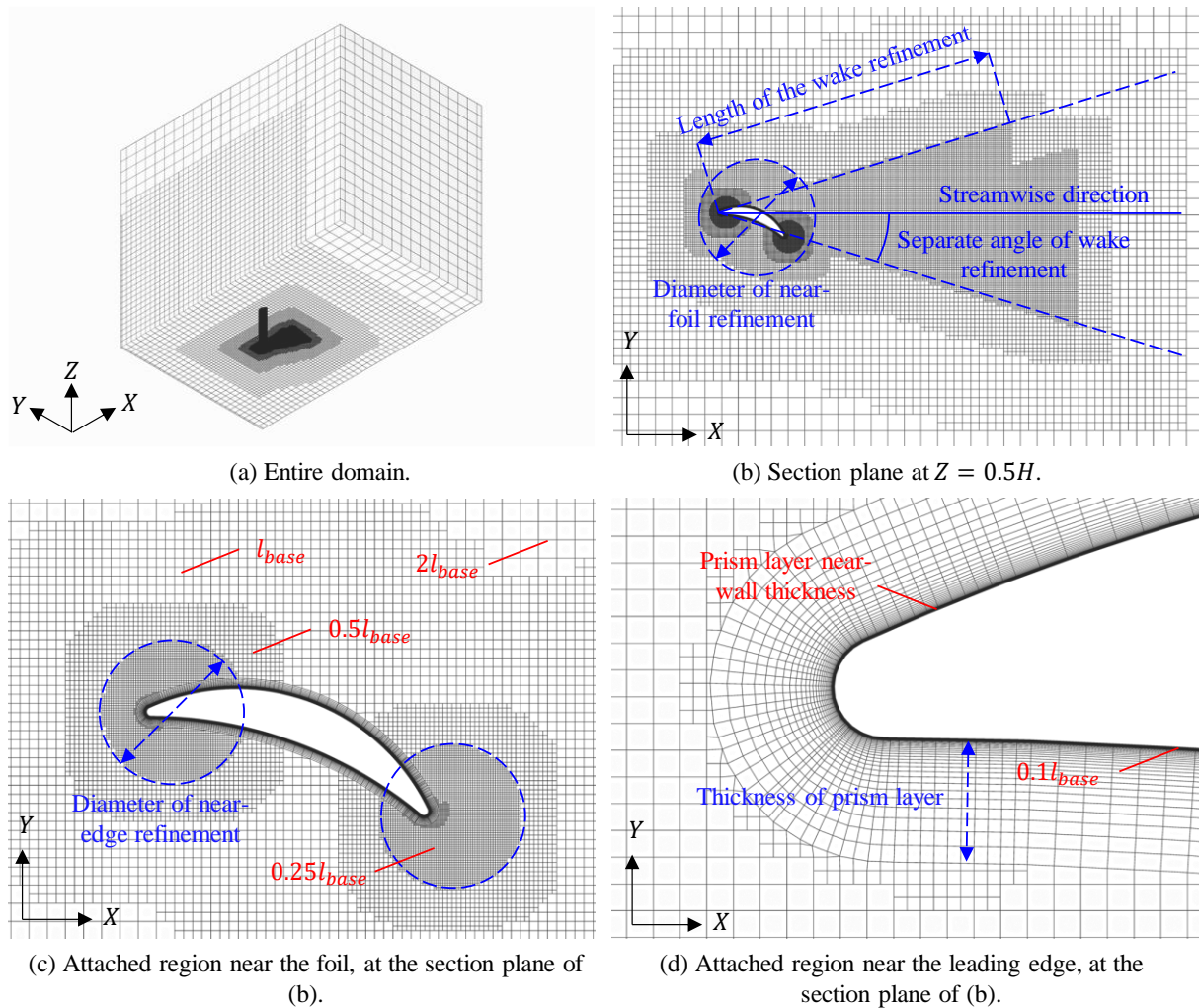

(a) Entire domain.

(b) Section plane at $Z = 0.5H$.

(c) Attached region near the foil, at the section plane of (b).

(d) Attached region near the leading edge, at the section plane of (b).

Figure 12. An unstructured mesh for the crescent-shaped wingsail with the D2R10 profile at AOA of 20°.

A mesh sensitivity study is conducted from two perspectives: the refinement strategy and cell size. The refinement strategy examined three factors to exclude mesh influence: the existence of near-foil refinement, and the length and separation angle of wake refinement. The optimal configuration is determined to be a wake refinement with a separation angle of 0.3 rad and a length of 60 m. The cell sizes in the domain are globally adjusted by changing the base cell size. Detailed information regarding the mesh sensitivity study can be found in **Paper I**.

3.2.2 Turbulence modeling

As reviewed in Section 2.1.2, significant flow separation was observed for the crescent-shaped wingsails. When studying propulsive performance, it is sufficient to solely consider time-

averaged loads. However, unsteady characteristics should also be considered when analyzing structural response. Low-frequency fluctuations of the external loads may cause VIV of the entire sail, and high-frequency fluctuations may cause local vibrations within the shell panels. Accurately simulating turbulence requires the introduction of LES or DES, since sub-grid scales are modeled in these methods (Davidson, 2019; Salim, 2011; Yao *et al.*, 2008). However, the LES method imposes costly near-wall meshing requirements. Therefore, the DES method of IDDES is selected for use in this work. The k–ω SST turbulence model is applied to the IDDES (Shur *et al.*, 2008). This model is also used for the URANS simulations.

The blended wall treatment approach (Workinn, 2021) is applied to the RANS equations in both IDDES and URANS, offering the advantage of accommodating complex geometries with varying local flow characteristics. Given that the velocity over complex walls varies and the geometry of the wingsail profile exhibits curvature, it is difficult to ensure that y^+ in all cells adjacent to the walls are either above or below specified values, as required in a conventional wall treatment model. In contrast, the blended wall treatment adapts to local y^+. Blended wall laws are employed to model smooth variable changes in the buffer layer between the viscous sublayer and the logarithmic region.

At high Reynolds numbers, the laminar-turbulent transition can occur very early, leading to turbulence-dominated boundary layer. Therefore, transition models are not applied in high-Re simulations for full-scale wingsails. However, the γ transition model (Menter *et al.*, 2015) is included in moderate-Re simulations for model-scale wingsails.

3.2.3 Discretization schemes and solvers

The finite volume method (FVM) is utilized to discretize the governing equations. This method employs a segregated flow solver based on the semi-implicit method for pressure-linked equations (SIMPLE) algorithm (Patankar, 1980). It is worth noting that the flow is assumed to be incompressible because of the low freestream Mach number.

Convection fluxes on cell faces are discretized using a hybrid second-order upwind and bounded-central scheme, while diffusion fluxes on both the internal and boundary cell faces are discretized with a second-order scheme. The second-order hybrid Gauss-LSQ method is applied in gradient computation, which involves the reconstruction of field values at a cell face. This includes the secondary gradients of the diffusion fluxes and pressure gradients, as well as the rate-of-strain tensors used in the turbulence model. A second-order implicit method is utilized to discretize the time derivative, and the Reichardt law (Reichardt, 1951) is utilized for the momentum equations.

3.3 WT test

A series of WT tests are carried out to validate the numerical simulations. In the WT tests, the aerodynamic loads on the wingsails are measured.

3.3.1 WT facilities

The WT is located at the Laboratory of Fluids and Thermal Science, the Department of Mechanics and Maritime Sciences, Chalmers University of Technology. A schematic of the WT is shown in Figure 13, which has a closed test section. A motor and fan are installed in the return channel to drive air within the closed circuit. A honeycomb and three screens are utilized

upstream of the test section to homogenize the speed and direction of airflow. An air gap is created at the rear end of the test section to regulate the pressure.

The inlet velocity is controlled using the graphical interface of LabVIEW VI. The maximum tested inlet velocity is 40 m/s. The environmental conditions, such as the temperature, air density, and viscosity, are monitored during the tests. The turbulence length scale is maintained below 0.1% under normal testing conditions in the present study.
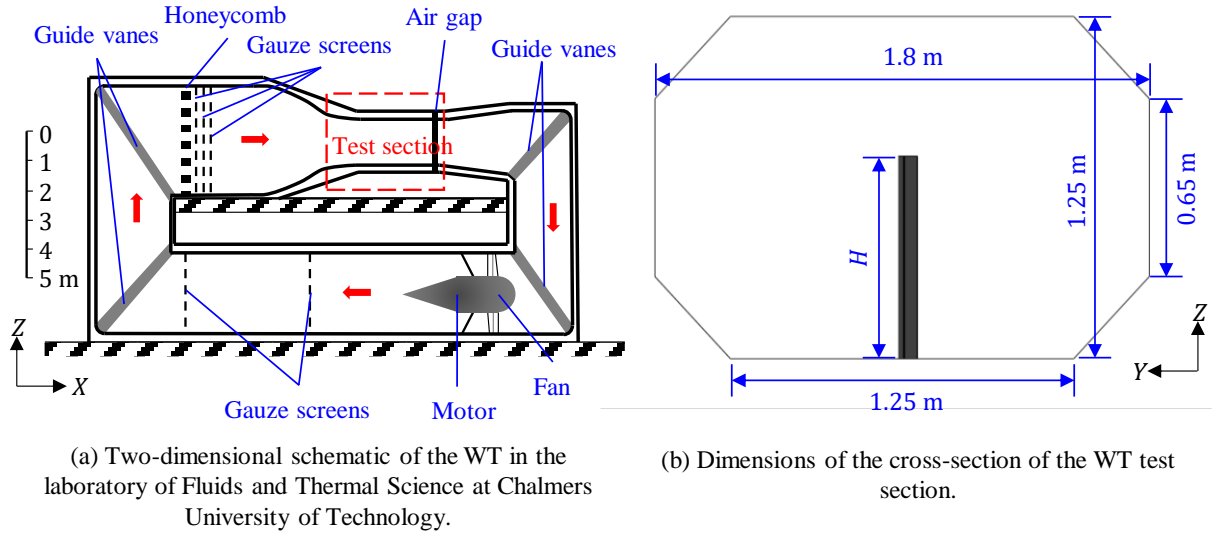

(a) Two-dimensional schematic of the WT in the laboratory of Fluids and Thermal Science at Chalmers University of Technology.

(b) Dimensions of the cross-section of the WT test section.

Figure 13. Schematic of the Chalmers WT.

3.3.2 Wingsail models of WT tests

The test models are made of aluminum. The model is on a scale of $1:100$, *i.e.*, the chord length (L_c) is 0.14 m and the height H is 0.74 m.

The tested layouts are a single model and a triple-line-up model, as shown in Figure 14. The deck holding the test models is designed to rotate to control the AOA and apparent wind angle (AWA). A gearbox is installed beneath the deck panel to control the rotation. The distance between the rotational axis of each sail in the triple model is $1.5L_c$.

A rough sand-paper tape (Borgoltz *et al.*, 2019) with a thickness of $0.0036 \cdot L_c$ and a width of $0.036 \cdot L_c$, is attached to the sail surface at 10% of the chord near the leading edge to trigger the transition from laminar to turbulent flow. This location is based on the laminar-turbulent transition position indicated by the full-scale CFD simulations in **Paper II**.

3.3.3 Measurement

An external balance is placed under the floor of the test section to measure lift and drag forces. The balance is adapted to hold the deck installed with wingsail models. The balances are connected to LabVIEW, which displays measured data in real time. The method of calculating the force coefficients, *i.e.*, C_L and C_D, is presented in **Paper III**.

The total pressure is measured with two Pitot probes that are set upstream and downstream of the test model. An automated traversing system controlled by LabVIEW is used to move the downstream Pitot tube during the tests. The flow velocity is measured with hot-wire

anemometer sensors, which are made of tungsten with a length of 1 mm and a diameter of 5 μm. The hot wire is operated at an overheat ratio of 1.7.

The absolute pressure and the temperature in the wind tunnel are measured with dedicated sensors and logged during the tests. The measurements exhibit negligible differences, so both variables are assumed constant in the analysis.
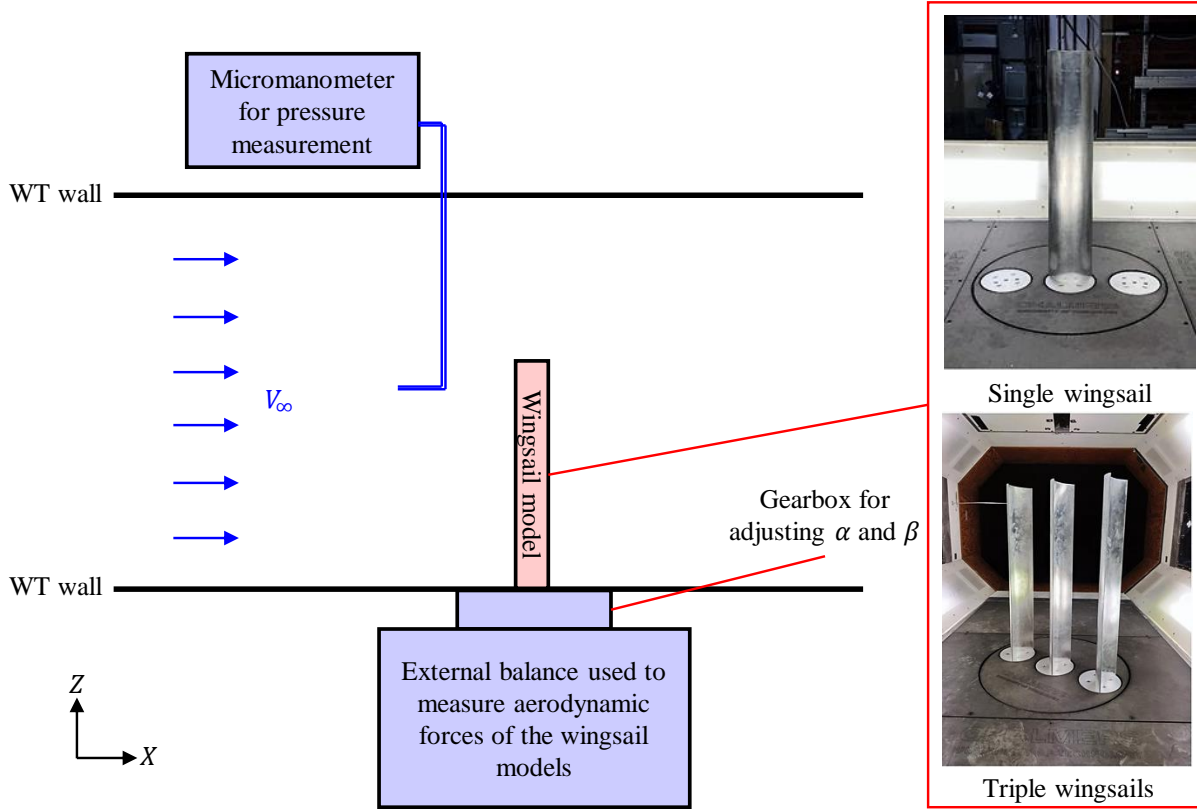

Figure 14. Schematic of WT test setup.

3.3.4 Correction and verification

Two types of wall interference are considered: the boundary layer flow of the WT floor and the blockage effect (Hoang & Bui, 2019). The measured momentum thickness is less than 5 mm and the measured boundary layer thickness on the WT floor is less than 25 mm. These values are similar to those estimated using Equation (1) (Schlichting & Gersten, 2016).

$$\delta_{99}(X) \approx 0.37 \frac{X}{Re_X^{0.2}} \tag{1}$$

Since the boundary layer on the WT floor is not thicker than 2% of H, its influence on the wingsail aerodynamic loads is neglected.

Additionally, since the physical presence of the wingsail model reduces the cross-sectional area of the WT test section, an acceleration of the airflow around the model is induced, *i.e.*, the solid blockage. The blockage ratio, *i.e.*, the ratio between the frontal area of the wingsail models (A_F) and the streamwise sectional area of the WT test section (A_{WT}) varies with α. For a single wingsail model, the blockage ratio ranges from 1.59% ($\alpha = 0°$) to 4.97% ($\alpha = 90°$). The

blockage effects can be corrected by introducing a blockage correction coefficient (Barlow *et al.*, 1999). Then, the corrected drag force coefficient (C_D) can be obtained as Equation (2).

$$C_D = (1 - \frac{A_F}{A_{WT}})^2 \cdot C_{D\_Mea} \tag{2}$$

where C_{D_Mea} represents the drag force coefficients based on the measured force. The corrected lift force coefficient (C_L) is calculated similarly. For a single full-expanded wingsail at AOA of $\alpha = 90°$, the force coefficients are overestimated by approximately 9.69%, while the overestimation is approximately 10.11% for the triple-sail system at $\alpha = 20°$.

Four sets of verifications of measurement consistency are conducted:

- A before- and after-check of both 6-component balances by applying known loads.

- A cross-check of the aerodynamic forces measured by the two balances.

- A cross-check of consistency between the integral aerodynamic pressure load and the lift force.

- A cross-check of consistency between the momentum deficit in the wake (Betz, 1925; Laboratory, 1936) and the drag force.

All sets of verifications produced satisfactory results, leading to the conclusion that the measurements provide reliable data with acceptable margins of error.

3.3.5 CFD validation against WT tests

The time-averaged lift and drag coefficients ($\langle C_L \rangle$ and $\langle C_D \rangle$) are compared with WT results to validate the CFD simulations, as shown in Figure 15. The WT tests are described in Section 3.3. Two series of tests have been conducted at $Re = 3.6 \times 10^5$: one with sand-paper tapes to trigger the laminar-turbulent transition, and the other without any triggering addons. Using sand-paper tapes is widely adopted in aerodynamic testing to trigger early boundary layer transition from laminar to turbulent, thus better approximating the flow conditions experienced in real-world applications (Borgoltz *et al.*, 2019). A good overlap of CFD and experimental data without tape for $Re = 3.6 \times 10^5$ can be seen. Besides, the force coefficients of the CFD simulations at the highest Re agree well with the experimental data with sand-paper tapes, which suggests that using the tripping can help to simulate the high Re aerodynamics in low-Re experiments. The CFD simulation presented in this study is considered convincing.

3.4 FEA and FSI

In addition to studying the aerodynamic characteristics, another objective is to investigate the structural responses of the wingsail structures. FEA is used to analyze the stress and strain distribution, eigenfrequencies, and dynamic structural deformation resulting from aerodynamic loads. This section introduced the structural analysis methods based on quasi-static FEA that are applied to detailed internal structures.

3.4.1 Quasi-static FEA

Quasi-static FEA is performed to compare different structural design concepts and provide an overview of structural integrity. Structural analysis of the full-expanded wingsail is based on

the apparent wind speed of $V_{AW} = 16$ m/s. The external load is divided into the forces on the pressure and suction sides of the wingsail. Both forces are assumed to be uniformly distributed. According to the CFD results, the magnitude of the total force on the suction side is approximately twice that on the pressure side. The gravity of the wingsail structure (*i.e.*, the inertia loads due to self-weight) is ignored since it does not significantly influence the stress distribution (Zhu *et al.*, 2023).
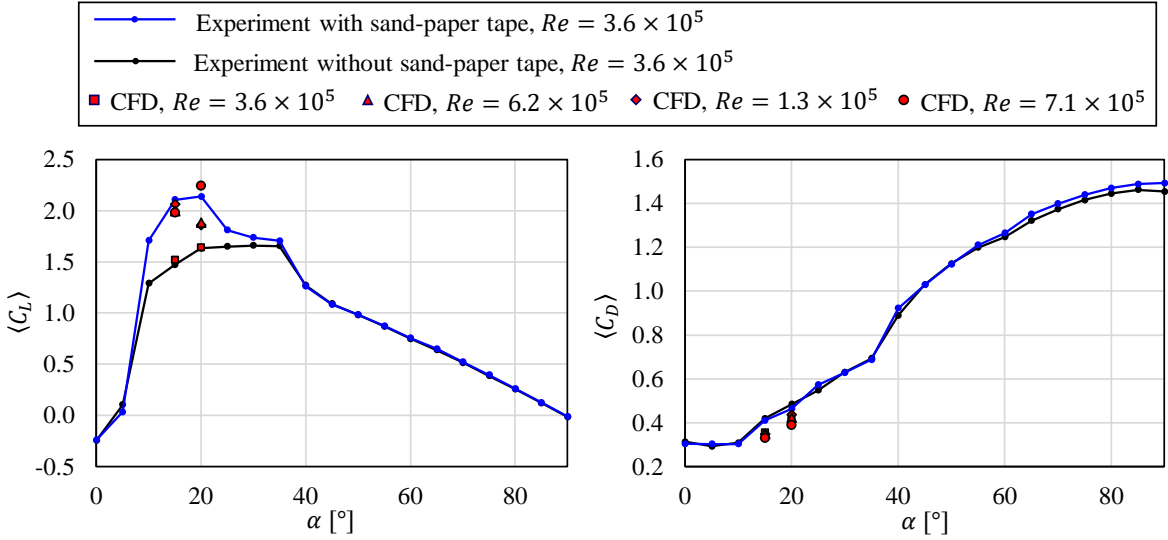

Figure 15. Comparison of $\langle C_L \rangle$ and $\langle C_D \rangle$ between WT tests and CFD simulations.

A cantilever boundary condition is applied. The bottom of the mast is fixed, so no translation or rotation is allowed. The structure of the sail panels is modeled as a group of shell elements in the quasi-static implicit FEA. Five thickness integration points are set, and Simpson's Rule is applied for integration. Each pair of sub-parts is tied together at the contact surface for the strong frame of "concept 1," as shown in Figure 9(d), to ensure that there is no relative motion between them. However, the panels are allowed to have small relative tangential displacements in the vertical direction since the panels are not expected to bear global bending. The FEA are performed using the commercial software ABAQUS (Dassault Systemes, 2020). The geometrical nonlinearities are accounted for by enabling the NLGEOM option in ABAQUS (Mian *et al.*, 2014).

A quad-dominated mesh is applied to the FEA model, and the quadrilateral elements are set as S4R elements. The triangular mesh elements, which are primarily distributed on the horizontal section plates, are assigned the S3 element type. The typical element size is 0.2 m, which is selected based on a mesh sensitivity study. Elements near the edges are refined according to the stress distribution. Additionally, curvature control is applied to the mesh generator to resolve the crescent shape. The maximum deviation factor is set to 0.1 so that the approximate number of elements per circle at the edges of the crescent profile is 8.

3.4.2 Simplified solid model

Two-way coupled FSI simulations are performed to address the aeroelastic effects in detail. Based on the results of the quasi-FEA results, "concept 2" (see Figure 9(d)) is selected for FSI

analysis. The wingsail sections and the mast are uniformly extruded solid bodies. The structure frame and panels are both made of aluminum.

Since the real structural design is too complex, the simulation is established based on a simplified solid model, which has the same bending stiffness, *i.e.*, Young's modulus (E) times the moment of inertia (I), as the actual wingsail structure. Each section of the wingsail and the mast is simplified independently. A quad-dominated mesh is used for FEA, as shown in Figure 16.
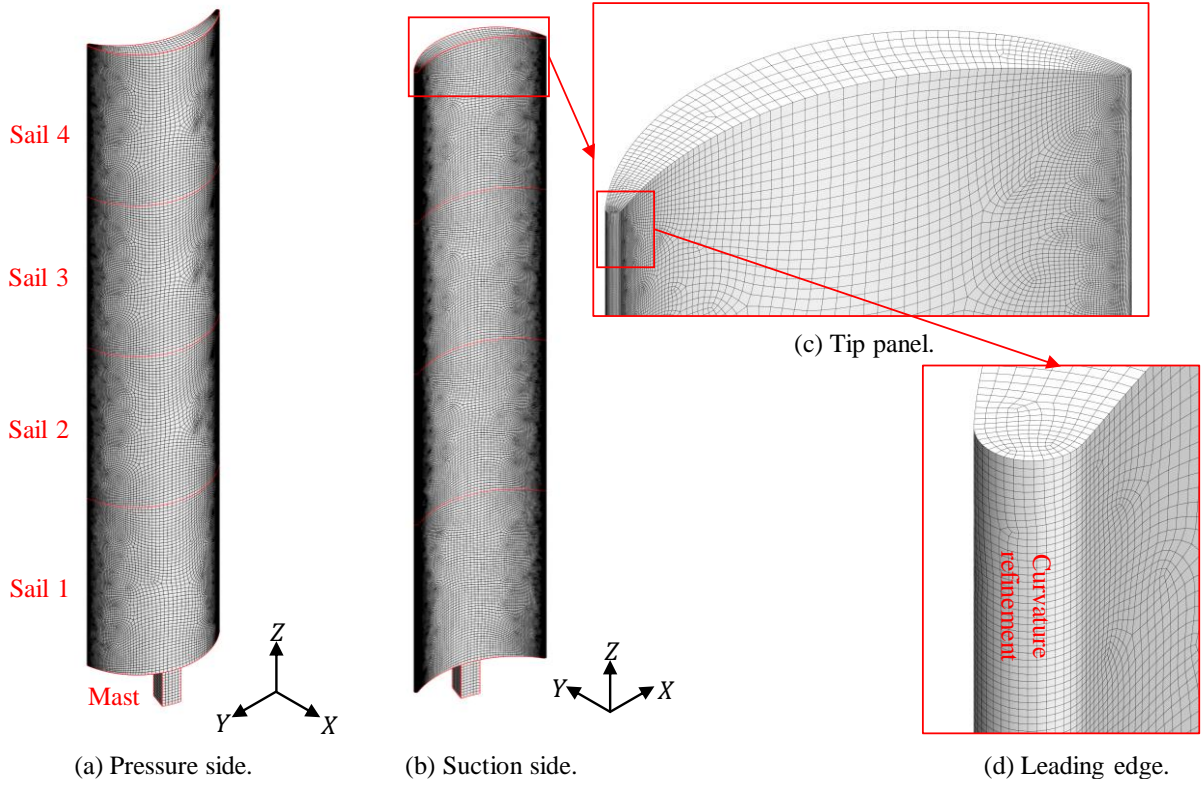

(c) Tip panel.

(a) Pressure side.   (b) Suction side.   (d) Leading edge.

Figure 16. The FEA mesh with the simplified solid mode*l*.

To understand the FSI patterns, it is important to know the structural eigenfrequencies (f_e). Based on the beam theory (Rao & Yap, 1995), the wingsail is modeled as a cantilever beam. The fundamental eigenfrequency (f_{e1}) can be calculated as Equation (3).

$$f_{e1} = \frac{\alpha_1^2}{2\pi} \sqrt{\frac{EI}{\rho A_H H^4}} \tag{3}$$

where α_1 is the first root of the characteristic equation for a cantilever beam and is set to $\alpha_1 \approx 1.875$, E is the Young's modulus, I is the moment of inertia of the cross-section about the bending axis, ρ is the averaged density of the structure, and A_H is the cross-sectional area.

As in the quasi-static FEA, the NLGEOM option is used here. Gravity is ignored (Zhu *et al.*, 2023).

3.4.3 Two-way coupled FSI

The Lagrangian and Eulerian reference frames are applied to the solid and fluid domains, respectively, and the ALE algorithm is applied to couple the two domains. The mesh in the fluid domain is allowed to move and deform without excessive distortions to accommodate the displacement of the solid-structure interface.

In the two-way coupled FSI approach, the CFD and FEA exchange data at every iteration of the simulation. The CFD utilizes the IDDES approach. The wall pressure and shear stress are transferred from the fluid domain to the solid domain, where they act as external loads on the solid surface. The structural displacement resulting from these forces is transferred back to the fluid domain. In this process, the fluid and solid interact dynamically.

During every iteration, the traction at the fluid-solid interface is calculated as the vector sum of the shear stress and the pressure component in the normal direction. The structural displacement is then calculated based on the stress distribution using Hooke's Law. Since the vertices of the CFD and FEA meshes at the fluid-solid interface are not conformable, conservative mapping of the physical variables is required. After mapping, mesh morphing is performed to accommodate the structural displacements and ensure the fluid mesh conforms to the deformed shape of the solid. Additionally, the radial basis function (RBF) method is used for mesh morphing to preserve mesh quality and avoid excessive distortion.

The complete fluid load is applied at the first time step. There is no under-relaxation for the fluid-solid interface deformation to ensure stability and convergence during the coupling process.

3.5 Power prediction program (PPP)

Strategies regarding wingsail operations under different wind conditions are suggested, and a case study is carried out to estimate the long-term fuel-saving performance.

3.5.1 Principle of sailing

The principle of sailing follows Kimball (2009). Figure 17(a) presents the wind triangle. The apparent wind is the wind experienced by the ship and sails. The apparent wind speed and angle (V_{AW} and θ_{AW})) can be calculated using Equations (4) and (5), respectively.

$$V_{AW} = \sqrt{V_S^2 + V_{TW}^2 + 2V_S V_{TW} \cdot \cos \theta_{TW}} \tag{4}$$

$$\theta_{AW} = \tan^{-1}\left(\frac{V_{TW} \cdot \sin \theta_{TW}}{V_S + V_{TW} \cdot \cos \theta_{TW}}\right) \tag{5}$$

The external loads on the sail include the force and moment, as shown in Figure 17. The lift and drag (F_L and F_D) are defined with respect to the apparent wind direction. On the other hand, the thrust and side force (F_T and F_S) are defined with respect to the ship cruising direction. The side force accounts for heeling and rolling, as well as drift and additional induced resistance. The thrust is calculated as Equation (6).

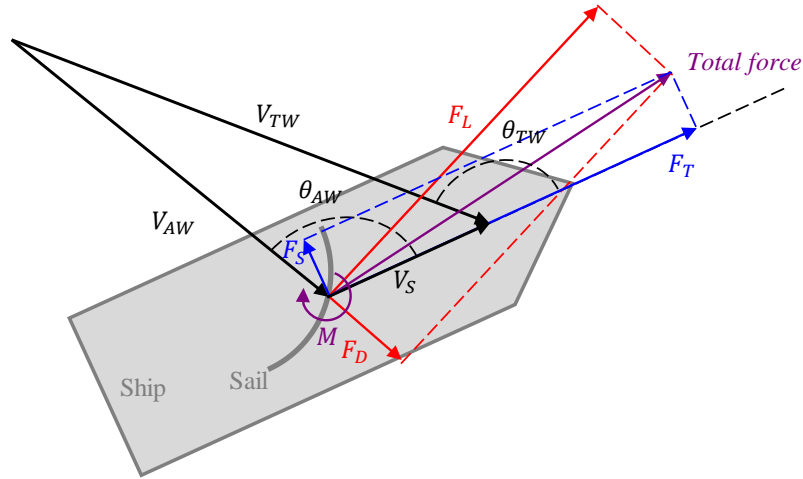$$F_T = F_L \cdot \sin \theta_{AW} - F_D \cdot \cos \theta_{AW} \tag{6}$$

Figure 17. Principle of sailing.

An enumeration method is used to predict the propulsive performance for apparent wind directions, where θ_{AW} ranges from 0° to 180° and α ranges from 0° to 90°.

3.5.2 ShipCLEAN

Predicting the performance of a WASP system requires the inclusion of the full system, *i.e.*, the wingsails and the ship. The side force F_S and yaw moments must be compensated for by the ship drift and rudder angle, both of which introduce an added resistance that reduces the net thrust. Sail trim optimization is needed to achieve the best performance. Therefore, a model considering four degrees of freedom (*i.e.*, surge, drift, yaw, and heel) must be used. In this thesis, a tanker with a deadweight of approximately 100,000 tons is considered. The crescent-shaped wingsail is positioned on the centerline and 5 m behind the forward perpendicular.

(a) Route of the case study ship during 2018. (b) Scatter plot of the experiences with θ_{TW} and V_{TW}.
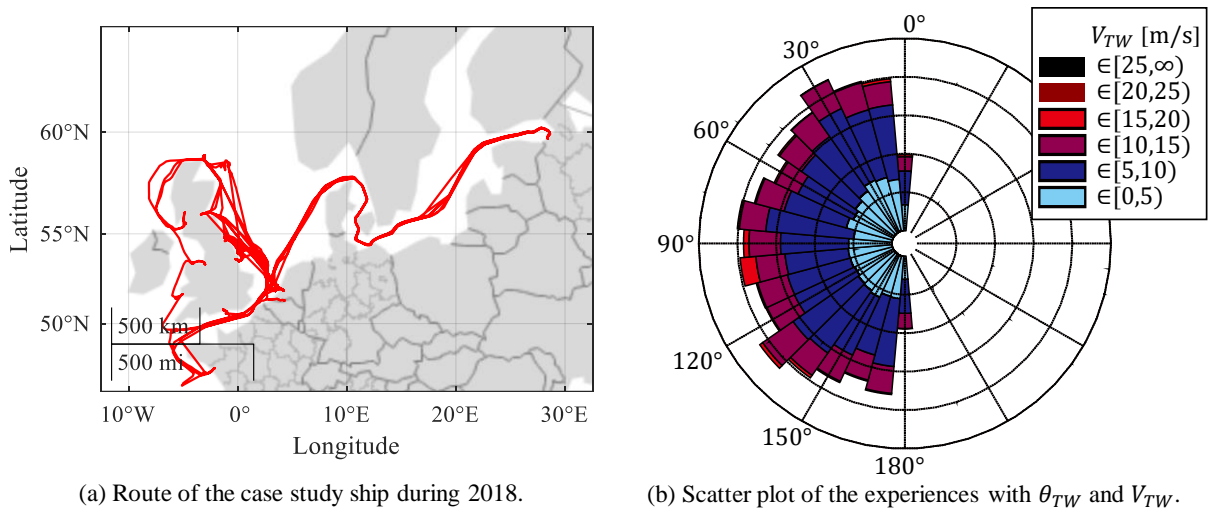
Figure 18. Shipping route and metocean data of the case study.

ShipCLEAN (Tillig *et al.*, 2019) is a generic model developed for performance predictions with little input data. Polar plots for fuel savings are first created for different wind strengths and true wind angles. Then, to calculate long-term fuel savings, the automatic identification system (AIS) data of the tanker are used to derive the ship position and speed during 2018, as shown in Figure 18(a). Environmental conditions are retrieved from the Copernicus Marine

Environment Monitoring Service (CMEMS) and are updated every 3 hours. Figure 18(b) shows the experienced wind conditions during 2018. Detailed information about the route and weather conditions for the case study can be found in **Paper I**.

4 Selected results

This Chapter presents the key results of the appended **Paper**s.

4.1 Overview of studied cases

The sectional profiles and scales of the wingsail geometries are listed in Table 1. The Reynolds numbers and AOAs are illustrated in Figure 19.

Table 1. Wingsail geometries that are studied in the **Paper**s.

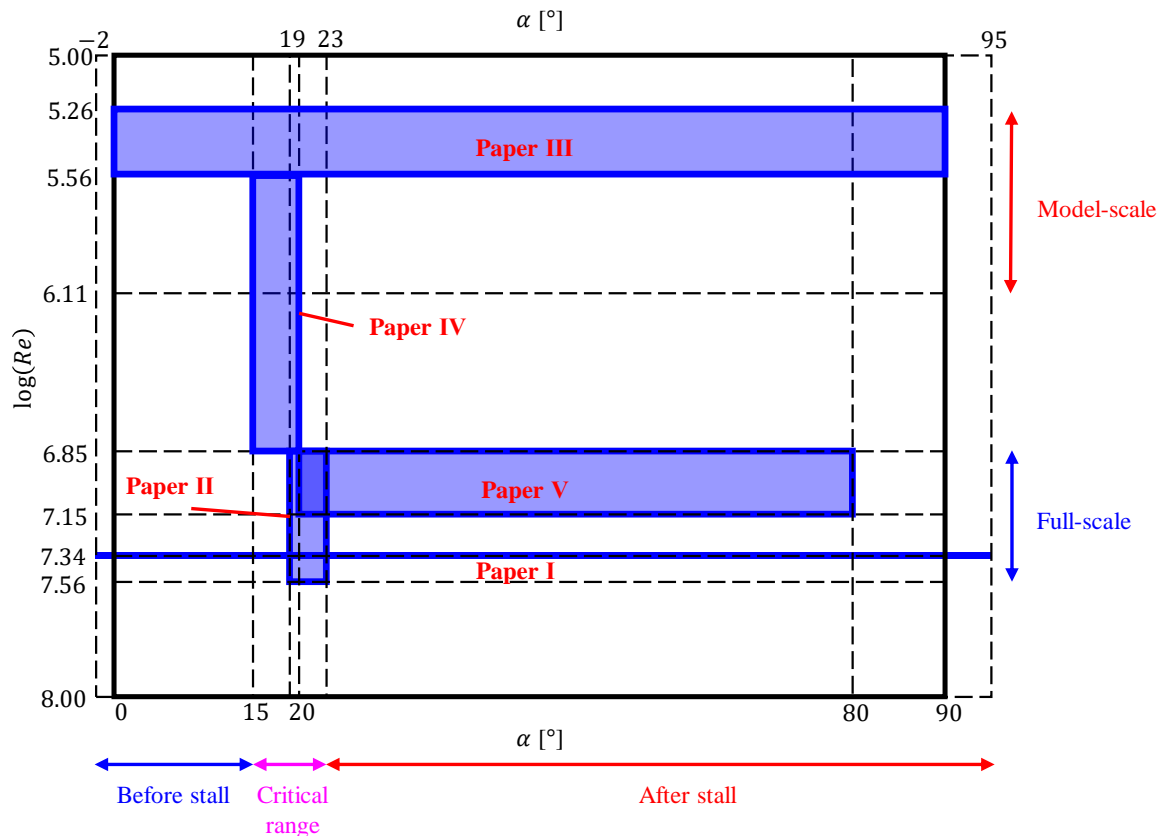|	Sectional profile	Scale	L_c	H
Paper I	NACA 0015 D2R10	Full-scale	14 m	72 m
Paper II	D2R8	Full-scale	14 m	74 m 32 m
Paper III	D2R8	1:100 model-scale	0.14 m	0.50 m 0.74 m
Paper IV	D2R8	1:100 model-scale 1:50 model-scale Full-scale	0.14 m 0.28 m 14 m	0.74 m 1.48 m 74 m
Paper V	D2R8	Full-scale	14 m	74 m

Figure 19. The Reynolds numbers and AOAs studied in the **Paper**s.

31

In **Paper I**, the Reynolds number (Re) is 2.3×10^7. According to the wind tunnel tests (Sheldahl & Klimas, 1981), when $Re = 1 \times 10^7$, the critical angle of attack (α_c) of NACA 0015 is approximately 16°. A previous study (Nikmanesh, 2021) indicated that α_c of the present crescent-shaped profile is approximately 20°. Therefore, NACA 0015 is simulated at $\alpha = 16°$, and the crescent-shaped profile at $\alpha = 20°$.

In **Paper II**, given that the wingsail with a telescopic function can be fully expanded or retracted at different wind speeds, $Re = 7.1 \times 10^6$ is used for the expanded condition, and is set at 2.9×10^7 for the retracted case. The AOAs are $\alpha = 19°, 21°, 23°$.

In **Paper III**, Re values ranging from 1.8×10^5 to 3.6×10^5 are investigated using simulations and WT tests. The AOA ranges from 0° to 90°. Specifically, at an AOA of 20°, the triple-sail system is investigated at yaw angles (β) ranging from 80° to 120°.

In **Paper IV**, the AOAs are 15° and 20°. Re ranges from 3.6×10^5 to 1.3×10^6 for model-scale cases; a full-scale wingsail with $Re = 7.1 \times 10^6$ is also analyzed for comparison.

In **Paper V**, $Re = 1.4 \times 10^7$ is applied for the external loads in quasi-static FEA, while $Re = 7.1 \times 10^6$ is used for two-way coupled aeroelastic simulations. The AOAs are 20°, 40°, and 80°.

4.2 Results of Paper I

Paper I aims to investigate the time-averaged characteristics of the crescent-shaped wingsail aerodynamics and the long-term energy performance of ships applying this wingsail. Full-scale CFD simulation models based on unsteady Reynolds-averaged Navier-Stokes (URANS) equations are developed and verified for the prediction of aerodynamic loads. Based on the time-averaged aerodynamic loads, *i.e.*, force coefficients, predicted by CFD simulations, a long-term case study is carried out using the in-house PPP platform, ShipCLEAN. The wingsail with a crescent-shaped profile is compared with that based on NACA 0015, and the results indicate that the former has notably better propulsive performance. However, stronger flow separation is detected for the crescent-shaped wingsail. The case study highlights that installing a wingsail with a crescent-shaped profile can reduce fuel consumption by 9% compared with no wingsail.

4.2.1 Time-averaged aerodynamic loads

4.2.1.1 Crescent-shaped profile *vs.* NACA 0015

Although various simulation setups are adopted (see Figure 20), a general finding is that the crescent-shaped profile of D2R10 produces much greater lift and drag than NACA 0015. Since both lift and drag contribute to the thrust, the results indicate the good aerodynamic performance of the crescent-shaped wingsail.

The three-dimensional simulations using "symmetry bottom and freestream tip" BC show the development of vortices at the wingsail top tip, whereas simulations with the other domain type do not. Therefore, the effects of tip vortices can be discerned by comparing the results of these two types of simulations. Additionally, the tip effects of the crescent-shaped profile are less significant than those of the NACA 0015 profile.
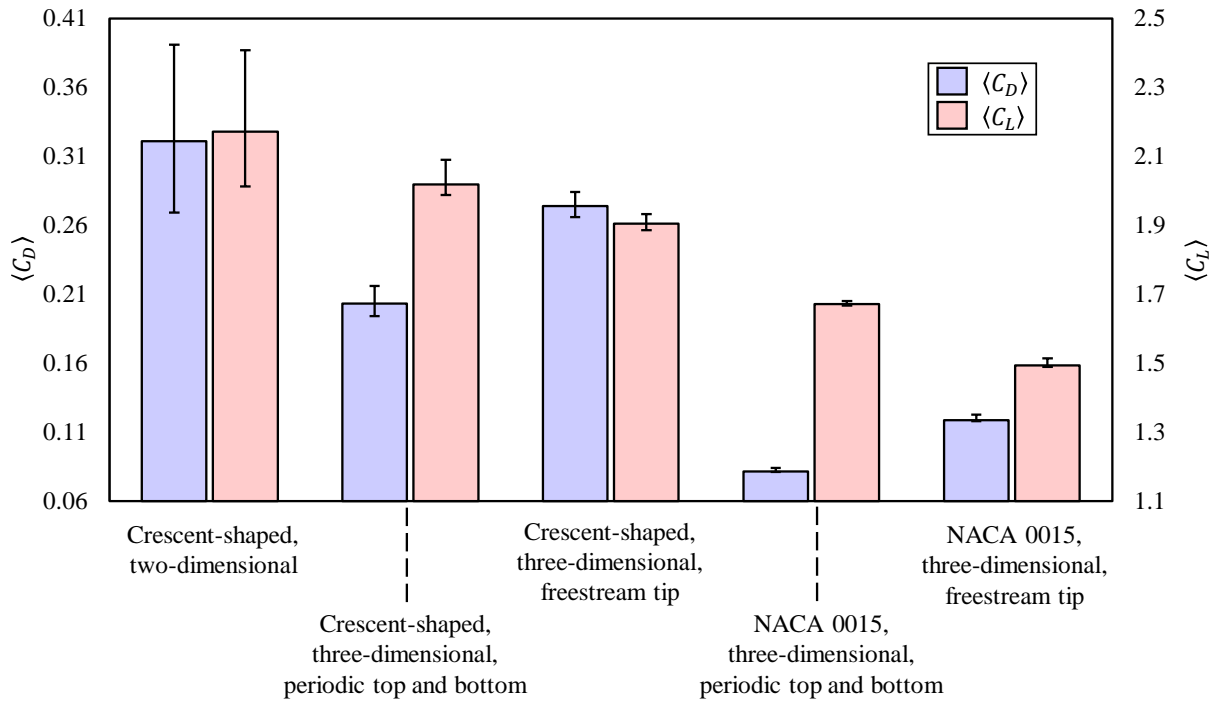
Figure 20. The force coefficients of NACA 0015 and the crescent-shaped "D2R10" profile from the two- and three-dimensional simulations with different computational domain types. The error bars represent the amplitudes of oscillation.

4.2.1.2 Force coefficient curves

Plots of the force coefficients within a wider range of α based on the three-dimensional CFD simulations are presented in Figure 21. There is no clear α_c, and two peaks of $\langle C_L \rangle$ occur. The highest $\langle C_L \rangle$ is approximately 1.915 at $\alpha = 20°$, which is the critical angle of attack (α_c). Another $\langle C_L \rangle$ peak occurs after stall at $\alpha = 35°$. $\langle C_D \rangle$ increases as α increases, and the highest $\langle C_D \rangle$ is approximately 1.595 at $\alpha = 85°$.
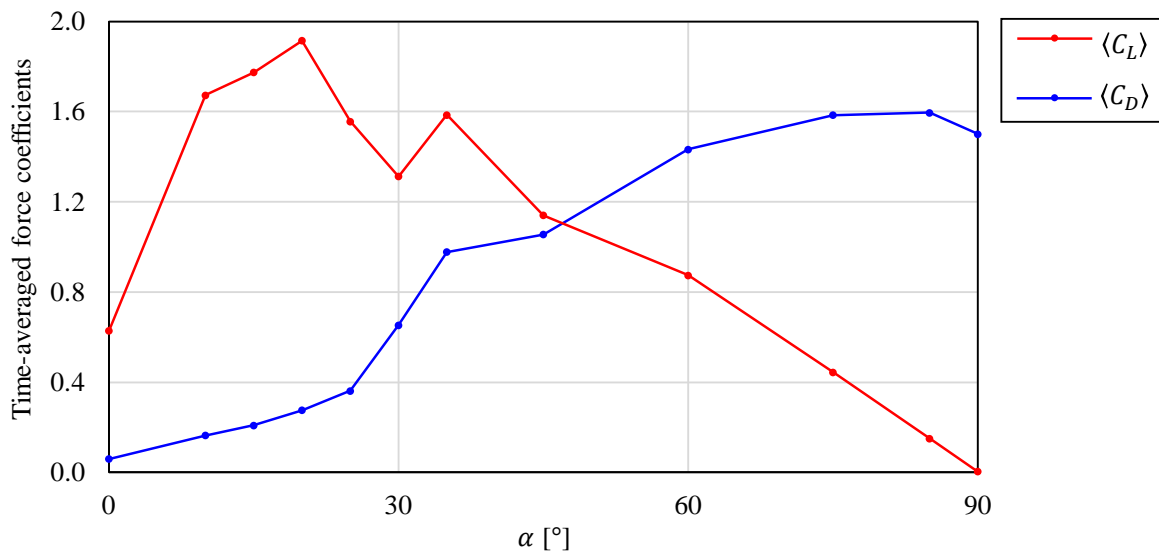

Figure 21. $\langle C_L \rangle$ and $\langle C_D \rangle$ *vs.* α for full-scale full-expanded wingsail with the "D2R10" profile based on three-dimensional URANS simulations.

4.2.2 Propulsive performance

4.2.2.1 Operation strategy

The propulsive performance is evaluated based on the force coefficients from the three-dimensional simulations with the freestream tip computational domain type. The results for the propulsion (the highest C_T at different θ_{AW}) and the corresponding operational AOA (α values applied to obtain the highest C_T) are plotted in Figure 22. Since the polar diagram is symmetric, only half of the polar plot, *i.e.*, $0° \leq \theta_{AW} \leq 180°$, is presented.

When the point of sail is luffing, close-hauled, or beam reach (θ_{AW} from 30° to around 120°), the lift is the main source of the thrust. When $120° < \theta_{AW} < 150°$, *i.e.*, the point of sail is board reach, the optimum α is approximately 40° where $C_L \approx C_D$, and the wingsail utilizes both F_D and F_L for propulsion. When the point of sail is running, meaning that θ_{AW} is approximately 180°, F_D is the primary contributor to thrust, and the wingsail is operated with $\alpha \approx 80°$.

(a) C_T vs. θ_{AW}.   (b) α vs. θ_{AW}.   (c) C_L/C_D vs. θ_{AW}.
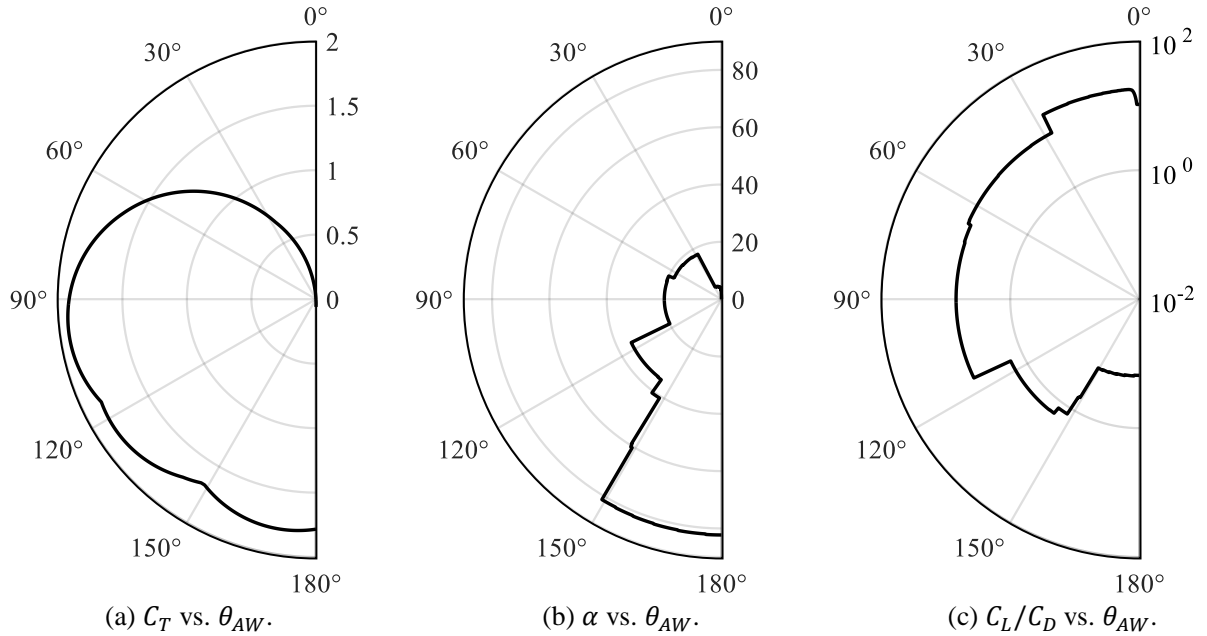
Figure 22. Polar diagram of C_T, α, and L/D versus θ_{AW} for the crescent-shaped profile at $V_{AW} = 25$ m/s.

4.2.2.2 Long-term fuel-saving performance

The polar diagram is applied to the in-house program, ShipCLEAN (Tillig *et al.*, 2019) for a tanker, as mentioned in Section 3.5.2. The fuel consumption analysis shows that the maximum fuel savings is expected to be approximately 9% at $\theta_{TW} = 90°$ in $V_{TW} = 10$ kn, and 25% in $\theta_{TW} = 90°$ in $V_{TW} = 20$ kn. However, the fuel savings vary depending on the true wind angle, so the performance must be predicted using actual routes with realistic weather.

As shown in Figure 23, a single crescent-shaped wingsail achieves fuel savings higher than 5% approximately 34% of the time, and the maximum fuel savings is 97.5%. It is deduced that the total long-term fuel savings is 9.5%. Note that the maximum additional fuel consumption for operating the wingsail is less than 1%.
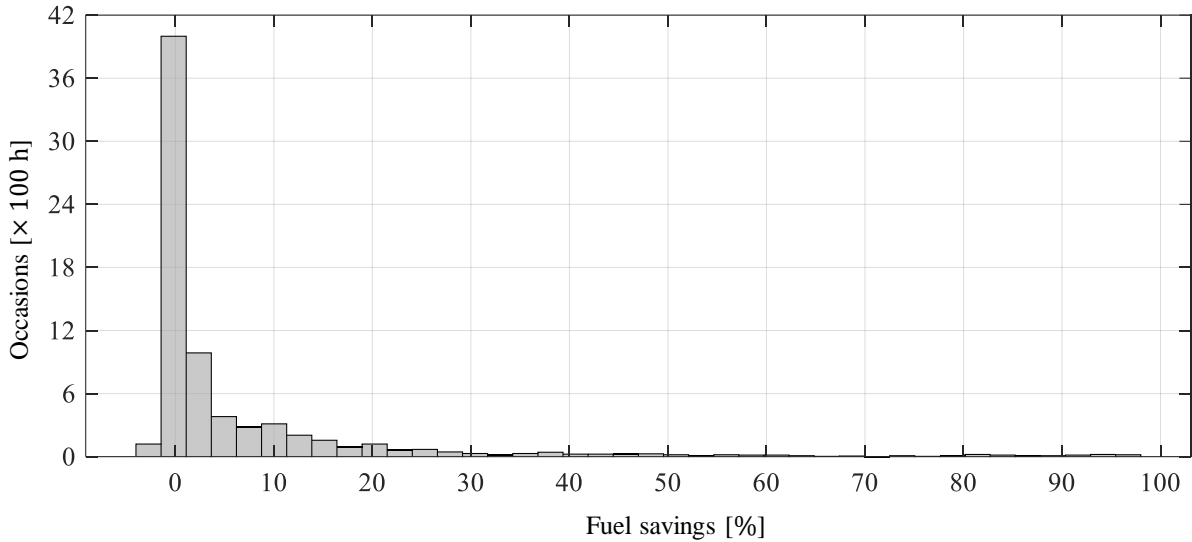
Figure 23. Histogram of the fuel savings achieved by a crescent-shaped wingsail at each waypoint.

4.3 Results of Paper II

Building on previous work, **Paper II** aims to reveal the unsteady characteristics of the aerodynamic loads on the crescent-shaped wingsail and its induced flow field. Parametric sensitivity studies are conducted to optimize the crescent-shaped profile. Based on the CFD models developed in **Paper I**, full-scale CFD simulations, with both URANS and improved delayed detached eddy simulation (IDDES) approaches, are performed. The spectral features of the aerodynamic loads are analyzed, and the unsteady flow field characteristics, including flow separation, vortex shedding, wake properties, and tip vortices are discussed in detail. The results highlight that while URANS and IDDES simulations provide similar predictions for time-averaged loads, their unsteady characteristics differ, particularly their high-frequency features. The IDDES simulations reveal more complex vortex-shedding phenomena.

4.3.1 Unsteady aerodynamic loads

The force coefficients of the fully expanded crescent wingsail are plotted in Figure 24. URANS and IDDES provide similar results for the time-averaged force coefficients. The difference between these two methods is usually less than 10% for C_L and C_D, and 15% for C_M. This suggests the viability of URANS for predicting time-averaged forces.

However, the URANS results exhibit larger fluctuation amplitudes than the IDDES results. This can be attributed to more turbulent content contained in the flow field obtained from the IDDES. This turbulence reduces large-scale fluctuations.

The comparison of the two methods suggests that the IDDES method is a better choice if the intention is to accurately capture the FSI between the wingsail structure and winds because of the capability of this method to resolve turbulent fluctuations. This will be further explained based on the flow field characteristics in the next section.

4.3.2 Flow characteristics – wake and tip vortices

The URANS and IDDES methods exhibit several differences in the wake induced by the crescent-shaped wingsail. The dimensionless vorticity in the spanwise direction, ω_Z^*, is shown at different streamwise positions in Figure 25. The IDDES predicts a flow field with much more

complex vortex structures. In contrast, the wake from the URANS does not show significant spanwise characteristics.

(a) C_L.   (b) C_D.   (c) C_M.
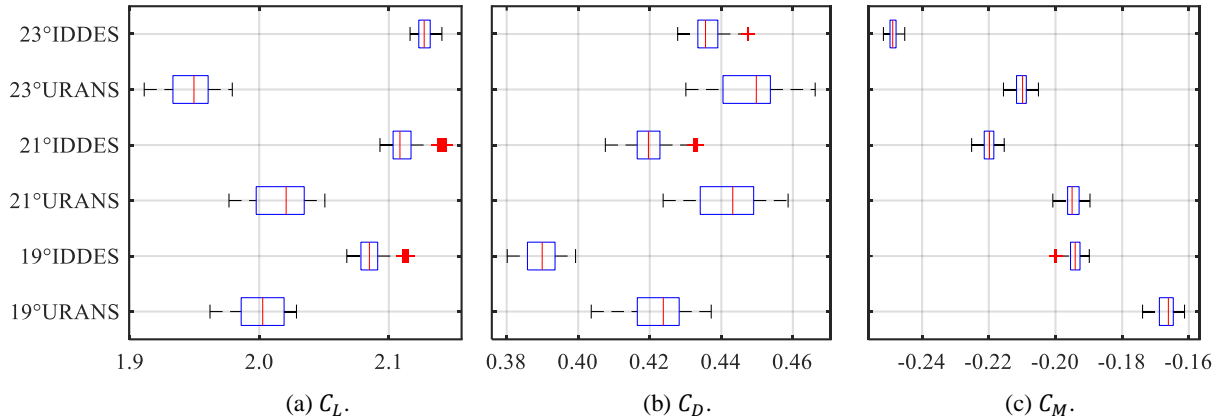
Figure 24. Boxplots of time-averaged force coefficients of the full-expanded crescent wingsail.
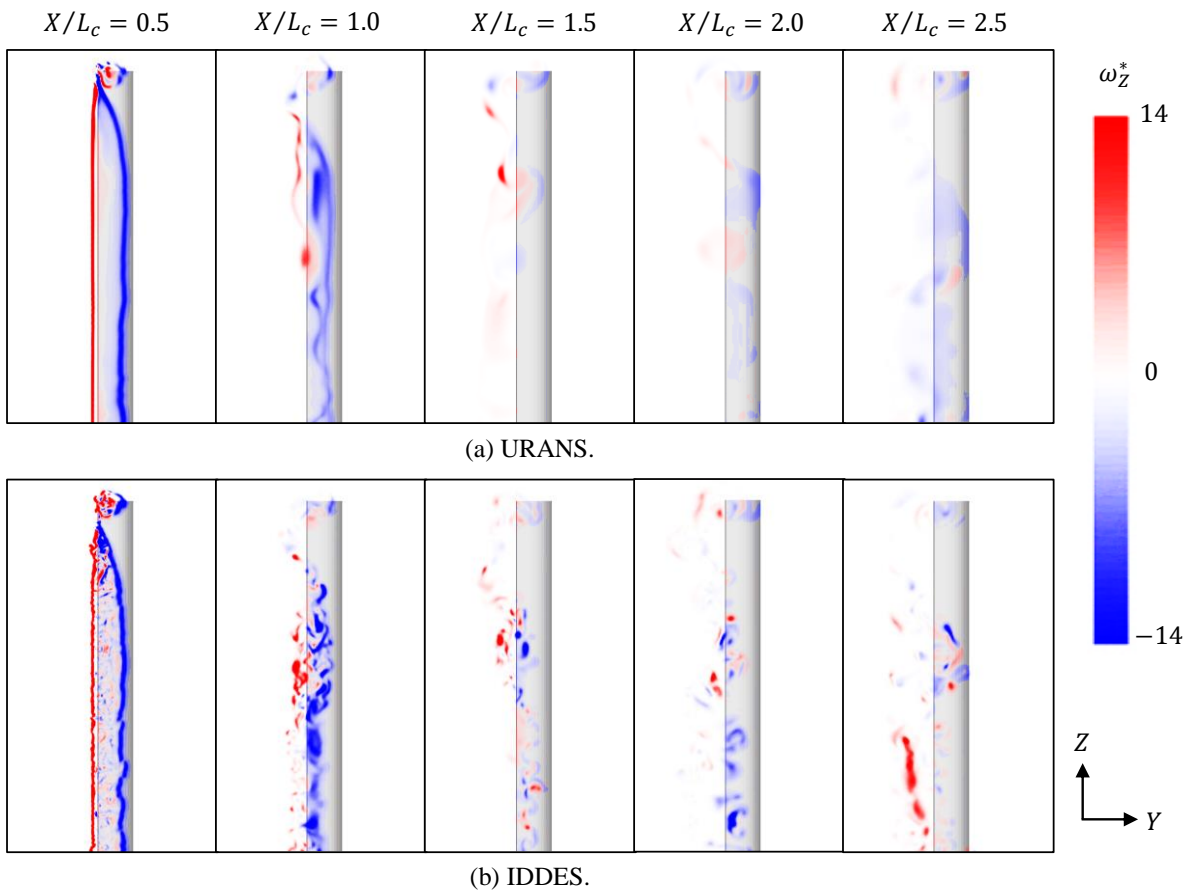
(a) URANS.

(b) IDDES.

Figure 25. Distribution of the dimensionless spanwise vorticity, ω_Z^*, at different streamwise positions in the wake from the full-expanded wingsail at $Re = 7.1 \times 10^6$, $\alpha = 23°$, computed using URANS and IDDES.

Another important characteristic of the flow field is the phenomenon of tip vortices, which is believed to be the primary reason for lift reduction when changing the boundary conditions from periodic top and bottom to free tip and symmetric bottom. The dimensionless streamwise vorticity, ω_X^*, around the tip is shown in Figure 26. Two tip vortices, the tip separation vortex

and the tip leakage vortex, develop at the suction and pressure sides, respectively. The vortices from the IDDES are more complex than those from the URANS.

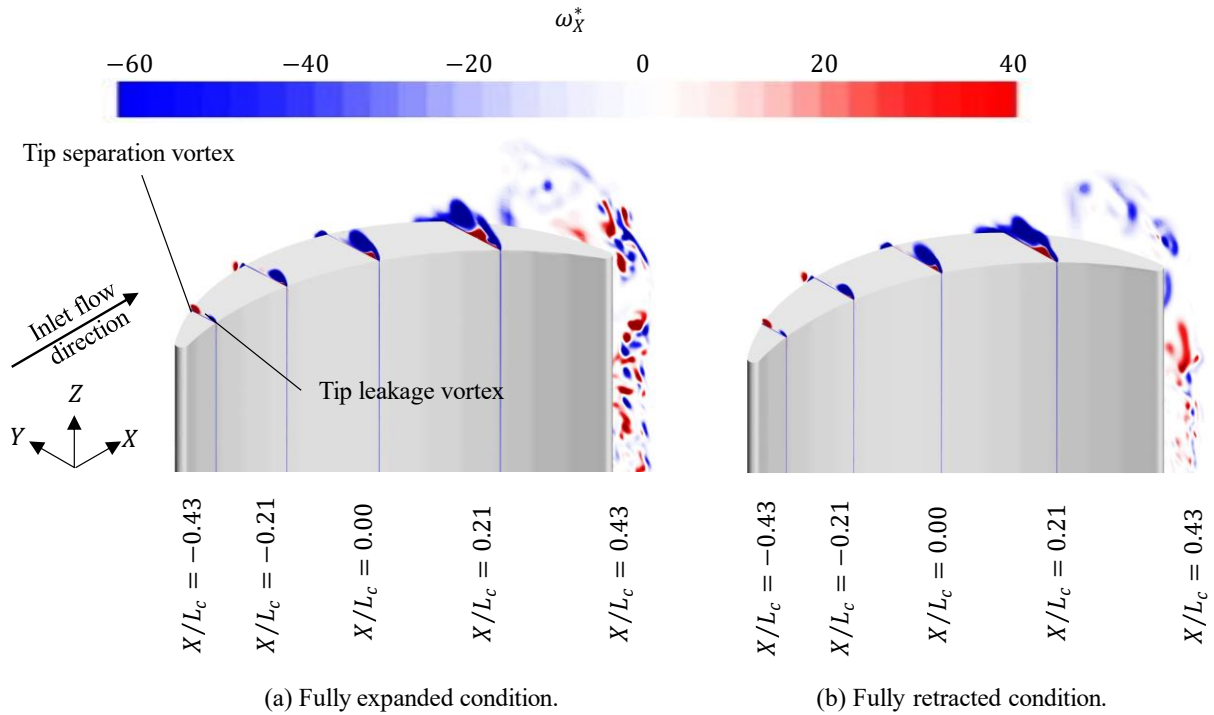(a) Fully expanded condition.   (b) Fully retracted condition.

Figure 26. The distribution of the dimensionless streamwise vorticity ω_X^* at different streamwise positions around the tip, based on the IDDES simulations at $\alpha = 23°$.

4.4 Results of Paper III

Paper III aims to use experimental methods to study the aerodynamics of a crescent-shaped wingsail across a range of moderate Re values in single- and triple-wingsail configurations. WT tests are conducted for wingsails with two aspect ratios (5.3 and 3.6, corresponding to semi-retracted and full-expanded sails in practice) at AOA from 0° to 90°, and Re values ranging from 1.8×10^5 to 3.6×10^5. Following the methods applied in **Paper II**, a CFD simulation based on IDDES is also performed for the triple-wingsail system. The results indicate that in addition to general aerodynamic characteristics, a specific crisis of the aerodynamic forces is found at an AOA of 15° when Re is reduced to 2.7×10^5, which does not exist in conventional NACA-profile wingsails. When triple wingsails are arranged in a row, the pressure field between them interferes, although the vortex patterns in the wakes are similar. This interference leads to significant redistribution of the aerodynamic forces among the wingsails. The total thrust from the triple wingsail arrangement is approximately three times the thrust of a single wingsail.

4.4.1 Single wingsail aerodynamics

The first experimental validation of the crescent-shaped wingsail is reported in this work. The comparison of the numerical and experimental results has been shown in Figure 15 in Section 3.3.5. The pressure distribution is measured to allow for interpretation of the force measurements and enable deeper insight into the aerodynamic loads. The measurement is made at the midspan, $Z = 0.5H$, and the distribution of C_p is plotted in Figure 27.
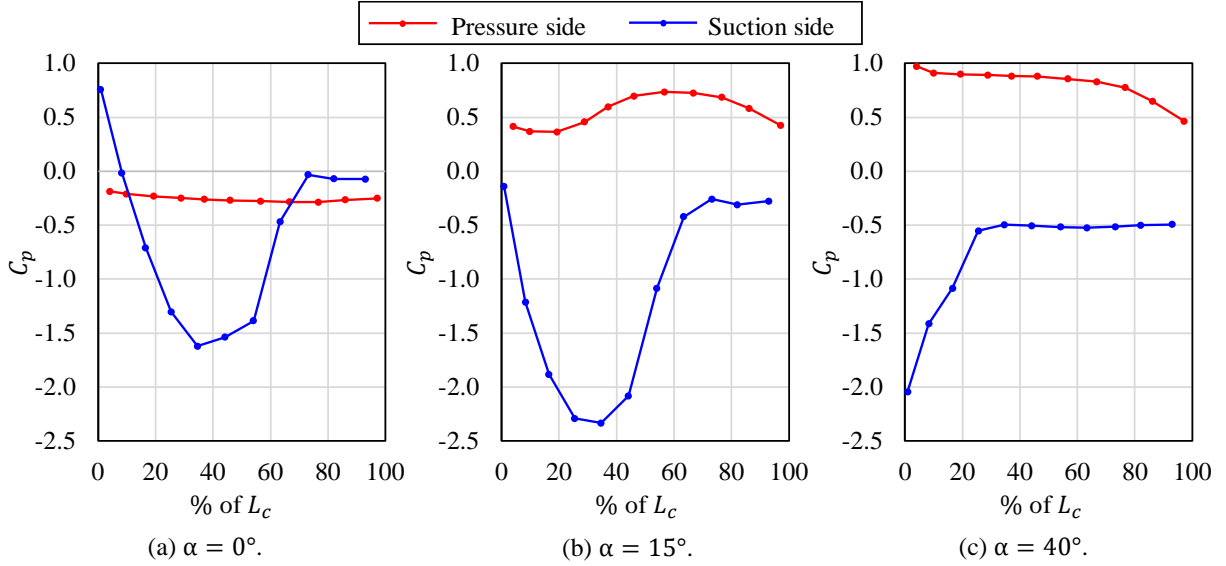
Figure 27. Surface pressure distribution of the wingsail model at $Re = 3.6 \times 10^5$, measured at $Z = 0.5H$.

As shown in Figure 27(a), at an AOA of $\alpha = 0°$, the pressure on both the pressure and suction sides of the wingsail exhibits an inverted sign at both the leading and trailing edges. Additionally, the pressure is negative on the pressure side because of the flow separation induced by the leading edge at small α. The pressure difference between the two sides of the wingsail is smaller at $\alpha = 0°$ than that at $\alpha = 15°$ or $40°$, leading to low C_L at $\alpha = 0°$. At $\alpha = 15°$, where the highest C_L is achieved during the WT tests, the pressure on the upstream half of the suction side is very low, as shown in Figure 27(b), causing a strong suction force. According to the numerical simulation results presented in **Paper I** and **Paper II**, the high-velocity flow on the suction side is the primary cause. The location of stall, as indicated by pressure measurements, is identified by a plateau with constant pressure, as the pressure inside a separation bubble is constant. In Figure 27(a) and (b), constant pressure is achieved at 70%. However, in Figure 27(c), it is found that at $\alpha = 40°$, where C_L is close to C_D, stall occurs at 25% chord. Low pressure occurs on the suction side close to the leading edge, which contributes to F_L and produces a moment on the wingsail. When the AOA is between $0°$ and $15°$, the stall location is fixed at 70% chord. Between $15°$ and $40°$, the stall location gradually moves upstream from 70% chord to 25% chord. The variation in lift performance (see Figure 15) is explained by the changes in stall location, as confirmed by the pressure measurements. This current measurement provides the first validation of the pressure distribution for a crescent airfoil.

4.4.2 Triple-wingsail interaction

The aerodynamic force coefficients, *i.e.*, C_L and C_D, measured for the three-line-up wingsails, at different values of β and a $Re = 3.6 \times 10^5$ are shown in Figure 28, where $\alpha = 20°$ for all wingsails. The triple-sail system is seen in Figure 9(c). Sail 3, *i.e.*, the downstream (stern) wingsail, generates the least lift of the three wingsails for $\beta \in [80°, 120°]$, whereas Sail 1 (bow) generates the most lift. In the case of the drag measurements, Sail 2 (middle) generates the largest F_D when $\beta \leq 90°$, but Sail 1 generates the largest F_D when $\beta \geq 100°$. Sail 3 always generates the smallest F_D. The differences in force coefficients among the three wingsails

38

indicate that the flow interaction between the wingsails affects the distribution of the aerodynamic loads.

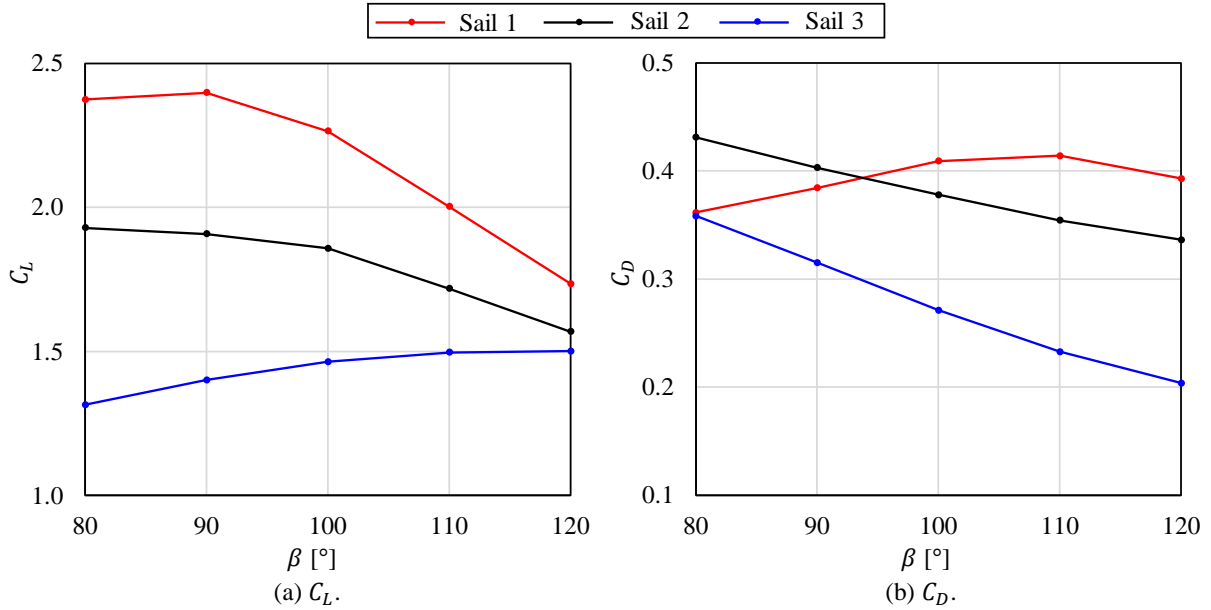Figure 28. Force coefficients of the triple-sail system at different apparent wind angles of β, but $Re = 3.6 \times 10^5$ and $\alpha = 20°$.

4.5 Results of Paper IV

On the basis of **Paper III**, **Paper IV** aims to determine whether laboratory model-scale experiments (moderate $Re{\sim}10^5$) remain valid for evaluations of real sail performance (high $Re{\sim}10^7$). Following the methods applied in **Paper II**, a series of CFD simulations based on IDDES are performed. The findings reveal that increasing Re not only improves the lift-to-drag ratio but also increases the critical angle of attack, indicating that model-scale tests can underestimate these parameters compared to those in full-scale practice. A critical Re range is identified. Detailed analysis shows that changes in laminar-turbulent transition and, more significantly, flow separation and reattachment patterns are crucial to understanding the physical mechanisms of the force crisis.

4.5.1 Reynolds number sensitivity of aerodynamic loads

Figure 29 presents the time-averaged force and moment coefficients (denoted as $\langle C_L \rangle$, $\langle C_D \rangle$, and $\langle C_M \rangle$, respectively) at $\alpha = 15°$ and $20°$. The length of the realizations used for the time-averaging operation is 100 periods, for which one period is the time of the flow passing through the chord. All coefficients are dependent on Re. The $\langle C_L \rangle$ increases with Re, particularly when $\alpha = 20°$. This suggests that the aerodynamic efficiency at very high Re in the real world is underestimated in WT tests which can only achieve moderate Re. At $Re = 6.2 \times 10^5$ and 1.3×10^6, the model-scale case shows larger $\langle C_L \rangle$ at $\alpha = 15°$ than $\alpha = 20°$, while the full-scale case exhibits an opposite trend. This phenomenon indicates that the critical angle of attack (α_c), is also affected by Re. It is observed that for Re values ranging from 6.2×10^5 to 7.1×10^6, α_c increases with Re. The sharp decrease in $\langle C_L \rangle$ (*i.e.*, the lift crisis) happens when

the Re value decreases from 6.2×10^5 to 3.6×10^5 for $\alpha = 15°$, and from 7.1×10^6 to 1.3×10^6 for $\alpha = 20°$.

In Figure 29(b), although $\langle C_D \rangle$ of the case with higher Re is lower than that with a lower Re, it is not as sensitive to Re as $\langle C_L \rangle$. Additionally, $\langle C_M \rangle$ also increases with Re, especially when $\alpha = 15°$. For instance, when Re increases from 3.6×10^5 to 6.2×10^5, the absolute value of $\langle C_M \rangle$ at $\alpha = 15°$ increases by 171.0%. This reflects that the position of the aerodynamic center is also affected by Re.

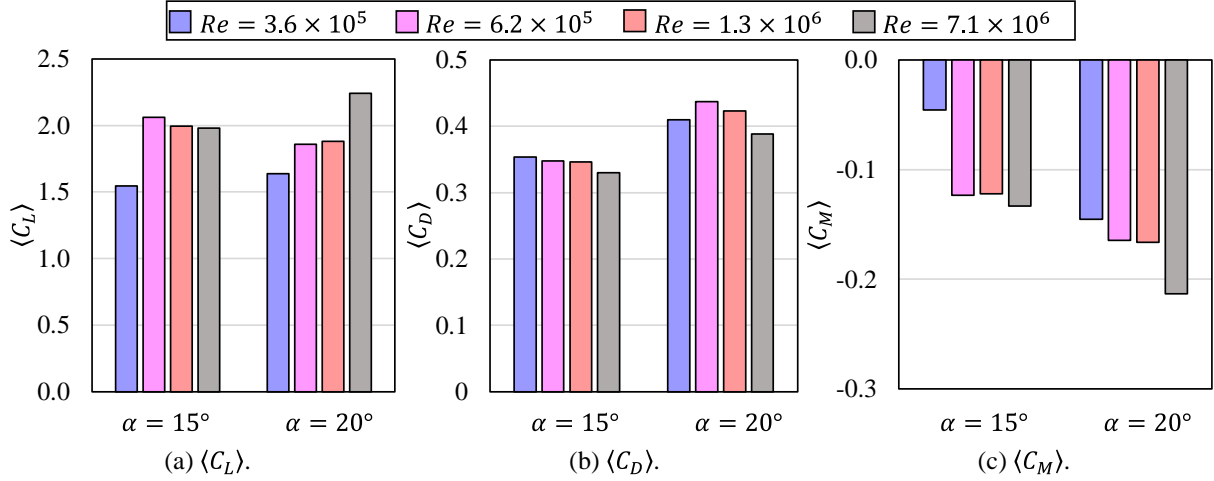Figure 29. Time-averaged force and moment coefficients with $\alpha = 15°$ and 20°, and various values of Re.

4.5.2 Laminar-turbulent transition

The laminar-turbulent transition is influenced by the Reynolds number, which scales differently between model- and full-scale conditions, leading to discrepancies in flow features. Figure 30 shows the contours of the nondimensional turbulent kinetic energy (TKE), k_t/V_∞^2, in the mid-span plane at $\alpha = 15°$ and 20°. As Re increases, the transition location shifts upstream. At the lowest Re of 3.6×10^5, the transition occurs at the mid chord, as shown in Figure 30(a) and (b). When increasing Re, the laminar-turbulent transition location moves in the upstream direction. The cases with the highest Re of 3.6×10^5 have the transition location near the leading edge, as shown in Figure 30(g) and (h), meaning that the boundary layer is turbulent along the entire suction side.

The transition location also depends on α, highlighting the impact of α on the critical Re. An abrupt shift in the laminar-turbulent transition location occurs between $Re = 6.2 \times 10^5$ and $Re = 7.1 \times 10^6$ for $\alpha = 15°$, as shown if Figure 30(c), (e), and (g). For $\alpha = 20°$, this shift occurs between $Re = 6.2 \times 10^5$ and $Re = 1.3 \times 10^6$, as shown in Figure 30(d) and (f), indicating that the transition at the larger α of 20° begins earlier than at the smaller α of 15°.

(a) $Re = 3.6 \times 10^5$, $\alpha = 15°$.

(b) $Re = 3.6 \times 10^5$, $\alpha = 20°$.

(c) $Re = 6.2 \times 10^5$, $\alpha = 15°$.

(d) $Re = 6.2 \times 10^5$, $\alpha = 20°$.

(e) $Re = 1.3 \times 10^6$, $\alpha = 15°$.

(f) $Re = 1.3 \times 10^6$, $\alpha = 20°$.

(g) $Re = 7.1 \times 10^6$, $\alpha = 15°$.

(h) $Re = 7.1 \times 10^6$, $\alpha = 20°$.
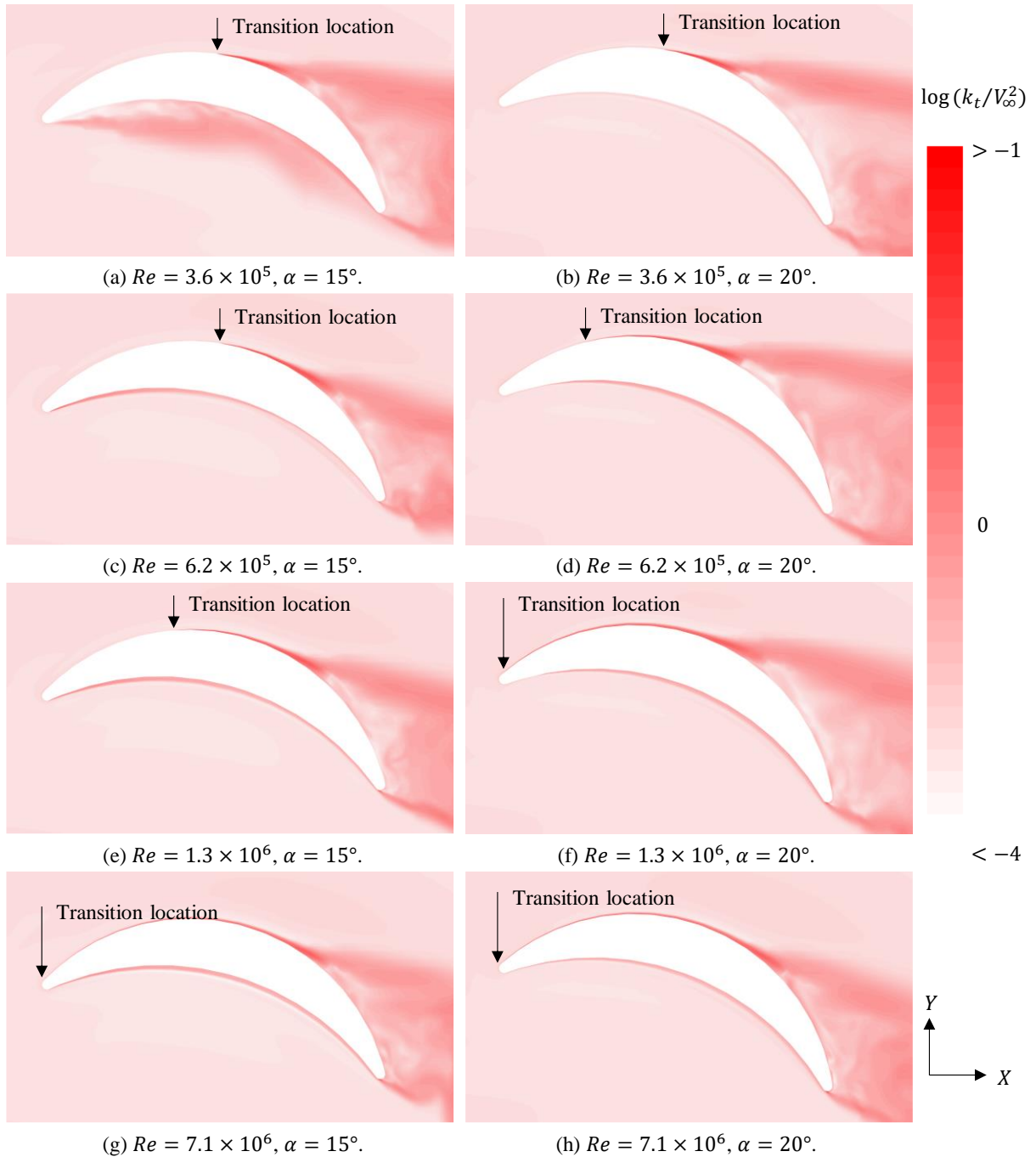
Figure 30. Distribution of nondimensional turbulent kinetic energy near the wingsail at the mid-span of the sectional panel ($Z = 0.5H$), for $\alpha = 15°$ and $20°$, with various values of Re.

4.5.3 Flow separation and reattachment patterns

Figure 31 shows the contours of the transient streamwise wall friction coefficient, $C_{\tau X}$, on the suction side of the wingsail at $\alpha = 15°$. For Re below 6.2×10^5, three flow separation points exist on the suction side at the lowest Re value. Recalling the transition location in Figure 30, it can be observed that the first and second separation points are located in the laminar region, while the third is in the turbulent region.

On the other hand, only one separation point is observed in the turbulent region for higher values of Re, $e.g.$, Figure 31(d). At the highest $Re = 7.1 \times 10^6$, the distribution of $C_{\tau X}$

41

becomes relatively even, and the flow separation position is at downstream of the laminar-turbulent transition location, within the region of the turbulent boundary layer. Despite adverse pressure gradients, the flow separation is delayed by the turbulence. As shown in Section 4.5.3, the location of the laminar-turbulent transition varies significantly between cases. This variation results in substantial changes in flow separation patterns. These changes, in turn, affect the aerodynamic forces presented in Figure 29. The delayed flow separation results in a larger C_L.
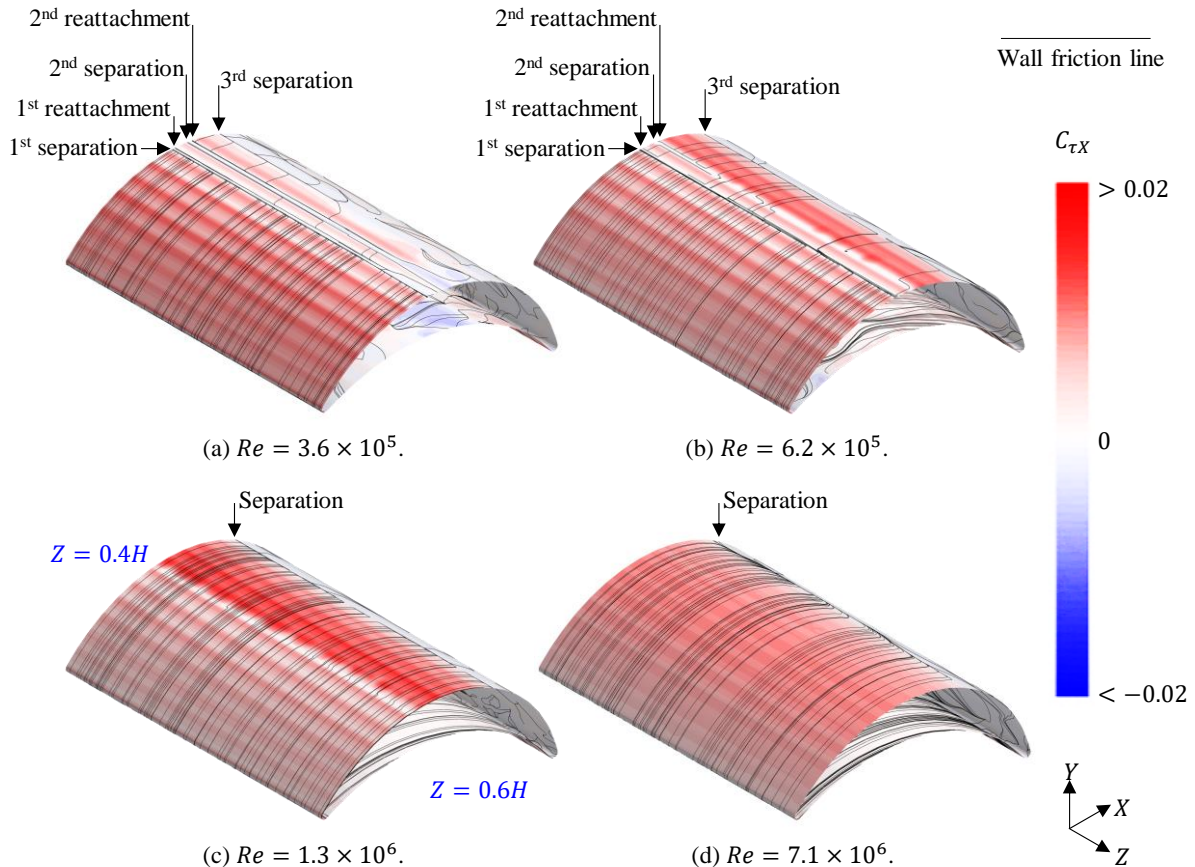
Figure 31. Distribution of $C_{\tau X}$ and the wall friction lines on the suction side of the wingsail within $Z = 0.4H$–$0.6H$ and $\alpha = 15°$.

Additional discussions regarding flow separation and reattachment patterns at $\alpha = 20°$ are presented in **Paper IV**.

4.6 Results of Paper V

Paper V explores the aeroelastic behavior of the crescent-shaped wingsail and quantifies its influence on propulsive performance. Several structural design concepts are proposed and analyzed by performing quasi-static FEA, with comparisons made based on weight, strength, and rigidity. The selected structural design concept is then simplified into a solid model for full-scale aeroelastic simulation. The results indicate that the eigenfrequencies of the wingsails dominate the frequency domain of the wingsail flutter, while the frequencies of the flow field play a secondary role. Aeroelastic effects are found to negatively impact aerodynamic performance.

4.6.1 Structural design and evaluation

A series of FEA simulations are performed to determine the thickness of various parts of the structure. The thicknesses of each of the parts are then adjusted for several iterations to satisfy the strength requirement regarding the plastic deformation and minimize their weights.

A comparison of the two concepts shows that the total weight can be reduced by approximately 11% by dividing the wingsail structure into a strong frame and light panels, as indicated by Table 2. The weight for the "all-aluminum" for "concept 1" can be significantly reduced, but this results in a much larger tip displacement. Therefore, the "steel frame and aluminum panels" design exhibits better rigidity, while the "all in aluminum" design is lighter.

Table 2. Weight, maximum von Mises stress, and maximum deflection of different structural designs.

		"Concept 1"	"Concept 2"	
			"Steel frame, aluminum panels"	"All in aluminum"
Total weight	[t]	130	116	74
Weight excluding the panels	[t]		75	33
Max. von Mises stress	[MPa]	158	141	103
Max. deflection	[m]	0.32	0.59	1.14

Figure 32 shows the von Mises stress distributions for the two material arrangements. When the wingsail has a steel frame, as shown in Figure 32(a), the stress distributed throughout the panels is much lower than in the frame, indicating that the frame bears the majority of the global bending load. In contrast, the stress in the panels is higher for the "all in aluminum" concept shown in Figure 32(b), although the distribution of von Mises stress throughout the frame exhibits similar characteristics. The maximum von Mises stress is located at the contact area of the mast and the bottom plate. Notably, the maximum von Mises stress occurs at the contact area of the mast and the bottom for both material arrangements.

4.6.2 Full-scale FSI simulations

The cases based on rigid and deformable solid bodies where $\alpha = 20°$ are selected as examples. Results and discussions for $\alpha = 40°$ and $90°$ can be found in **Paper V**.

4.6.2.1 Structural responses

The frequency characteristics based on fast Fourier transform (FFT) of the tip displacements are plotted in Figure 33. The sampled time is 21 s, *i.e.*, 12 times L_c/V_{AW}. The dominant oscillation frequency of 0.58 Hz can be observed, which is close to the fundamental eigenfrequency of the structure (0.62 Hz). In contrast, the simulations based on rigid bodies indicate that the dominant oscillation frequency of C_L is approximately 0.4 Hz. Therefore, the flutter frequency of the wingsail is more dependent on the eigenfrequency of the structure, rather than the Strouhal number (St).

(a) "Steel frame, aluminum panels."

(b) "All in aluminum."
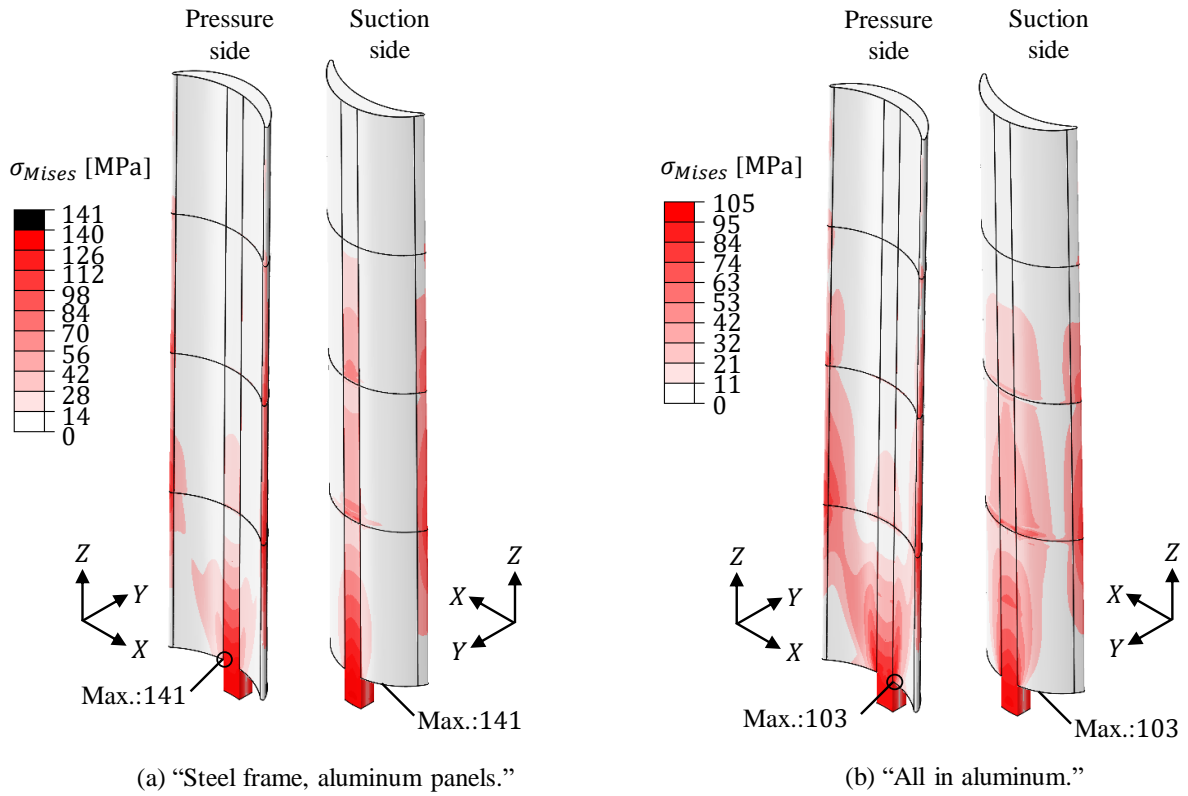
Figure 32. von Mises stress distribution for "concept 2." σ_{yield} is 279 MPa for steel and 210 MPa for aluminum. Safety factor is 2.0.
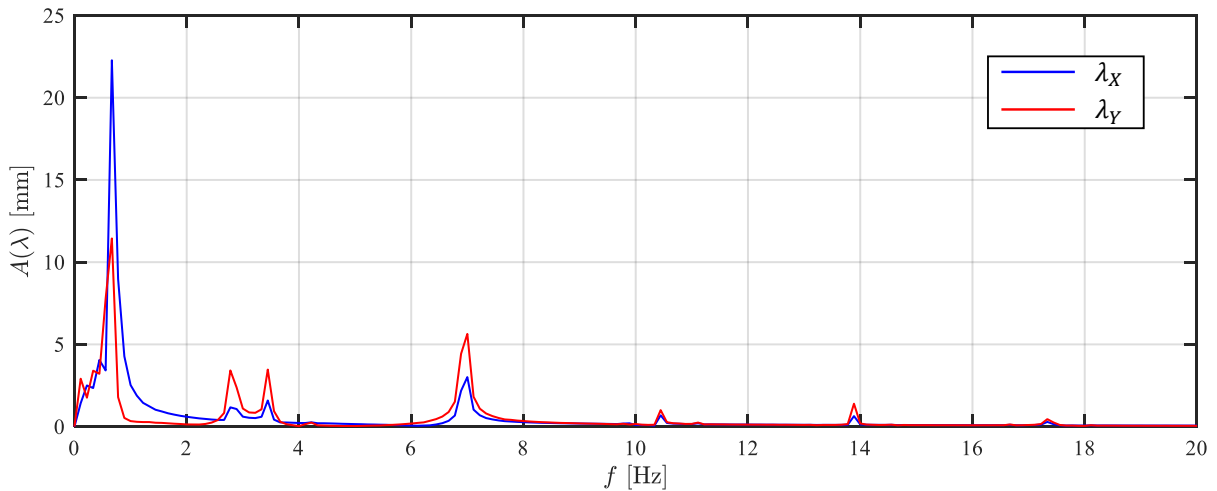
Figure 33. Frequency characteristics of the tip displacement based on FFT. Full-scale aeroelastic simulations at $\alpha = 20°$ and $V_{AW} = 8$ m/s ($Re = 7.1 \times 10^6$). λ_X is the tip displacement in the X direction, and λ_Y is the tip displacement in the Y direction.

4.6.2.2 Aeroelastic effects on propulsive performance

Figure 34 compares $\langle C_L \rangle$, $\langle C_D \rangle$, and $\langle C_M \rangle$ for deformable and rigid wingsails. The simulation results for the rigid body indicate that $\langle C_L \rangle$ is 2.135, whereas the aeroelastic simulation predicts a value that is approximately 3% lower. Comparing different sections of the deformable wingsail, "section 1" and "section 2" show lower $\langle C_L \rangle$ and higher $\langle C_D \rangle$ compared with "section 2" and "section 3" due to the tip vortices at the top and bottom ends.

44
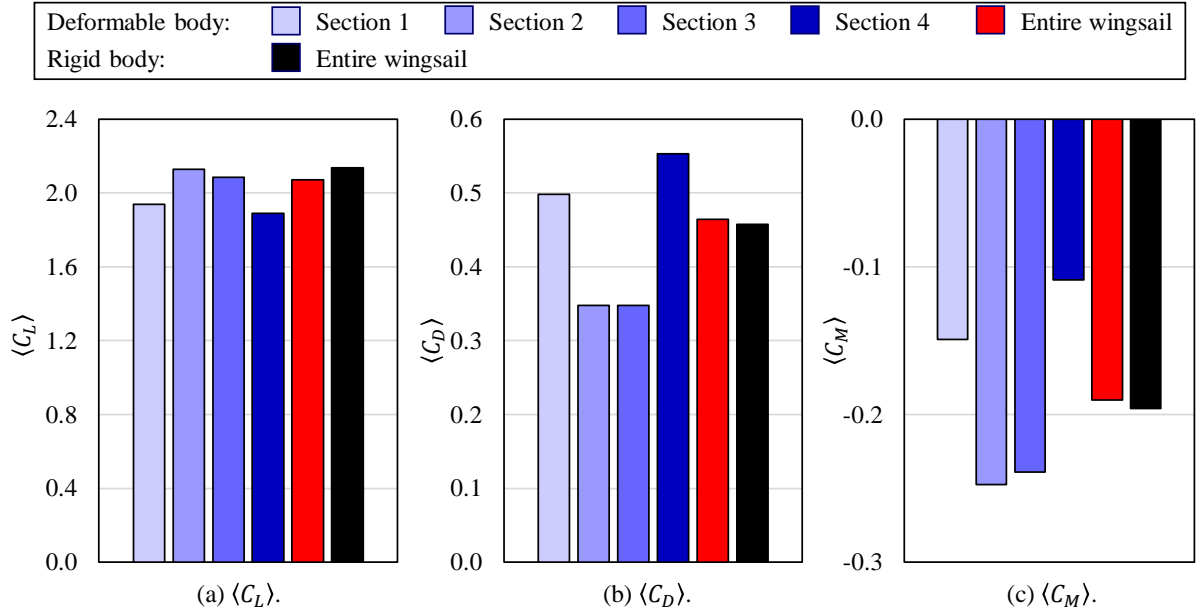
Figure 34. Comparison of $\langle C_L \rangle$, $\langle C_D \rangle$, and $\langle C_M \rangle$ between deformable and rigid wingsail. Full-scale aeroelastic simulations at $\alpha = 20°$ and $V_{AW} = 8$ m/s ($Re = 7.1 \times 10^6$).

Figure 35 shows the spectra of the force and moment coefficients. The main oscillation frequency of the force coefficients for the rigid-body wingsail, the is approximately 0.4 Hz with a relatively low amplitude. However, the high-frequency properties of the aerodynamic loads are much stronger when aeroelasticity is considered. A peak at 3.46 Hz is observed for all coefficients, while C_L shows an additional peak at 2.85 Hz. These two peaks in the frequency domain explain the oscillation of λ_Y in Figure 33. Additionally, the oscillation of the force and moment coefficients is much stronger for the deformable wingsail.
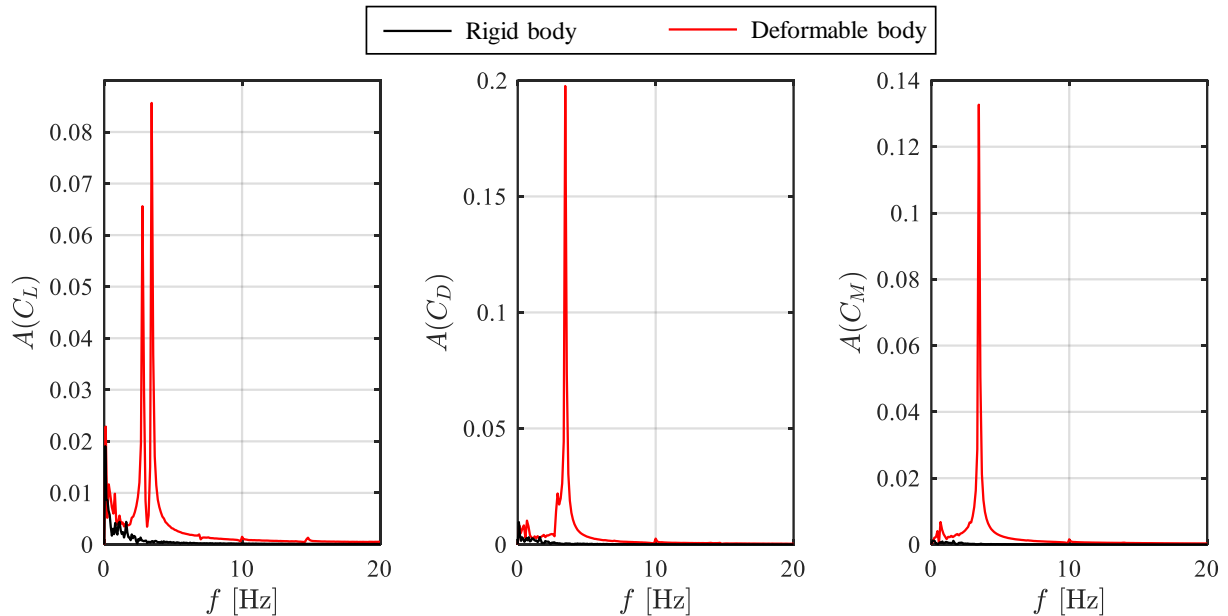
Figure 35. The spectra of C_L, C_D, and C_M based on FFT. Full-scale aeroelastic simulations at $\alpha = 20°$ and $V_{AW} = 8$ m/s ($Re = 7.1 \times 10^6$).

45

The observed aeroelastic effects are critical for understanding the wingsail structural response under operational loads, including fatigue, ultimate strength, and plastic deformation. The dynamic stresses induced by fluctuations in aerodynamic forces can significantly impact the material's fatigue life, potentially leading to premature failure if cyclic loads are not adequately accounted for. Additionally, peak aerodynamic loads may push sections of the wingsail, particularly near the tips, toward their yield strength, increasing the risk of plastic deformation.

5 Conclusions

Driven by the need to improve energy efficiency in maritime transport, the overall aim of this thesis, as formulated in Section 1.2, is to assess the aerodynamic and aeroelastic performance of crescent-shaped wingsails. The novelty of this work lies in the deep investigation of unsteady aerodynamic characteristics and the induced dynamic structural responses. This thesis concludes that due to strong unsteady characteristics of the flow field induced by the crescent-shaped wingsail, FSI is crucial for accurately predicting the propulsive performance and structural integrity of the wingsails. Furthermore, the methods used in this thesis can be extended to other sail types, such as two- and three-element wingsails, to evaluate their aerodynamic and structural performance under varying conditions.

Referring objectives listed in Section 1.2, detailed conclusions are presented below.

- **Aerodynamic characteristics**

In this thesis, the aerodynamic characteristics of the wingsails with crescent-shaped profiles are investigated using high-fidelity CFD simulations and validated with WT tests.

From the perspective of time-averaged aerodynamic characteristics, it is found that crescent-shaped wingsails have demonstrated the potential to generate appreciable lift across a range of wind conditions has been demonstrated. A high lift coefficient can be achieved over a wide range of α from 15° to 35°. Notably, a specific lift increase is observed after stall due to a high-velocity backflow near the suction side. The highest lift coefficient of 2.1 is obtained at an AOA of ~20°for a full-scale wingsail.

This study identifies certain challenges related to unsteady aerodynamic characteristics. It is concluded that strong flow separation intensifies flow unsteadiness, leading to increased fluctuating surface loads, which may compromise the strength and stability of the wingsail structure. The oscillation amplitude of the force coefficients can be ~10% of the time-averaged value.

In the triple-sail arrangement, notable interferences are observed between the wingsails. The largest propulsion is generated by the upstream (bow) wingsail, and the smallest propulsion by the downstream (stern) wingsail. However, the mean thrust generated by the three wingsails is close to that of an isolated single wingsail, so the arrangement does not affect the overall performance.

- **Model-scale effects**

Re values ranging from 1.8×10^5 (model-scale experiments) to 2.8×10^7 (full-scale applications) are studied.

It is found that C_L, C_D, and C_M are all sensitive to Re. Two force crises, where the force coefficients change dramatically with Re, are observed in the interval $Re \in [1.8 \times 10^5, 3.6 \times 10^6]$ (the first force crisis) and $Re \in [3.6 \times 10^5, 7.1 \times 10^6]$ (the second force crisis). As Re increases, C_L and C_D typically increase and decrease, respectively. Moreover, α_c is also sensitive to Re, as α_c decreases from approximately 30° to 15° in the first force crisis but increases to approximately 20° in the second force crisis. Due to the force crisis, the underestimation of C_L in model-scale tests can be up to ~30%. Therefore, given that most laboratory experiments are able to achieve moderate Re values up to 10^6, without careful

measures for proper tripping of the laminar-turbulent transition, their results are unlikely to be suitable for direct use in the assessment of real-world wingsail aerodynamics where the value of Re is on the order of 10^7.

As Re increases, the laminar-turbulent transition location in the boundary layer on the suction side of the wingsail migrates upstream. This shift in the transition position affects the location and nature of the resultant separation and reattachment patterns. The flow separation and reattachment dynamics contribute to the observed force crisis. At lower Re values (*e.g.*, 3.6×10^5), multiple separation points are observed at two different values of α: 15° and 20°. This effect leads to more complex unsteady characteristics. However, only one separation position is observed at the highest Re of 7.1×10^6 since the entire boundary layer on the suction side is turbulent.

- **Structural responses and aeroelasticity**

Quasi-static FEA is conducted for several structural design concepts of the crescent-shaped wingsail. Then, two-way coupled aeroelastic simulations are performed for a simplified solid model based on the selected structural design concept.

The structural analysis reveals that the wingsail concept featuring a strong frame with lightweight panels offers superior performance in terms of weight, strength, and rigidity. Of the assessment criteria considered, strength, specifically, von Mises yield and compressive normal stress, emerges as the most critical factor in evaluating wingsail structures.

It is concluded that the aeroelastic behavior of the wingsail is notably influenced by interactions between aerodynamic forces and structural deformation. Flutter at the fundamental eigenfrequency is a significant concern. Full-scale aeroelastic simulations demonstrate that aeroelasticity negatively impacts the aerodynamic performance of the wingsail. For instance, simulations show a reduction of ~3% in C_L when aeroelastic effects are considered. Small-scale vortex shedding on the suction side of the wingsail caused by flutter is identified as the mechanism of lift reduction.

- **Propulsive performance**

The propulsive performance of wingsails with crescent-shaped wingsails is calculated based on the principle of sailing. The long-term energy performance is then estimated by the in-house platform, ShipCLEAN.

This thesis demonstrates the significant potential of wingsails with crescent-shaped profiles in ship propulsion. The introduction of the novel crescent-shaped profile proves to be more effective in generating thrust force compared to the NACA 0015 profile, since it is evidenced that the potential thrust force coefficient is approximately 30% higher.

The implementation of crescent-shaped wingsails presents a promising avenue for enhancing the efficiency and sustainability of maritime transportation since the case study highlights the considerable fuel savings that can be achieved by installing a single crescent-shaped wingsail, with anticipated savings ranging from 9% for $V_{TW} = 10 \, \text{kn}$ to 25% for $V_{TW} = 20 \, \text{kn}$. Furthermore, the long-term fuel savings prediction indicates that the overall savings attributed to the crescent-shaped wingsail are 9.5%. One drawback of the new profile is the increased resistance experienced when sailing against the wind; however, such occurrences are infrequent.

6   Future perspectives

In this Chapter, key topics and areas for further investigation are highlighted. Their importance lies in their potential to enhance both the practical implementation and theoretical understanding of crescent-shaped wingsails and related technologies. By addressing these areas, future research can overcome current limitations, refine the methods employed in this thesis, and extend their applicability to a wider range of sail configurations and operational conditions. Each topic is aligned with the assumptions and constraints that framed the scope of this work, ensuring a clear continuity between the findings presented and the recommended future directions.

- **Wingsail aerodynamics optimization**

This thesis includes a preliminary parametric sensitivity study regarding the crescent-shaped profile. Future work on wingsail profile optimization can focus on further refining the crescent-shaped profile to enhance aerodynamic performance (Guzelbulut *et al.*, 2024; Zhang *et al.*, 2023). Advanced optimization algorithms, such as the non-dominated sorting genetic algorithm (NSGA-II) and PSO, can be employed to explore the design space. Recently, machine learning-based methods, such as physics-informed neural networks (PINN), have become increasingly popular, which can also be considered for establishing the optimization platform.

In addition, since strong interactions among multiple wingsails have been indicated, the arrangement of wingsails on the deck can also be an aspect of optimization.

- **Wingsail-hull interaction**

As mentioned in Section 1.3, though the interaction among wingsails, ship hull, and superstructures are basically not considered in this thesis. However, these interactions are critical for evaluating the overall propulsion system (Zeng *et al.*, 2024b; Zhang *et al.*, 2024). Aerodynamic and hydrodynamic interactions affect lift, drag, and vessel resistance. These interactions can also influence vessel stability and maneuverability. Future studies can explore the effects of different wingsail placements and orientations relative to the hull, with a focus on optimizing the balance between aerodynamic efficiency and vessel performance.

Coupling aerodynamic, hydrodynamic, and rigid body dynamics (RBD) simulations will be essential to accurately capture these interactions. Techniques such as two-phase flow simulations, which model the interaction between the wingsails and the surrounding water, can be employed.

- **Further structural analysis**

This thesis studies the aeroelasticity of the crescent-shaped based on a simplified solid model. The two-way coupled aeroelastic simulations reveal the structural responses due to global bending. However, the dynamic structural responses regarding ultimate stress, potential plastic deformation, buckling, and fatigue are not deeply addressed. Therefore, the structural integrity of wingsails remains a key area for further investigation. Future research can focus on developing more advanced structural analysis techniques that account for complex loading scenarios, including fluctuating wind forces and wave-induced motions.

Beyond the linear elastic structural response, fatigue analysis can be a primary focus in future research, given that wingsails are subjected to constantly fluctuating wind loads, which can lead to material fatigue over time. Moreover, buckling is another critical consideration, especially

given the thin-walled nature of wingsails and the high aspect ratios involved. There is a significant risk of both local and global buckling, particularly in the telescopic sections where structural strength is reduced.

References

Ageze, M. B., Hu, Y., & Wu, H. (2017). Comparative study on uni-and bi-directional fluid structure coupling of wind turbine blades. *Energies*, *10*(10), 1499.

Ajaj, R. M., Parancheerivilakkathil, M. S., Amoozgar, M., Friswell, M. I., & Cantwell, W. J. (2021). Recent developments in the aeroelasticity of morphing aircraft. *Progress in Aerospace Sciences*, *120*, 100682.

ASTM. (2004). Standards specification for aluminum and aluminum-alloy sheet and plate. In: American Society for Testing and Materials.

Atkins, D. W. (1996). *The CFD assisted design and experimental testing of a wing-sail with high lift devices*. University of Salford (United Kingdom).

Atkinson, G., Nguyen, H., & Binns, J. (2018). Considerations regarding the use of rigid sails on modern powered ships. *Cogent Engineering*, *5*(1), 1-20. https://doi.org/10.1080/23311916.2018.1543564

Atkinson, G. M. (2019). Analysis of lift, drag and CX polar graph for a 3D segment rigid sail using CFD analysis. *Journal of Marine Engineering and Technology*, *18*(1), 36-45. https://doi.org/10.1080/20464177.2018.1494953

Atkinson, G. M., & Binns, J. (2018). Power profile for segment rigid sail. *Journal of Marine Engineering and Technology*, *17*(2), 99-105. https://doi.org/10.1080/20464177.2017.1319997

Aubin, N., Augier, B., Deparday, J., Sacher, M., & Bot, P. (2018). Performance enhancement of downwind sails due to leading edge flapping: A wind tunnel investigation. *Ocean Engineering*, *169*, 370-378.

Bak, S., Yoo, J., & Song, C. Y. (2013). Fluid-structure interaction analysis of deformation of sail of 30-foot yacht. *International Journal of Naval Architecture and Ocean Engineering*, *5*(2), 263-276.

Barlow, J. B., Rae, W. H., & Pope, A. (1999). *Low-speed wind tunnel testing*. John wiley & sons.

Basting, S., Quaini, A., Čanić, S., & Glowinski, R. (2017). Extended ALE method for fluid–structure interaction problems with large structural displacements. *Journal of Computational Physics*, *331*, 312-336.

Bazilevs, Y., Takizawa, K., & Tezduyar, T. E. X. (2013). *Computational fluid-structure interaction: methods and applications*. John Wiley & Sons.

Benra, F.-K., Dohmen, H. J., Pei, J., Schuster, S., & Wan, B. (2011). A comparison of one-way and two-way coupling methods for numerical analysis of fluid-structure interactions. *Journal of applied mathematics*, *2011*(1), 853560.

Betz, A. (1925). *A method for the direct determination of wing-section drag*.

Bialystocki, N., & Konovessis, D. (2016). On the estimation of ship's fuel consumption and speed curve: A statistical approach. *Journal of Ocean Engineering and Science*, *1*(2), 157-166. https://doi.org/10.1016/j.joes.2016.02.001

Billah, K. Y., & Scanlan, R. H. (1991). Resonance, Tacoma Narrows bridge failure, and undergraduate physics textbooks. *American Journal of Physics*, *59*(2), 118-124.

Bisplinghoff, R. L., Ashley, H., & Halfman, R. L. (2013). *Aeroelasticity*. Courier Corporation.

Blakeley, A., Flay, R., & Richards, P. (2012). Design and optimisation of multi-element wing sails for multihull yachts. 18th Australasian Fluid Mechanics Conference, Launcestion, Australia,

Blount, H., & Portell, J. M. (2021). *CFD investigation of wind powered ships under extreme conditions* Gothenburg, Sweden. https://odr.chalmers.se/handle/20.500.12380/304254

Bordogna, G., Keuning, J. A., Huijsmans, R. H. M., & Belloli, M. (2018). Wind-tunnel experiments on the aerodynamic interaction between two rigid sails used for wind-assisted propulsion. *International Shipbuilding Progress*, *65*(1), 93-125.

Borgoltz, A., Intaratep, N., & Devenport, W. J. (2019). Aerodynamic Effects of Boundary Layer Trip Strips on the Flow over a NACA63018 Airfoil. *Virginia Polytechnic Inst. and State Univ., Blacksburg, VA*.

Bot, P., Rabaud, M., Thomas, G., Lombardi, A., & Lebret, C. (2016). Sharp transition in the lift force of a fluid flowing past nonsymmetrical obstacles: evidence for a lift crisis in the drag crisis regime. *Physical review letters*, *117*(23), 234501.

BS EN. (2004). 10025-2: 2004: Hot rolled products of structural steels. Part 2-Technical delivery conditions for non-alloy structural steels. In *British Standards Institution, London*.

Burden, A., Lloyd, T., Mockler, S., Mortola, L., Shin, I. B., & Smith, B. (2010). Concept design of a fast sail assisted feeder container ship.

Chen, J., Wang, Q., Shen, W. Z., Pang, X., Li, S., & Guo, X. (2013). Structural optimization study of composite wind turbine blade. *Materials & Design (1980-2015)*, *46*, 247-255.

Chen, Z., Cai, W., & Zeng, Q. (2022). A numerical study on the thrust and interaction of a three-sail wind-assisted propulsion system. Proceedings of the ASME 2022, 41st International Conference on Ocean, Offshore and Arctic,

Dassault Systemes. (2020). Abaqus 2020. In *Abaqus Analysis User's Guide*.

Davidson, L. (2019). *Fluid mechanics, turbulent flow and turbulence modeling*. Division of Fluid Dynamics, Department of Mechanics and Maritime Sciences, Chalmers University of Technology.

Della Posta, G., Ciri, U., Leonardi, S., & Bernardini, M. (2021). A novel two-way coupling method for the study of the aeroelasticity of wind turbines in a large eddy simulation framework. 14 th European Conference on Turbomachinery Fluid dynamics & Thermodynamics,

Della Posta, G., Leonardi, S., & Bernardini, M. (2022). A two-way coupling method for the study of aeroelastic effects in large wind turbines. *Renewable Energy*, *190*, 971-992.

DNV. (2022). *[DNV-ST-0511] Wind assisted propulsion systems - edition Oct, 2022*. https://standards.dnv.com/explorer/document/C0E1D699CA1748C585C31004BC1B1C85/5?_ga=2.144478 517.1272353220.1681210027-409665076.1638902377

Drela, M. (1989). XFOIL: An analysis and design system for low Reynolds number airfoils. Low Reynolds Number Aerodynamics: Proceedings of the Conference Notre Dame, Indiana, USA, 5–7 June 1989,

Ezkurra, M., Esnaola, J. A., Martinez Agirre, M., Lertxundi, U., & Etxeberria, U. (2018). Analysis of one-way and two-way FSI approaches to characterise the flow regime and the mechanical behaviour during closing manoeuvring operation of a butterfly valve.

Faber, J., Hanayama, S., Zhang, S., Pereda, P., Comer, B., Hauerhof, E., van der Loeff, W. S., Smith, T., Zhang, Y., & Kosaka, H. (2020). Reduction of GHG emissions from ships—Fourth IMO GHG study 2020—Final report. *IMO MEPC*, *75*(7), 15.

Forouzi Feshalami, B., He, S., Scarano, F., Gan, L., & Morton, C. (2022). A review of experiments on stationary bluff body wakes. *Physics of Fluids*, *34*(1).

Fröhlich, J., & Von Terzi, D. (2008). Hybrid LES/RANS methods for the simulation of turbulent flows. *Progress in Aerospace Sciences*, *44*(5), 349-377.

Furukawa, H., Blakeley, A. W., Flay, R. G. J., & Richards, P. J. (2015). Performance of wing sail with multi element by two-dimensional wind tunnel investigations. *Journal of Fluid Science and Technology*, *10*(2), JFST0019-JFST0019.

Giovannetti, L. M., Dhome, U., Malmek, K., Persson, A., & Wielgosz, C. (2022). Multi-wing sails interaction effects. SNAME Chesapeake Sailing Yacht Symposium,

Guzelbulut, C., Badalotti, T., & Suzuki, K. (2024). Optimization techniques for the design of crescent-shaped hard sails for wind-assisted ship propulsion. *Ocean Engineering*, *312*, 119142. https://doi.org/https://doi.org/10.1016/j.oceaneng.2024.119142

Hoang, N. T., & Bui, B. V. (2019). Investigation of wind tunnel wall effect and wing-fuselage interference regarding the prediction of wing aerodynamics and its influence on the horizontal tail. *Journal of Mechanical Science and Technology*, *33*, 2737-2746.

Hu, Y., He, J., Tang, J., Xue, S., Liu, S., & Wu, Y. (2015). Sail Structure Design and Stability Calculation for Sail-assisted Ships. Marine Engineering Frontiers,

Hu, Y. H., Zeng, X. M., & Li, S. Y. (2012). Research on the aerodynamic characteristics of ellipse wing sail. *Advanced materials research*, *347*, 2249-2254.

Hussain, M. D., & Amin, O. M. (2021). A comprehensive analysis of the stability and powering performances of a hard sail–assisted bulk carrier. *Journal of Marine Science and Application*, *20*(3), 426-445.

IMO. (2018). Interpretation of Initial IMO Strategy on Reduction of GHG Emissions from Ships. In (Vol. 60, pp. 195-201).

IMO. (2020). *Report of fuel oil consumption data submitted to the IMO Ship Fuel Oil Consumption Database in GISIS* (Energy efficiency of ships, Issue.

Kass, M. D., Abdullah, Z., Biddy, M. J., Drennan, C., Haq, Z., Hawkins, T., Jones, S., Holliday, J., Longman, D. E., & Menter, S. (2018). *Understanding the opportunities of biofuels for marine shipping*.

Khan, L., Macklin, J., Peck, B., Morton, O., & Souppez, J.-B. R. G. (2021, 2021/9//). A review of wind-assisted ship propulsion for sustainable commercial shipping: Latest developments and future stakes. Proceedings of the Wind Propulsion Conference 2021, London, UK.

Kijima, K., Katsuno, T., Nakiri, Y., & Furukawa, Y. (1990). On the manoeuvring performance of a ship with theparameter of loading condition. *Journal of the society of naval architects of Japan*, *1990*(168), 141-148.

Kimball, J. (2009). *Physics of Sailing*. CRC Press. https://doi.org/10.1201/9781420073775

Laboratory, C. U. A. (1936). *Measurement of profile drag by the pitot-traverse method*. HM Stationery Office.

Larsson, L. (1990). Scientific methods in yacht design. *Annual Review of Fluid Mechanics*, *22*(1), 349-385.

Lee, H., Jo, Y., Lee, D. J., & Choi, S. (2016). Surrogate model based design optimization of multiple wing sails considering flow interaction effect. *Ocean Engineering*, *121*, 422-436. https://doi.org/10.1016/j.oceaneng.2016.05.051

Li, D., Li, G., Dai, J., & Li, P. (2017). A new type of collapsible wing sail and its aerodynamic performance. International Conference on Offshore Mechanics and Arctic Engineering,

Li, D., Zhang, Y., Li, P., Dai, J., & Li, G. (2019). Aerodynamic performance of a new double-flap wing sail. *Polish Maritime Research*, *26*(4), 61-68.

Ljungberg, E. (2023). Evaluation of Novel Wingsail Concepts in Terms of Aerodynamic Efficiency.

Lu, R., & Ringsberg, J. W. (2020). Ship energy performance study of three wind-assisted ship propulsion technologies including a parametric study of the Flettner rotor technology. *Ships and Offshore Structures*, *15*(3), 249-258. https://doi.org/10.1080/17445302.2019.1612544

Ma, R., Zhao, H., Wang, K., Zhang, R., Hua, Y., Jiang, B., Tian, F., Ruan, Z., Wang, H., & Huang, L. (2022). Leakage fault diagnosis of lifting and lowering hydraulic system of wing-assisted ships based on WPT-SVM. *Journal of marine science and engineering*, *11*(1), 27.

Ma, Y., Bi, H., Gan, R., Li, X., & Yan, X. (2018). New insights into airfoil sail selection for sail-assisted vessel with computational fluid dynamics simulation. *Advances in Mechanical Engineering*, *10*(4), 1-12. https://doi.org/10.1177/1687814018771254

Madhavan, S., Al-Jahmany, Y. Y., Minev, P. D., & Nandakumar, K. (2014). On the transition to 3D modes for channel flow past a square cylinder. *The Canadian Journal of Chemical Engineering*, *92*(12), 2122-2137.

Malmek, K., Dhomé, U., Larsson, L., Werner, S., Ringsberg, J. W., & Finnsgård, C. (2020). Comparison of two rapid numerical methods for predicting the performance of multiple rigid wing-sails. The 5th International Conference on Innovation in High Performance Sailing Yachts and Sail-Assisted Ship Propulsion (INNOV'SAIL 2020), Gothenburg, Sweden.

Malmek, K., Larsson, L., Werner, S., Ringsberg, J. W., Bensow, R., & Finnsgård, C. (2024). Rapid aerodynamic method for predicting the performance of interacting wing sails. *Ocean Engineering*, *293*, 116596. https://doi.org/https://doi.org/10.1016/j.oceaneng.2023.116596

Matsumoto, M., Shirato, H., Yagi, T., Shijo, R., Eguchi, A., & Tamaki, H. (2003). Effects of aerodynamic interferences between heaving and torsional vibration of bridge decks: the case of Tacoma Narrows Bridge. *Journal of Wind Engineering and Industrial Aerodynamics*, *91*(12-15), 1547-1557.

Menter, F. R., Smirnov, P. E., Liu, T., & Avancha, R. (2015). A One-Equation Local Correlation-Based Transition Model. *Flow, Turbulence and Combustion 2015 95:4*, *95*(4), 583-619. https://doi.org/10.1007/S10494-015-9622-4

Mian, H. H., Wang, G., & Ye, Z.-Y. (2014). Numerical investigation of structural geometric nonlinearity effect in high-aspect-ratio wing using CFD/CSD coupled approach. *Journal of Fluids and Structures*, *49*, 186-201 %@ 0889-9746.

Nava, S., Bot, P., Cater, J., & Norris, S. (2016). Modelling the lift crisis of a cambered plate at 0 angle of attack. Proc. Of the 20th Australasian Fluid Mechanics Conference, Perth, Australia,

Nikmanesh, M. (2021). *Sailing performance analysis using CFD simulations: A study on crescent shaped wing profiles* Chalmers University of Technology]. Gothenburg, Sweden. https://odr.chalmers.se/handle/20.500.12380/304303

Nykvist, B., & Whitmarsh, L. (2008). A multi-level analysis of sustainable mobility transitions: Niche development in the UK and Sweden. *Technological forecasting and social change*, *75*(9), 1373-1387 %@ 0040-1625.

Ouchi, K., Shima, K., & Kimura, K. (2023). 2023A-OS6-3 "WIND HUNTER "-the Zero Emission Ship Powered by Wind and Hydrogen Energy. Conference Proceedings The Japan Society of Naval Architects and Ocean Engineers 37,

Ouchi, K., Uzawa, K., & Kanai, A. (2011). Huge Hard Wing Sails for the Propulsor of Next Generation Sailing Vessel. Second International Symposium on Marine Propulsors, Hamburg, Germany.

Ouchi, K., Uzawa, K., Kanai, A., & Katori, M. (2013). Wind challenger" the next generation hybrid sailing vessel. The Third International Symposium on Marine Propulsors, Launceston, Tasmania, Australia, Launceston, Tasmania, Australia.

Patankar, S. V. (1980). *Numerical heat transfer and fluid flow*. CRC Press. https://doi.org/10.13182/nse81-a20112

Persson, A., Li, D. Q., Olsson, F., Werner, S., & Dhomé, U. (2019). Performance prediction of wind propulsion systems using 3D CFD and route simulation. RINA, Royal Institution of Naval Architects-International Conference on Wind Propulsion, WP 2019, 15-16 October 2019, London, United Kingdom,

Rao, S. S., & Yap, F. F. (1995). *Mechanical vibrations* (Vol. 4). Addison-Wesley New York.

Register, L. s. (2024). *ENERGY EFFICIENCY RETROFIT REPORT 2024: Applying Wind-Assisted Propulsion to ships*.

Rehimi, F., Aloui, F., Nasrallah, S. B., Doubliez, L., & Legrand, J. (2008). Experimental investigation of a confined flow downstream of a circular cylinder centred between two parallel walls. *Journal of Fluids and Structures*, *24*(6), 855-882.

Reichardt, H. (1951). Vollständige Darstellung der turbulenten Geschwindigkeitsverteilung in glatten Leitungen. *ZAMM - Journal of Applied Mathematics and Mechanics / Zeitschrift für Angewandte Mathematik und Mechanik*, *31*(7), 208-219. https://doi.org/10.1002/ZAMM.19510310704

Richter, T. (2010). Numerical methods for fluid-structure interaction problems. *Institute for Applied Mathematics, University of Heidelberg, Germany*.

Ritchie, H., Roser, M., & Rosado, P. (2020). CO2 and Greenhouse Gas Emissions. *Our World in Data*.

Rockwood, M. P., & Green, M. A. (2019). Real-time identification of vortex shedding in the wake of a circular cylinder. *AIAA Journal*, *57*(1), 223-238.

Salim, S. M. (2011). *Computational study of wind flow and pollutant dispersion near tree canopies* University of Nottingham].

Schlichting, H., & Gersten, K. (2016). *Boundary-layer theory*. springer.

Sheldahl, R. E., & Klimas, P. C. (1981). *Aerodynamic characteristics of seven symmetrical airfoil sections through 180-degree angle of attack for use in aerodynamic analysis of vertical axis wind turbines*. http://www.osti.gov/servlets/purl/6548367/

Shur, M. L., Spalart, P. R., Strelets, M. K., & Travin, A. K. (2008). A hybrid RANS-LES approach with delayed-DES and wall-modelled LES capabilities. *International Journal of Heat and Fluid Flow*, *29*(6), 1638-1649. https://doi.org/10.1016/j.ijheatfluidflow.2008.07.001

Siemens PLM Software. (2021). STAR-CCM+ user guide (version 16.02). In: Siemens PLM Software Inc: Munich, Germany.

Smith, A. M. O. (1975). High-lift aerodynamics. *Journal of Aircraft*, *12*(6), 501-530.

Sofla, A., Meguid, S., Tan, K., & Yeo, W. (2010). Shape morphing of aircraft wing: Status and challenges. *Materials & Design*, *31*(3), 1284-1292.

Souppez, J.-B. (2023). Structural Challenges of Low-Emission Vessels: A Review. *International Journal of Maritime Engineering*, *165*(A2), 165-178 %@ 1479-8751.

Souppez, J.-B. R., Bot, P., & Viola, I. M. (2022). Turbulent flow around circular arcs. *Physics of Fluids*, *34*(1).

Souppez, J.-B. R., & Viola, I. M. (2024). Water tunnel testing of downwind yacht sails. *Experiments in Fluids*, *65*(2), 1-19.

Spalart, P. R. (1997). Comments on the Feasibility of LES for Wings and on the Hybrid RANS/LES Approach. Proceedings of the First AFOSR International Conference on DNS/LES, 1997,

Spalart, P. R., Deck, S., Shur, M. L., Squires, K. D., Strelets, M. K., & Travin, A. (2006). A new version of detached-eddy simulation, resistant to ambiguous grid densities. *Theoretical and computational fluid dynamics*, *20*, 181-195.

Storhaug, G., Borzacchiello, G. R., & Hoffmeister, H. (2022). Fatigue assessment of wind assisted propulsion systems. Proceedings of the ASME 2022 41st Internal Conference on Ocean, Offshore and Arctic Engineering,

Tank, J., Klose, B., Jacobs, G., & Spedding, G. (2021). Flow transitions on a cambered airfoil at moderate Reynolds number. *Physics of Fluids*, *33*(9).

Thies, F., & Fakiolas, K. (2022). Wind propulsion. In *Sustainable Energy Systems on Ships* (pp. 353-402). Elsevier.

Tillig, F., Ringsberg, J. W., Mao, W., & Ramne, B. (2017). A generic energy systems model for efficient ship design and operation. *Proceedings of the Institution of Mechanical Engineers, Part M: Journal of Engineering for the Maritime Environment*, *231*(2), 649-666. https://doi.org/10.1177/1475090216680672

Tillig, F., Ringsberg, J. W., Psaraftis, H. N., & Zis, T. (2019). ShipCLEAN–an integrated model for transport efficiency, economics and CO2 emissions in shipping. Proceedings of the 2nd International Conference on Modelling and Optimization of Ship Energy Systems (MOSES 2019),

UNCTAD. (2024). *Review of Maritime Transport 2024*. United Nations.

Viola, I. M. (2013). Recent advances in sailing yacht aerodynamics. *Applied Mechanics Reviews*, *65*(4), 040801.

Viola, I. M., Bartesaghi, S., Van-Renterghem, T., & Ponzini, R. (2014). Detached Eddy Simulation of a sailing yacht. *Ocean Engineering*, *90*, 93-103.

Viola, I. M., Biancolini, M. E., Sacher, M., & Cella, U. (2015). A CFD-based wing sail optimisation method coupled to a vpp. 5th High Performance Yacht Design Conference, HPYD 2015,

Viola, I. M., & Flay, R. G. (2012). Sail aerodynamics: on-water pressure measurements on a downwind sail. *Journal of ship research*, *56*(04), 197-206.

von Klemperer, C. J., Horwitz, R. A., & Malan, A. G. (2023). An articulating wingsail design for Wind Assisted Ship Propulsion (WASP) applications. *Scientific African*, *20*, e01699.

Wang, K., Xue, Y., Xu, H., Huang, L., Ma, R., Zhang, P., Jiang, X., Yuan, Y., Negenborn, R. R., & Sun, P. (2022). Joint energy consumption optimization method for wing-diesel engine-powered hybrid ships towards a more energy-efficient shipping. *Energy*, *245*, 123155.

Williamson, C. H. (1996). Vortex dynamics in the cylinder wake. *Annual Review of Fluid Mechanics*, *28*(1), 477-539.

Workinn, D. (2021). *A high-level interface for a sailing vessel* http://urn.kb.se/resolve?urn=urn:nbn:se:kth:diva-299430

Yao, H.-D., He, G.-W., Wang, M., & Zhang, X. (2008). Time correlations of pressure in isotropic turbulence. *Physics of Fluids*, *20*(2), 025105-025105. https://doi.org/https://doi.org/10.1063/1.2870111

Yin, S., Yang, Y., Liu, B., & Meng, X. (2023). Experimental study on propulsion performance of unmanned sailboat with arc sail. *Ocean Engineering*, *282*, 115029.

Zeng, Q., Cai, W., & Xu, J. (2024a). Large-Eddy Simulation of Low-Frequency Flow Oscillations for NACA0012 and Dynarig Sail at Large Attack Angles. *Journal of marine science and engineering*, *12*(5), 835.

Zeng, Q., Lyu, X., Cai, W., Zhang, L., & Xu, J. (2024b). Influence of wind gradient and ground effect on the aerodynamic forces of a Dynarig sail at large heeling angles. *Ocean Engineering*, *312*, 119069.

Zeng, Q., Zhang, X., Cai, W., & Zhou, Y. (2023). Wake distortion analysis of a Dynarig and its application in a sail array design. *Ocean Engineering*, *278*, 114341. https://doi.org/10.1016/j.oceaneng.2023.114341

Zhang, H., Hu, Y., & He, J. (2022). Wind tunnel experiment of multi-mode arc sail device. *Polish Maritime Research*, *28*(4), 20-29.

Zhang, R., Huang, L., Ma, R., Peng, G., Ruan, Z., Wang, C., Zhao, H., Li, B., & Wang, K. (2024). Numerical investigation on the effects of heel on the aerodynamic performance of wing sails. *Ocean Engineering*, *305*, 117897.

Zhang, R., Huang, L., Peng, G., Ma, R., Wang, K., Tian, F., & Song, Q. (2023). A novel method of desynchronized operation of sails for ship wind-assisted propulsion system. *Ocean Engineering*, *288*, 115964.

Zhu, H. (2020). *CFD investigation of wind-powered ships under extreme condition: Simulations on the naca-0015 foil under deep stall condition* Chalmers University of Technology]. Gothenburg, Sweden. https://odr.chalmers.se/handle/20.500.12380/301919

Zhu, H. (2023). *Methods for the Evaluation of Wingsails with a Crescent-shaped Profile* Chalmers University of Technology]. Gothenburg, Sweden.

Zhu, H., Bikkireddy, S., Ringsberg, J. W., & Yao, H.-D. (2023). Structure analysis of lightweight sail structures for wind-assisted ship propulsion. 9th International Conference on Marine Structures , MarStruct, Gothenburg, Sweden.

Zhu, H., Nikmanesh, M. B., Yao, H. D., Ramne, B., & Ringsberg, J. W. (2022a). Propulsive Performance of a Novel Crescent-Shaped Wind Sail Analyzed With Unsteady Rans. Proceedings of the International Conference on Offshore Mechanics and Arctic Engineering - OMAE, Hamburg, German.

Zhu, H., Yao, H.-D., & Ringsberg, J. W. (2022b). Unsteady RANS and IDDES study on a telescopic crescent-shaped windsail. International Conference on Ships and Offshore Structures, ICSOS 2022, Ålesund, Norway.